Detection and control of calcium carbonate formation and phase conversion: laboratory and field work

by

©Boyang Gao

A thesis submitted to the School of Graduate Studies in partial fulfillment of the requirements for the degree of

Ph.D.

Department of Chemistry

Memorial University of Newfoundland & Labrador

December 2022

St. John's Newfoundland & Labrador

Abstract

This thesis work relates to calcium carbonate ($CaCO_3$) polymorphism, focusing on crystallization and dissolution in non-equilibrium situations, to show why understanding $CaCO_3$ chemistry can help control the reactivity of both laboratory-synthesized and naturally occurring carbonate minerals.

My laboratory work focused on how two $CaCO_3$ polymorphs, calcite and aragonite, dissolve and recrystallize in aqueous solution. The experimental results show that aragonite dissolves (and recrystallizes as calcite) faster when there is more calcite present with it. To understand the chemistry behind this observation, the solubility constant and recrystallization rates of each polymorph need to be considered. These results show why putting these two polymorphs together in water causes a non-equilibrium situation that cannot be well-described by their solubility constants alone. In addition, the dissolution-recrystallization behavior of mixed powder is tremendously retarded by the addition of a small amount of polyphosphate in the suspension. Based on bulk and surface characterization data (Infrared Spectroscopy and Solid-state Nuclear Magnetic Resonance), the phosphate species is incorporated only near the $CaCO_3$ particle surface without forming any separate phosphate-rich phase as a protecting shell. These data show that such dispersed surface-embedded phosphate entities stabilize solids against recrystallization in an aqueous environment. Moreover, polyphosphate treatment can also slightly improve the thermal stability of

aragonite in terms of phase conversion.

The thesis work also applies similar carbonate chemistry knowledge to characterization method development for field research. Carbonate mineral deposits are a surface manifestation of serpentinization, a water-rock reaction that provides energy and carbon sources that could support microbial life on serpentine-rich areas of Earth, or even on other planets like Mars. Infrared spectra from this study identify calcite and aragonite phases from ground-truthed samples. Based on literature from both laboratory- and field-based studies, the presence of aragonite could be due to high pH water and magnesium ions produced by serpentinization. Similar literature shows that calcite could be formed directly or caused by phase conversion of aragonite over time. However, the period required for the phase transformation is unknown. The thesis work describes how knowledge of carbonate polymorph control in a laboratory setting can help us begin to understand what geochemical factors may be necessary for phase selection during the serpentinization process.

Acknowledgements

I would like to thank my supervisor Dr. Kristin M. Poduska for her expert advice and constantly encourage during my Ph.D. period. I would also like to thank Dr. Asher Schmidt and Dr. Shifi Kababya for their boundless help on solid-state nuclear magnetic resonance analysis and their research collaboration. I also want to thank Dr. Penny L. Morrill for her tremendous leadership in the fieldwork.

I want to thank my colleagues and friends for supporting me academically and in life. I would also love to express my appreciation to my parents and wife, who have given me great moral support. Without your patience and encouragement, I couldn't make such impressive achievements in my Ph.D. studies.

This project would have been impossible without the financial support from Canadian Space Agency and my supervisor's NSERC grants. Moreover, I especially want to thank the Chemistry Department at Memorial University for providing excellent resources to support my research.

Table of Contents

List of Tables

List of Figures

List of Abbreviations

ACC	Amorphous calcium carboante
ACP	Amorphous calcium phosphate
ATR	Attenuated total reflectance
AWNS	Aragonite under water treatment (unstirred)
AWS	Aragonite under water treatment (stirred)
BMD	Blow Me Down massif
CP	Cross polarization
CSE	Chemical shift echo
DA	Disordered aragonite
DC	Disordered calcite
DCP	Dibasic calcium phosphate
DCPD	Dicalcium phosphate dihydrate
DE	Direct excitation
DSC	Differential scanning calorimetry
EDX	Energy dispersive X-ray
FIR	Far infrared
FTIR	Fourier-transform infrared spectroscopy

HAp	Hydroxypatite
ICP-OES	Inductively coupled plasma-optical emission spectroscopy
IR	Infrared
MIR	Mid-infrared
NIR	Near-infrared
pi	Orthophosphate
NMR	Nuclear magnetic resonance
REDOR	Rotational-echo, double-resonance
SEM	Scanning electron microscopy
SHMP	Sodium hexametaphosphate
ssNMR	Solid-state nuclear magnetic resonance
SWIR	Short wave-infrared
TGA	Thermogravimetric analysis
WHC	Winter House Brook canyon
XRD	X-ray diffraction

Chapter 1

Introduction

1.1 Research inspiration

Calcium carbonate ($CaCO_3$) is a prominent carbonate mineral in nature, with three common polymorphic forms: calcite, aragonite and vaterite [2]. They have the same chemical formula ($CaCO_3$), but the arrangement of Ca^{2+} and CO_3^{2-} ions differs, resulting in different crystal structures. The study of $CaCO_3$, especially its dissolution and crystallization in solution, is in the global spotlight for two main reasons.

First, the dissolution and crystallization of $CaCO_3$ are ubiquitous, especially in nature. For example, hitherto unprecedented amounts of anthropogenic CO_2 dissolve in the oceans, leading to ocean acidification [3]. As a result, the carbonate biominerals in the sea are forced to dissolve to neutralize the ocean pH, jeopardizing biominerals. Therefore, many efforts have been made to solve this problem, such as removing released CO_2 through the mineral carbonation [4], or enhancing ocean alkalinity through dissolved alkaline minerals in seawater [5].

Second, for industrial and medical applications, $CaCO_3$ can be treated as an additive (filler) in other materials, such as cement [6], printing paper [7], plastic [8, 9], to

change the physical or chemical properties. Also, due to the high compatibility and non-toxicity, $CaCO_3$ is regarded as a biomaterial for medical applications [10, 11]. All the above applications are related to the dissolution and crystallization of $CaCO_3$. The formation of $CaCO_3$ filler particles involves the process of $CaCO_3$ crystallization. Using $CaCO_3$ as a drug carrier relies on dissolution of $CaCO_3$ in tumors, since the solubility of $CaCO_3$ is pH-sensitive, which may help accelerate or delay the release of drug based on the local pH of the tumors [11].

The study of the interaction between phosphate and $CaCO_3$ originates from the discovery of phosphorus in naturally occurring $CaCO_3$ biominerals, such as coral skeletons or sea urchin spines [12, 13]. Laboratory studies demonstrate that phosphate plays a vital role in $CaCO_3$ phase selection and crystal size control [14,15]. The applications of the interaction between $CaCO_3$ solids and phosphate have received wide attention as drug carriers [16, 17], phosphorus recycling from industrial wastewater [18], chemical modifiers of $CaCO_3$ filler [19, 20], and to control flocculation and scaling [21]. In biomaterial formation, orthophosphates such as phosphate buffers are often used to trigger secondary phases [22]. In contrast, for scaling and flocculation control applications, including zetasizer sample preparations, it is polyphosphates (such as sodium hexametaphosphate (SHMP)) that are widely used, precisely because they do not tend to trigger detectable secondary phases [23]. Thus, even though polyphosphate treatments are demonstrated to be very effective, the surface chemistry involved in their interactions with calcium carbonates is sorely understudied, having been explored more extensively in the realm of simulations than in experiments [24].

In summary, all of the above studies and applications of $CaCO_3$ chemistry are related to dissolution and crystallization, whether natural minerals or materials for industrial applications. Therefore, it is valuable to understand the structure, process, and kinetics during dissolution and crystallization.

1.2 Calcium carbonate ($CaCO_3$)

In this thesis, I focus on two calcium carbonate polymorphs: calcite and aragonite. Calcite crystallizes in a hexagonal unit cell with a trigonal space group, where the cleavage of $(10\bar{1}4)$ face shows the typical calcite rhombohedral crystal structure [25]. This face is non-polar since calcium and carbonate ions alternate on the surface. Aragonite crystallizes in an orthorhombic unit cell and space group, and its (010) and (110) faces are mostly seen in natural forms [26]. These two faces are polar, with the outermost layer either calcium terminated or carbonate terminated (Figure 1.1a). Figure 1.1b further shows the calcium-terminated aragonite (110) face, with calcium ions exposed on the outermost surface [27]. Based on calculations by others [25], the surface energy of the calcite $(10\bar{1}4)$ face is much lower than aragonite (010) and (110) faces. This is the reason why calcite is more thermodynamically stable than aragonite. For aragonite, the surface energy of the calcium-terminated face is smaller than that of the carbonate-terminated face, which suggests that the former is more thermodynamically stable. For hydrated aragonite, the calcium face is thermodynamically stabilized by hydration due to the decrease of surface energy, but the carbonate face is thermodynamically destabilized during the hydration [27].

1.2.1 $CaCO_3$ dissolution

As $CaCO_3$ is immersed in solution, there is one reversible reaction, which is dissolution and crystallization. Dissolution refers to the release of Ca^{2+} and CO_3^{2-} ions as $CaCO_3$ solids dissolved in solution. Crystallization is the reverse reaction of dissolution, which is the process of reprecipitation of Ca^{2+} and CO_3^{2-} free ions from solution to solid [29]. The $CaCO_3$ dissolution and crystallization equilibrium is shown in Equation 1.1.

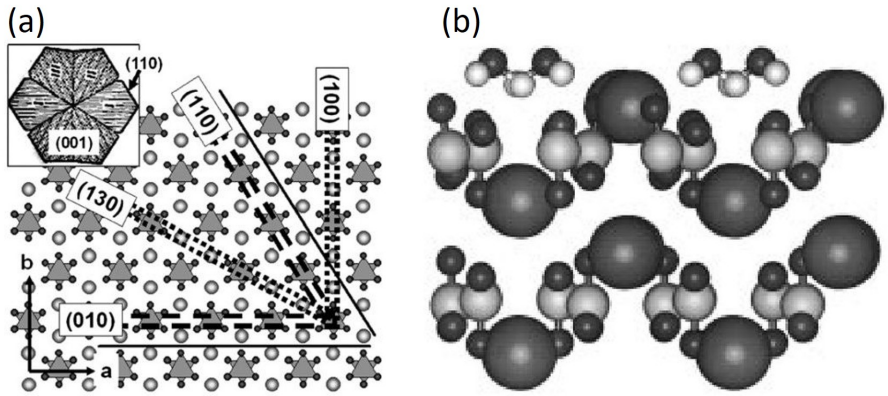

Figure 1.1: (a) The top view of the aragonite (001) surface, with triangles standing for carbonate ions and grey dots standing for calcium ions. The (110) and (010) faces are drawn with broken lines and solid lines. Broken lines show the carbonate-terminated outermost surface and solid lines show the calcium-terminated outermost surface. The (100) and (130) non-polar faces are drawn with dashed lines. (b) The top view of the calcium-terminated aragonite (110) face. Large black dots represent calcium ions. Small black and gray dots represent carbon and oxygen atoms, respectively.
This figure is adapted from [27,28]. Figure (a) [28] is reused with the permission of Elsevier. Figure (b) is adapted with permission from [27] Nora H. de Leeuw and Stephen C. Parker "Surface structure and morphology of calcium carbonate polymorphs calcite, aragonite, and vaterite: an atomistic approach" *The Journal of Physical Chemistry B.* 1998;102(16):2914-2922. Copyright 2022 American Chemical Society.

$$CaCO_{3(s)} \rightleftharpoons Ca^{2+}_{(aq)} + CO^{2-}_{3(aq)} \tag{1.1}$$

During dissolution and crystallization, there are three conditions considered in solution [30].

- Undersaturated: This is the condition in which dissolution is more dominant than crystallization. More and more solids dissolve until solution reaches saturation.
- Saturated: This is the condition in which the dissolution rate equals the crystallization rate so that the overall reaction reaches equilibrium.
- Supersaturated: This is the condition in which the dissolved solute is more abundant than in the saturated state, resulting in its tendency to precipitate (crystallization).

The solubility product constant (K_{sp}) is the equilibrium constant to describe saturated solution of ionic compounds [31]. In some cases, the pK_{sp} is also used to indicate the solubility product constant, which is the -log of K_{sp}. As seen in Equation 1.2, the K_{sp} of $CaCO_3$ is determined by ion activity of dissolved Ca^{2+} and CO_3^{2-} ions ($[Ca^{2+}]_{eq}$, $[CO_3^{2-}]_{eq}$) at equilibrium situation [32]. In this case, the ionic activities of $Ca^{2+}$and CO_3^{2-} and their ionic concentrations can be interchanged. Therefore, ion concentration is commonly used in K_{sp}.

$$pK_{sp} = -\log([Ca^{2+}]_{eq}[CO_3^{2-}]_{eq}) \tag{1.2}$$

According to pK_{sp} values for each polymorph, the solubility of calcite (pK_{sp}= 8.48) is slightly lower than that of aragonite (pK_{sp}= 8.34) under ambient conditions (25 °C, 1 atm pressure) [33]. In other words, aragonite dissolves more Ca^{2+} and CO_3^{2-} ions

than calcite to achieve equilibrium. Assuming that aragonite is dissolved in water, as aragonite reaches saturation in solution, the concentration of dissolved Ca^{2+} and CO_3^{2-} is supersaturated with respect to calcite. In this case, calcite will crystallize. However, the kinetics that influence the time scale of this process is not defined by the solubility product.

The dissolution of $CaCO_3$ can be considered from a crystal face perspective. Aragonite (110) and (010) are polar faces (Figure 1.1a), and neutral, acidic environments easily trigger protonation of the outermost carbonate ions. Thus, the dissolution of aragonite causes the disappearance of (110) and (010) faces and exposes non-polar crystal faces, such as (100) and (130) [28]. As seen in Figure 1.1a, both calcium and carbonate ions alternate on (100) and (130) faces, causing electrically neutral surfaces. Since calcite's dominant face $(10\bar{1}4)$ is nonpolar, it is more thermodynamically stable than aragonite when exposed in water. This provides another explanation for why calcite is slightly less soluble than aragonite.

In reality, however, the dissolution of $CaCO_3$ is more complicated. Carbon dioxide pressure, pH, salinity and temperature are all factors affecting the solubility of calcium carbonate [34, 35]. For example, if some reactions causes the CO_3^{2-} dissolved from $CaCO_3$ to be continuously consumed, then the dissolution of $CaCO_3$ would continue until equilibrium. This scenario can be described in acidic environment. In acidic pH, two other reactions often accompany dissolution [36]. One is the protonation of carbonate (Equation 1.3). The other one is the interaction of $CaCO_3$ with carbonic acid, generating calcium and bicarbonate ions (HCO_3^-) (Equation 1.4). Carbonate ions are consumed continuously in acidic environments, resulting in continuous calcium carbonate dissolution until equilibrium.

$$CaCO_{3(s)} + H^+_{(aq)} \rightarrow Ca^{2+}_{(aq)} + HCO^-_{3(aq)} \tag{1.3}$$

$$CaCO_{3(s)} + H_2CO_{3(aq)} \rightarrow Ca^{2+}_{(aq)} + 2HCO^{-}_{3(aq)} \tag{1.4}$$

1.2.2 $CaCO_3$ crystallization

The crystallization process of $CaCO_3$ involves nucleation of ion clusters to form amorphous calcium carbonate (ACC), followed by the growth of crystalline $CaCO_3$ polymorphs [37]. ACC is a metastable precursor of crystalline $CaCO_3$ [38]. Overall, $CaCO_3$ crystallization is driven by the supersaturation state [39], where the bulk free energy from old phase (free ions) to new phase (solid) is thermodynamic favored. In other words, the driving force of the free energy change (Δu) is the real-time ion activity product (AP) of $CaCO_3$. Although not identical to AP, real-time ion concentration can be used interchangeably under most circumstances. $AP_{(CaCO_3)}$ is given by Equation 1.5, where $[Ca^{2+}]$ and $[CO_3^{2-}]$ represent the real-time ion concentration.

$$AP_{(CaCO_3)} = [Ca^{2+}][CO_3^{2-}] \tag{1.5}$$

Equation 1.6 shows that as long as the solution is in a supersaturated state (value of AP is larger than K_{sp}), the bulk free energy change (Δu) favors the $CaCO_3$ crystallization [40]. K_B and T in Equation 1.6 represent the Boltzmann constant and absolute temperature, respectively.

$$\Delta u = K_B T \ln(AP/K_{sp}) \tag{1.6}$$

For $CaCO_3$ crystallization, two theories have been discussed for decades: classical theory and non-classical theory. The big difference between these two theories is the mechanism of cluster nucleation.

1.2.2.1 Classical theory

Cluster nucleation is based on the stochastic fluctuations involving random individual particle (ion, atom) attachment [41]. The cluster nucleation at the early stage is impeded due to the particles' solid/liquid interface [42]. In other words, the cluster interfacial energy is higher than the bulk free energy, causing an energy barrier. Such energy barrier is overcome as clusters gather to a critical size so that the bulk free energy surpasses the interfacial energy [43]. Therefore, clusters are metastable, and the nucleation of critical-sized clusters is the rate-limiting step.

As mentioned above, bulk free energy (Δu) is highly correlated with supersaturation. In other words, higher supersaturation induces a larger bulk free energy change. Equation 1.7 describes the effect of supersaturation and interfacial energy on nucleation rate [44].

$$\Delta g_n = A\exp(-B\alpha^3/\sigma^2) \tag{1.7}$$

σ and α indicate supersaturation and interfacial energy, respectively. Δg_n represents an energy barrier that determines the kinetics of nucleation. In short, a lower energy barrier (Δg_n) leads to smaller nucleation time. Coefficient A and B groups all other factors besides supersaturation and interfacial energy. Therefore, when interfacial energy (α) stays constant, the supersaturation (σ) and energy barrier (Δg_n) retain their reciprocal relation [45]. In other words, the higher the supersaturation, the smaller the Δg_n, and the faster the nucleation rate.

1.2.2.2 Non-classical theory

In recent studies, others [46] found stable prenucleation clusters during the early stage of $CaCO_3$ nucleation. Such prenucleation clusters could form even in undersaturated

conditions [47]. In addition, the aggregation of prenucleation clusters requires only a small energy barrier to be overcome [41]. All of these observations contradict the classic theory. More interestingly, the growth of prenucleation clusters follows oriented attachment [48], causing unique structures of ACC that point directly to specific long-range ordered $CaCO_3$ phases [49,50]. In other words, $CaCO_3$ phase selectivity happens in the ACC precursor. Recent studies [51]show pH-dependent ACC structures, with neutral pH favoring proto-calcite ACC and alkaline pH favoring proto-vaterite ACC. Others [52] also found proto-aragonite ACC with Mg^{2+} incorporated in the structure.

1.3 Calcium carbonate - phosphate ion system

In this section, I summarize others' works on the interaction between phosphate ions and calcium carbonate. This thesis describes two kinds of phosphates: polyphosphate and orthophosphate. Polyphosphates are composed of long (multiple) chain phosphate units that form relatively large molecules. In contrast, orthophosphate is a much smaller molecule with only one phosphate unit. The influence of pH and phosphate concentration are discussed below. It is worth mentioning that the definition of high or low phosphate concentration varies, without a universal agreement on the boundary of a low concentration regime. Qualitatively, low concentration is used to avoid any phosphate mineral precipitation, only to study phosphate adsorption on a surface. High concentration is used for studying calcium phosphate precipitation.

1.3.1 Polyphosphate

For polyphosphate, I chose sodium hexametaphosphate ($Na_6(PO_3)_6$, SHMP) for this study. As seen in Figure 1.2, SHMP consists of six phosphate units forming one hexamer. SHMP has two different phosphate functional groups: P=O and PO^-Na^+. At

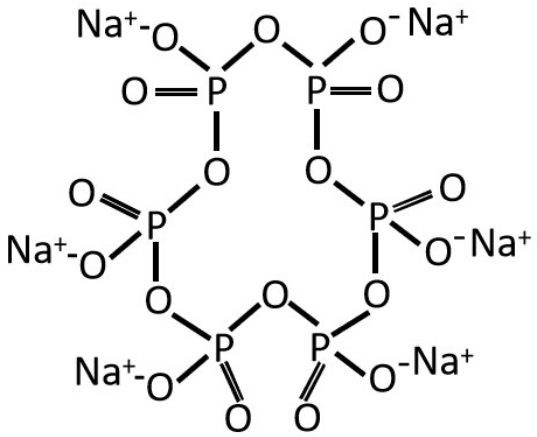

Figure 1.2: Chemical structure of sodium hexametaphosphate.

different pH conditions, $PO^{-}Na^{+}$ can also be classified as P-OH (acidic) and P-O^{-} (alkaline). Based on other's work [24], as pH changes from 2 to 12, the main SHMP species in aqueous solution are $H_4(PO_3)_6^{2-}$, $H_2(PO_3)_6^{4-}$ and $(PO_3)_6^{6-}$, respectively. In other words, the more alkaline the environment, the more pronounced the deprotonation of SHMP is in solution.

For the interaction of SHMP with calcium carbonate ($CaCO_3$), others [21] have simulated it by calculating the potential energy of SHMP/calcite $(10\bar{1}4)$ surface system. The adsorption configuration between SHMP and calcite has two possibilities: one is the P=O group pointing toward the calcite surface, and another one is the P-OH or P-O^{-} pointing towards the calcite surface. From calculations, the interaction between SHMP functional groups with calcite is in the order of P-O^{-} > P=O > P-OH. According to the charge of SHMP functional groups, with the dissolution of calcite, the electrostatic interaction between P-O^{-} and Ca^{2+} in solution is the strongest compared with P=O and P-OH. Therefore, theoretically, the SHMP uptake on calcium carbonate solid is more favorable under alkaline conditions [21].

As an anti-scaling agent of calcium carbonate, the concentration of SHMP is normally in the low concentration range (1-100 mg/L [24,53]). Therefore, very few works

can provide experimental insight on SHMP-calcium carbonate interaction, especially at the solution-solid interface. Many chemistry mechanisms remain unknown, such as how SHMP is incorporated into the carbonate particles. Is it at the surface only? Is there any secondary phosphate phase? Is it a crystalline phase? This is one of the reasons driving my research on this topic.

1.3.2 Orthophosphate

Since orthophosphate contains isolated phosphate units, the interaction between phosphate and $CaCO_3$ can be understood in a more general way by looking at orthophosphate's behavior on $CaCO_3$ surface. Normally, orthophosphate species in aqueous solution have one of four forms: PO_4^{3-}, HPO_4^{2-}, $H_2PO_4^-$, H_3phosphate. The existence of these four phases highly depends on the local pH environment. In acidic environments, phosphate ions are more protonated, with $H_2PO_4^-$, H_3PO_4 dominating in solution. In alkaline environments, HPO_4^{2-} and PO_4^{3-} become more prevalent in solution. Thus, the corresponding phosphate conjugated salts are obtainable by controlling pH.

Others [54] reported that the adsorption of phosphate on $CaCO_3$ is mainly due to the electrostatic interaction between calcium and phosphate ion. Since calcium-terminated faces are predominant in aragonite, the phosphate coverage on aragonite surface can be considerable. Solids containing both calcium and phosphate have many variations, including brushite ($CaHPO_4{\cdot}2H_2O$) and hydroxyapatite ($Ca_{10}(PO_4)_6(OH)_2$, HAp) [55].

1.3.2.1 Low phosphate concentration

In an environment with low phosphate concentrations, the phosphate may not be irreversibly incorporated into a $CaCO_3$ surface. Others did an experiment by adding

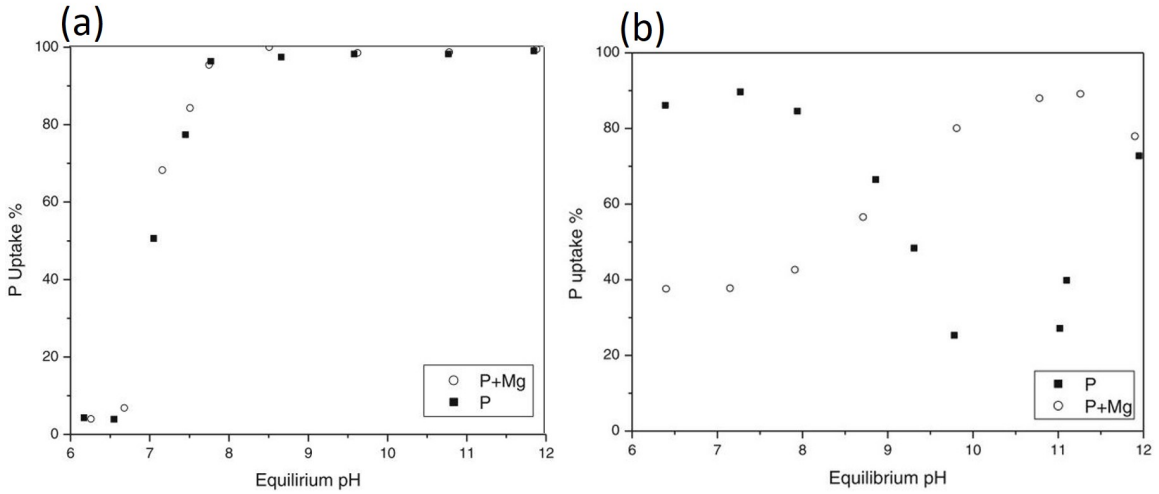

Figure 1.3: Phosphate uptake of calcite with (a) 0.32 mM phosphate solution (black solid dots) and (b) 6.45 mM phosphate solution (black solid dots). For this thesis, I am not discussing the P+Mg case (open dots in the plot).
This figure is adapted from [57] and reused with the permission of Springer Nature BV.

orthophosphate ($\leq 50\ \mu$M) in a calcite suspension [56]. They demonstrated this result by showing fast phosphate uptake during the adsorption, following by the quick and complete phosphate desorption in pure water, which suggests the phosphate doesn't incorporate into the calcite crystal [56]. Others [57] studied the low concentration (0.32 mM) phosphate uptake of calcite in different pH environments (Figure 1.3a), which shows that the phosphate uptake increases as the pH becomes more alkaline. In acidic solution, the protonated phosphate ions compete with carbonate or bicarbonate ions to adsorb onto the calcite surface. As pH increases, less free carbonate ions and more de-protonated phosphate cause greater phosphate adsorption [56].

1.3.2.2 High phosphate concentration

At higher phosphate concentrations, the phosphate uptake as a function of pH is quite different (Figure 1.3b) [57]. In an acidic environment (pH $\leq$ 8), the phosphate uptake is over 80% due to the quick dissolution of calcite, and precipitation of calcium

phosphate occurs. Others [58] studied this dissolution-precipitation process by soaking calcite solids in orthophosphate buffer solution (pH = 7.4, 0.2 mol/L). Based on experimental results, they confirmed the precipitation of HAp and the dissolution of calcite. As calcite is immersed in an orthophosphate buffer, the dissolution of calcite releases free CO_3^{2-} and Ca^{2+} ions. This is followed by the nucleation of small nm-scale particles containing a HAp cluster as the inner core and amorphous calcium phosphate (ACP) as an outer layer. Some of these nm-scale particles deposits on the calcite surface, generating the first layer of HAp seeds. Other nm-scale particles will continuously aggregate on the previously deposited HAp seeds, resulting in film formation. Meanwhile, calcite dissolution causes many tiny pores on the particle surface. These small pores serve as active nucleation sites and increase the surface area.

As pH increases (Figure 1.3b), the phosphate uptake initially decreases to 25% and increases back to 90% in a more alkaline environment [57]. At higher pH, the protonation of CO_3^{2-} becomes less likely, triggering less dissolution of calcite, and the dissolution-precipitation process is unlikely. Therefore, a phosphate ion adsorbs directly on the calcite surface, followed by calcium phosphate formation. Besides HAp, $CaHPO_4$ also prevails in a mildly alkaline regime. This is reasonable since HPO_4^{2-} is the dominant orthophosphate species between pH 7-10. In a profoundly alkaline environment, HAp is still the most preferred calcium phosphate phase [59]. Others found that unstable ACP was first precipitated, then crystallized into the HAp phase [60].

1.3.2.3 Overview

Others [61] have summarized an overall picture of calcium carbonate - orthophosphate interactions (Figure 1.4). For a low phosphate concentration, the phosphate

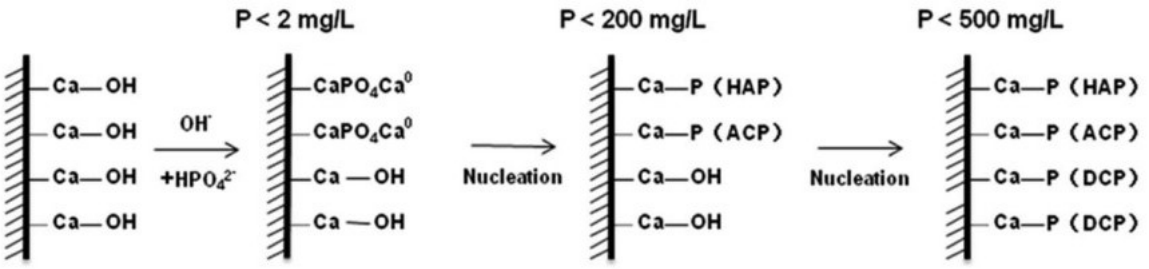

Figure 1.4: Schematic diagram of phosphate ion - calcium carbonate interaction with increasing phosphate concentration in a mildly alkaline environment.
This figure is adapted from [61] and reused with the permission of Royal Society of Chemistry.

ion may only experience adsorption, generating a phosphate complex ($CaPO_4Ca^0$) on the calcium carbonate surface. In a highly concentrated phosphate environment, ACP is initially precipitated on the surface as an intermediate precursor. Then several calcium phosphate phases could start to crystallize. The phosphate uptake and calcium phosphate phase will depend greatly on the pH environment.

1.4 Primary characterization methods

My research work focuses on tracking changes that happen in solid materials, both in their bulk and at their surface. One of the main aspects of this thesis is to investigate the effect of the interfacial interaction between phosphate and $CaCO_3$ during the dissolution and recrystallization. To get a full picture, I used different characterization methods, including Fourier transform infrared spectroscopy (FTIR) and Solid-state nuclear magnetic resonance (ssNMR). In this section, I will explain what FTIR and ssNMR can teach us about the sample. We used other material characterization techniques as well, which are mentioned in later chapters of this thesis.

1.4.1 Attenuated total reflectance-fourier transform infrared spectroscopy (ATR-FTIR)

ATR-FTIR is a technique based on the total internal reflection of the infrared (IR) beam at the boundary between the sample and the internal reflection element (ATR crystal) [62]. Overall, the incident beam enters the ATR crystal at a certain angle, illuminating the sample with broadband IR. At the same time, the reflection of the incident beam induces an evanescent wave that penetrates the sample [63]. Atoms absorb energy from evanescent waves only at characteristic energies related to vibrational modes, causing a specific vibrational motion. IR energy absorption occurs only when vibrations change the dipole moment of molecule [64]. The intensity of the evanescent wave decays as the distance it penetrates through the sample increases [65]. Typically, the penetration depth is between 0.5 and 5 μm, which can be deep into the bulk of powdered materials. The spectrometer modulates the IR beam in real time, and the accompanying Fourier software converts the raw interferogram into a spectrum, showing what IR energies are absorbed by the sample and producing IR peaks at specific wavenumbers (cm^{-1}) in the spectrum. Therefore, as IR active substances absorb specific IR energy related to their unique vibrational modes, the corresponding IR peak positions in the spectra help identify the composition of the sample.

1.4.1.1 Why choose ATR-FTIR?

Since the samples I studied are solid, the advantage of ATR-FTIR over traditional transmission FTIR, from an operational point of view, is the simple sample preparation. For transmission FTIR, solid powders must be diluted with potassium bromide (KBr), then pressed into an IR-transparent pellet, to allow transmission. For ATR-FTIR, however, the powders need only be pressed against the ATR crystal to ensure

close contact.

The penetration depth of the evanescent wave in $CaCO_3$ is 0.5 and 5 μm, indicating that the entire bulk of the $CaCO_3$ solid may not contribute to the ATR-FTIR that we record. However, I grind each solid sample before ATR-FTIR measurements, which means more of the bulk has been exposed. Therefore, ATR-FTIR can identify solid powder containing both bulk and surface information. Moreover, ATR-FTIR spectra can help to identify not only crystalline materials but compounds with poor crystallinity or even amorphous phases.

ATR-FTIR is a characterization method that can easily identify solid phases and provide qualitative or quantitative information on phase changes based on relative peak intensities. Although ATR-FTIR offers valuable details on the solid phases, it cannot investigate the details of the surface structure between phosphate and calcium carbonate.

In this thesis work, I use ATR-FTIR as the first characterization tool to validate the experimental results after each trial of the experiment, before moving to other more time-consuming characterization methods.

1.4.2 Solid-state nuclear magnetic resonance (ssNMR)

Nuclear magnetic resonance (NMR) is a technique based on measuring local magnetic fields (magnetization) around atomic nuclei during exposure of an external magnetic field [66]. Such nuclear spin interaction with an external magnetic field (B_o) is called the Zeeman interaction [67]. As active nuclei absorb electromagnetic radiation, the energy difference between two spin states (-1/2, 1/2) is related to the external magnetic field strength. This energy difference can be denoted as the frequency with the unit of MHz. Equation 1.8 shows the relation between frequency and external magnetic field, where ν stands for radio frequency and γ is gyromagnetic moment [68].

$$\nu(Hz) = \frac{B_o \gamma}{2\pi} \tag{1.8}$$

Some internal nuclear spin interactions, such as chemical shielding and dipole-dipole coupling, are orientation-dependent interactions (anisotropic). For instance, chemical shielding describes the magnetic field of nuclei shielded by the surrounding electrons [69]. The electrons that surround the nucleus are in motion (electronic current), so electrons create their own electromagnetic field. Dipolar coupling is a through-space interaction with neighboring nuclei [70]. In solution, the rapid tumbling of molecules in solution can average the anisotropic interactions. Therefore, solution-state NMR can achieve high-resolution spectra. However, ssNMR is the one that deals with solid materials. Powder samples consist of many rigid crystallites with random orientations, causing anisotropy effect. For instance, the chemical shielding describes the nuclei experiencing shielded external field. Since each nuclei in the solid has a fixed orientation, the shielded external field is orientation-dependent and thus anisotropic. Moreover, in a solid-state sample, anisotropic effect of dipole couplings is also inevitable since each magnetic spin is coupled to other magnetic spin in its local environment [71]. Normally, Zeeman interaction energy is much larger than other anisotropic interactions [72]. But these anisotropic interactions can perturb the Zeeman interaction, causing peak broadening and peak shift in the ssNMR spectra.

One of the methods to suppress the influence of anisotropic interaction in ssNMR is by introducing an artificial spinning at a magic angle ($\beta_M = 54.74^o$) with respect to an applied magnetic field (B_o) [73]. The rate of magic angle spinning should be equal to or larger than the span of the anisotropic tensor so as to eradicate the anisotropic effects.

1.4.2.1 ssNMR experiment strategies

Direct excitation (DE, also known as Chemical Shift Echo (CSE)) is a ssNMR technique that can provide quantitative information. The population of detected nuclei is quantifiable by peak integration. However, some NMR-active nuclei are low abundance in nature; in our case, ^{13}C in natural abundance carbon is only 1%. For this reason, isotopic enrichment is often preferred to increase signal [74].

Cross polarization (CP) is focused on investigating the dilute nuclear spins such as ^{13}C. Low abundance nuclei usually suffer from the poor signal intensity. During CP, the polarization from the high natural abundance spin (in our case, ^{1}H) is transferred to the diluted spin (in our case, ^{13}C). In this case, ^{13}C acquire magnetization from nearby ^{1}H nuclei [75]. In our case, CP selectively enhances ^{13}C signal that is close to hydrogen atoms. In ^{13}C CP ssNMR, the polarization from proton to rare ^{13}C result in the enhancement around hydrogen-rich environments, providing a higher signal:noise ratio [76].

Rotational-echo, double-resonance (REDOR) NMR is used to measure heteronuclear dipolar coupling [77]. Dipolar coupling is the interaction of one nuclear spin with a magnetic field generated by another nuclear spin. Equation 1.9 shows the strength of dipolar coupling (d) is distance-dependent ($1/r^3$), where u_0 in the equation is vacuum permittivity, r is the distance between two nuclei, γ^I and γ^S are gyromagnetic ratio of coupled spin, h is Planck's constant [78].

$$d = \frac{u_0 h}{4\pi} \frac{1}{r^3} \gamma^I \gamma^S \tag{1.9}$$

Therefore, the signal of REDOR can help to estimate the internuclear distance. In other words, the stronger the dipole interaction, the closer the internuclear distance would be, and vice versa. In my case, I investigate the dipolar interaction between

^{13}C and ^{31}P to understand the molecular structure of phosphate-$CaCO_3$ interaction.

1.4.2.2 Why choose ssNMR?

With regard to experiments, ^{13}C and ^{31}P DE ssNMR is a tool that has provided many interesting insights about $CaCO_3$ and secondary phosphate phases. This is due to the fact that crystalline, disordered and amorphous phases can be distinguished by comparing chemical shift and peak width differences due to subtle differences in the immediate chemical environment of target nuclei [79,80]. Moreover, the population of detected nuclei is quantifiable by integrating their distinctive chemical shift peaks [51].

For $CaCO_3$-related materials, ^{13}C CP ssNMR only detects the ^{13}C that is adjacent to proton (^1H) environments. In other words, only the ^{13}C signal that is coupled by ^1H is acquired in the spectrum. If $CaCO_3$ samples contain structural water or organic additives, the appearance of carbonate ^{13}C signal in CP spectra means that there are some carbonate-containing environments that are proton-rich [81]. Therefore, an interfacial carbonate environment between the bulk solid and bulk solution can provide a strong CP signal [82]. CP can also investigate the homogeneity of proton (structural water) distribution in the local structure of $CaCO_3$ [51]. However, CP is not possible for the pure crystalline polymorphs (calcite and aragonite) in a hydrogen-atom-free environment.

REDOR can provide great help in understanding the phosphate-$CaCO_3$ interaction at the atomic level, based on obtaining the inter-nuclear distance between ^{31}P and ^{13}C. For example, our collaborators [83] once used REDOR to help explain the molecular mechanisms by which phosphate additives govern amorphous calcium carbonate (ACC) stability, phase transition, and crystallization.

Overall, ssNMR not only identifies and differentiates the various phases of $CaCO_3$, but also gives information about the uniformity of the $CaCO_3$ structure (bulk and

interface). More importantly, ssNMR gives quantitative information about the interfacial structure between calcium carbonate and inorganic/organic adsorbates.

1.5 Thesis outline

This thesis aims to understand the dissolution-recrystallization behavior (phase conversion) of untreated/treated $CaCO_3$ material and to learn about the solid-ion or ion-ion interaction in aqueous solution. This thesis has considered two parts: lab work and field research work.

The lab work focuses on $CaCO_3$ synthesis, $CaCO_3$ dissolution-recrystallization behaviour and phosphate-$CaCO_3$ interaction:

- Chapter 2: This chapter talks about the synthesis of $CaCO_3$, including experimental factors to control the $CaCO_3$ polymorphs. This chapter makes reference to additional work by us that has been submitted for peer review [84] (date of submission: December 6^{th} 2022).

- Chapter 3: This chapter studies the phase conversion of $CaCO_3$ in aqueous solution and further understands polyphosphate-$CaCO_3$ interaction during dissolution and recrystallization. This chapter is a draft manuscript that will be submitted for peer-reviewed publication.

- Chapter 4: This chapter compares polyphosphate and orthophosphate as they interact with $CaCO_3$ in aqueous solution. It also describes the thermal stability of phosphate treated $CaCO_3$. This is a manuscript accepted by 'Solids' journal [85].

Chapter 5 and Appendix A are related to field research work, providing another way to observe and infer dissolution and recrystallization of naturally occur-

ring $CaCO_3$. Through the identification of natural minerals and the understanding of the surrounding environment, I can gain insights about mineral deposition and their phase transformations

1.6 Copyright and authorship statement

This thesis contains a series of manuscript-style chapters; all are manuscripts that are in preparation for submission to peer-reviewed journals. For all the Chapters, I carried out the experiments, and data analysis. My supervisor, Dr. Kristin M. Poduska, provided me with theoretical and experimental guidance. In Chapter 3, Dr. Asher Schmidt and Dr. Shifi Kababya (Technion (Israel)) conducted the solid-state NMR experiments and data analyses. In Chapter 5, the field research trip was conducted by the leadership of Dr. Penny L. Morrill.

Figures 1.1 was reused with the permission of the Elsevier and American Chemical Society, respectively. Figure 1.3 was reused with the permission of the Springer Nature BV. Figure 1.4 was reused with the permission of the Royal Society of Chemistry. All others are my own.

Chapter 2

Phase-specific calcium carbonate synthesis strategies

This chapter discusses the synthesis of calcium carbonate. Several experimental factors, such as temperature, additives and solvents, control the phase of calcium carbonate. Overall, the main goal is to find a reproducible and relatively easy way to form calcite and aragonite, since the experiments in the following chapters (Chapter 3 and Chapter 4) require calcite and aragonite as starting materials.

As the first author, I designed the experiment and contributed to the material synthesis, data collection and analysis. Dr. Kristin M. Poduska helped guide the theory and methodology of the experiments. This chapter makes reference to additional work by us that has been submitted for peer review [84] (date of submission: December 6^{th} 2022).

2.1 Literature overview

Many different synthesis strategies are reported in the literature to form calcium carbonate, including solution precipitation, gas carbonation (such as CO_2 bubbling), and reverse emulsion [86]. Each method has different advantages for producing specific polymorphs, particle sizes, and crystallite morphologies.

2.1.1 CO_2 bubbling method

Among these methods, most industrial processes use CO_2 bubbling to produce calcium carbonate ($CaCO_3$). It involves the calcination of limestone (a mineral composed of $CaCO_3$), followed by slaking of quicklime (calcium oxide (CaO)). Finally, CO_2 is bubbled through the slaked lime (Calcium hydroxide ($Ca(OH)_2$)) to precipitate $CaCO_3$ particles [87]. The series of reactions are:

$$CaCO_{3(s)} \rightarrow CaO_{(s)} + CO_{2(g)} \tag{2.1}$$

$$CaO_{(s)} + H_2O_{(l)} \rightarrow Ca(OH)_{2(aq)} \tag{2.2}$$

$$Ca(OH)_{2(aq)} + CO_{2(g)} \rightarrow CaCO_{3(s)} + H_2O_{(l)} \tag{2.3}$$

An advantage of the bubbling method is that it can produce nm-sized $CaCO_3$ particles. The particle sizes can be adjusted by controlling CO_2 flow rate, pressure, and stirring rate [88,89]. These parameters are relatively easy to control even in large-scale industrial processes. Calcite is the most common phase in the CO_2 bubbling method. The formation of other phases, such as aragonite, requires the addition of additives, such as polyacrylamide or ethylenediamine tetraacetic acid (EDTA) [90,91].

2.1.2 Solution precipitation method

Another widely used method for $CaCO_3$ synthesis is solution precipitation. Mixing calcium ions with carbonate ions in aqueous solutions causes rapid precipitation (Equation 2.4):

$$CaCl_{2(aq)} + Na_2CO_{3(aq)} \rightarrow CaCO_{3(s)} + 2NaCl_{(aq)} \tag{2.4}$$

Aqueous precipitation of $CaCO_3$ occurs in geological settings and biological mineralization [92]. Under ambient temperature and pressure conditions, calcite is the most common polymorph produced by solution precipitation. However, polymorphs and particle sizes can be adjusted by factors such as additives or temperature [93–95].

Temperature is one of the critical factors affecting the phase of calcium carbonate. Calcite forms at room temperature and below. Aragonite precipitates when the temperature rises above 70 °C [96]. Several hypotheses are proposed in terms of the influence of temperature. A few decades ago, others thought increasing temperature causes more impurities, such as Sr or Pb cations, to be trapped in the $CaCO_3$ crystal lattice during the precipitation, which obstructs the crystal growth of calcite [97]. However, all the chemicals for our syntheses are ACS reagent grade, so the impurity possibilities may not be as relevant. Others indicated that increasing temperature might change the hydration bonding network of amorphous calcium carbonate (ACC), forming aragonite-related clusters during the nucleation [98, 99]. These clusters will go on to form ACC, then aragonite.

Another factor controlling calcium carbonate phase selection is the addition of magnesium (Mg), which is conducive to aragonite formation [100, 101]. One explanation of this observation is that Mg triggers a more significant energy barrier of pre-calcite cluster nucleation than that of aragonite nucleation, causing preferential

aragonite crystallization [102]. However, the addition of Mg ions makes the calcium carbonate system more complicated. First, Mg ion concentration significantly impacts the phases of carbonate salts. With different Mg:Ca ratios, magnesite ($MgCO_3$) and Mg-incorporated-$CaCO_3$ are all possible final products [103, 104]. Second, the behavior of Mg with other additives, such as the phosphates that are the focus of this thesis work, could also complicate the chemistry. On one hand, the introduction of Mg ion increases the surface area of aragonite/calcite particles, giving rise to more phosphate adsorption sites on the particle surface [57]. On the other hand, the Mg impacts the phosphate secondary phase formation. For instance, Mg-$CaCO_3$ can stabilize the dibasic calcium phosphate (DCP) and retard the formation of hydroxyapatite (HAp), and some magnesium phosphate is also detected as more Mg involved [61].

The solvent effect on calcium carbonate phase control has also drawn attention. Others [105] have found that calcium (Ca^{2+}) and carbonate (CO_3^{2-}) ions have different solvation tendencies in water-ethanol mixtures, resulting in local inhomogeneity. In other words, the solvation of Ca^{2+} and CO_3^{2-} in water and ethanol is quite different in that the CO_3^{2-} is mainly solvated by water, while Ca^{2+} is solvated by both water and ethanol. Therefore, the calcium carbonate phase is controlled by solvent polarity (ethanol:water ratio). Others found that a mixture of ethanol and water as the solvent can form aragonite, vaterite, and even ACC [106, 107]. The synthesis of ACC is of great significance in terms of following crystallization and different precursor phases [108, 109].

2.2 Solution precipitation of calcite and aragonite

In general, solution method and bubbling method each have advantages and disadvantages. The bubbling method is more efficient in particle size controlling, which

is sought after industrial process. In the solution method, although the crystal size can be fine-tuned by slowing the mixing rate [93], size control is still too limited compared with the bubbling method. However, the synthesis procedure of the solution method is simpler, and phases are more easily controlled. For example, aragonite is easily formed simply by raising the temperature in solution. In contrast, phase control by bubbling requires a more complex procedure, and forming a relatively pure aragonite phase is challenging. Since one of my research projects is to explore the $CaCO_3$ phase conversion in the aqueous solution, it is essential to find an easy way to synthesize pure calcite and aragonite phases as the starting materials. Therefore, phase control is more important than crystal morphology and crystal size. Thus, I chose temperature-controlled solution precipitation as the primary method.

2.3 Experimental procedure

I made calcium carbonate precipitates by adding 25 mL 60 mM Na_2CO_3 (pH 10.9) solution in 25 mL 60 mM $CaCl_2$ (pH 7.2) solution drop by drop over a duration of 3 min, while stirring at 400 rpm to help prevent heterogeneous crystallization. Calcite was precipitated at room temperature, making a pH of 8.8 in the final supernatant. The aragonite was formed at 90 °C, making a pH of 8.6 in the final supernatant. I separated precipitates from the suspension by centrifugation (4000 rpm for 10 min) and filtration, then dried the solids at room temperature for 12 hours.

2.3.1 Infrared spectra of calcium carbonate standards

One primary method to identify calcium carbonate phases is infrared (IR) spectroscopy. There are four common carbonate vibrational modes, ν_1: symmetric stretch, ν_2: out-of-plane bending, ν_3: asymmetric stretch and ν_4: in-plane bending [110]. Fig-

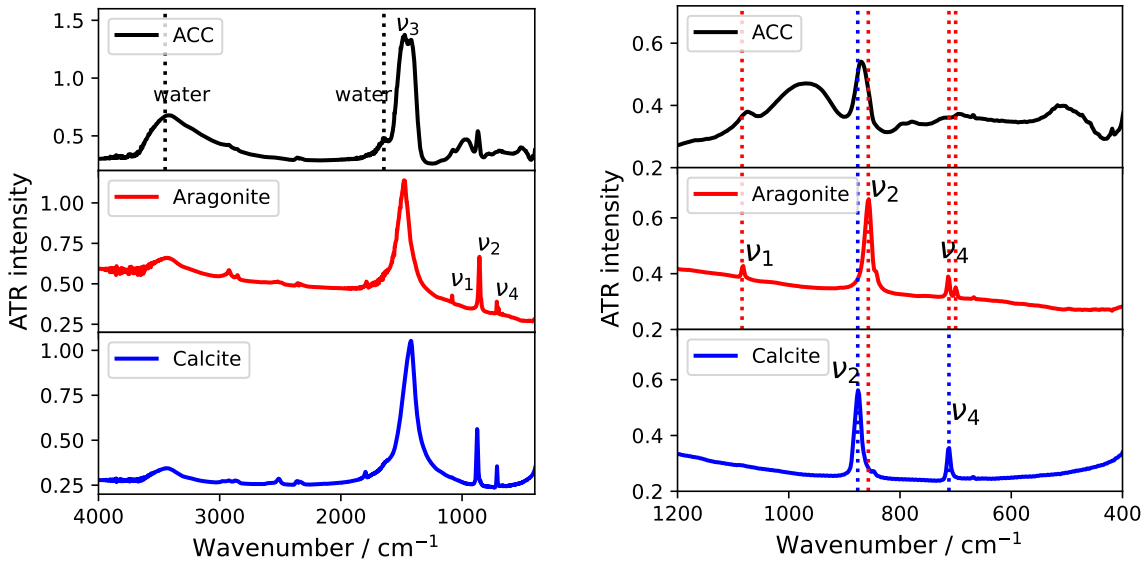

Figure 2.1: Transmission FTIR data of calcium carbonate polymorphs: calcite, aragonite and amorphous calcium carbonate (ACC). Left: full spectra. Right: Emphasizing the ν_2, ν_4 and ν_1 peaks. The black dotted lines with band labels correspond to water peaks, while blue and red dotted lines shows the vibration peaks of calcite and aragonite, respectively.
Polymorph assignments are based on comparisons using mineral spectral libraries [1]

ure 2.1 shows a standard mid-IR spectra of calcium carbonate phases based on mineral spectral libraries [1]. Four typical carbonate vibration peaks (ν_3, ν_1, ν_2 and ν_4) are labelled in the plot. Due to the difference in the crystal structure, each polymorph (phase) has a unique IR spectrum. For example, the ν_2 peak of aragonite (854 cm^{-1}) has a lower energy compared to that of calcite (872 cm^{-1}) (Figure 2.1 Right). Moreover, aragonite has a distinct doublet ν_4 peak and a ν_1 peak at 1100 cm^{-1} [111] (Figure 2.1 Right). These peak differences are used to distinguish between calcite and aragonite. Compared with calcite or aragonite, the IR peaks of ACC show wider widths, and some peaks even disappear, such as ν_2 and ν_4 peak (Figure 2.1 Right). In addition, ACC contains a large amount of structural water compared to calcite and aragonite, which appears as strong OH vibration peaks (3400 cm^{-1} and 1620 cm^{-1}) in the IR spectra (Figure 2.1 Left).

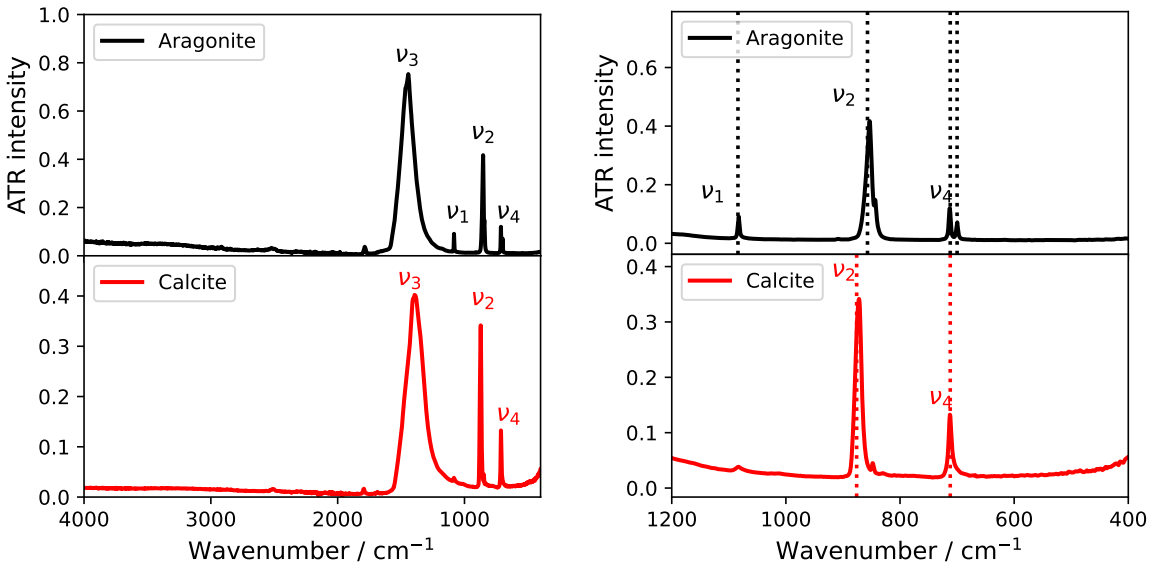

Figure 2.2: Representative ATR-FTIR spectra of synthesized calcite and aragonite. Left: full spectra. Right: Emphasizing the ν_2, ν_4 and ν_1 peaks. The black dotted lines and red dotted lines represent the vibration peaks of aragonite and calcite, respectively.

2.3.2 ATR-FTIR of synthesized calcium carbonate

I confirmed the synthesized calcite and aragonite by IR, whose vibration peaks showed typical calcite and aragonite features (Figure 2.2). For instance, the ν_2 peaks of aragonite and calcite are different in position (854 cm^{-1} and 872 cm^{-1}). Moreover, aragonite solid has unique ν_1 peak and doublet ν_4 peaks. Overall, my experiments validated the temperature effect, with room temperature favouring calcite and higher temperature favoring aragonite. I also attempted the synthesis of the aragonite by increasing the temperature to 70 °C, 80 °C, and 90 °C. The IR result (Figure 2.3) indicates that aragonite is the predominant phase (peak at 854 cm^{-1}). There is a small IR shoulder at 872 cm^{-1}, whose vibration is calcite-related. This IR shoulder weakens with increasing temperature, indicating that sample contained less calcite phase as temperature increases. Therefore, a higher temperature (90 °C) favors pure phase aragonite.

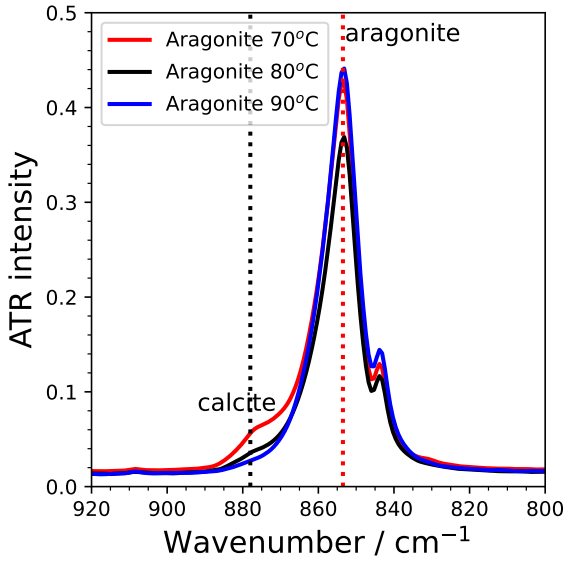

Figure 2.3: Representative ATR-FTIR spectra of the aragonite ν_2 peak. The large peak at 854 cm^{-1} is the aragonite ν_2 peak (red dashed line). The weak shoulder at 872 cm^{-1} is the calcite ν_2 (black dashed line).

2.4 Other factors

Section 2.2 only focuses on how temperature controls selective formation of either aragonite or calcite. According to others [112–114], Mg:Ca ratios, solvent and temperature influence formation of ACC, as well as calcite and aragonite. Therefore, this section describes how I used temperature, Mg additives, and solvents to form amorphous and crystalline calcium carbonate phases.

2.4.1 Magnesium and temperature

I mixed $CaCl_2$ and $MgCl_2$ in an aqueous solution to get different Mg:Ca ratios. The Ca^{2+} concentration remained at 60 mM while the Mg^{2+} concentration ranged from 0 mM to 300 mM. I placed the $CaCl_2$, $MgCl_2$ mixture solution, and Na_2CO_3 solution (60 mM, water as solvent) in the an ice bath or on a hot plate, ensuring that both solutions reached the desired temperature. Then both solutions were quickly mixed,

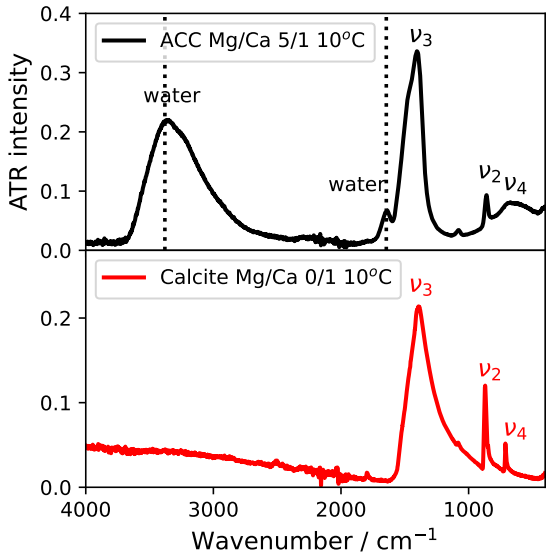

Figure 2.4: Representative ATR-FTIR spectra of synthesized calcium carbonate with the addition of Mg ion and low temperature (10°C). The black dotted lines with band labels correspond to water peaks.

followed by centrifugation to separate precipitates from supernatant. The precipitates were filtered and dried at room temperature for 12 hours.

At low temperature (10 °C), calcite phase is formed without the addition of Mg (Mg:Ca 0:1, Figure 2.4). As more Mg was added, making the Mg:Ca ratio reaches 5:1, ACC is formed. ATR-FTIR spectra (Figure 2.4) show that ACC has a strong OH features at 3400 cm^{-1} and 1600 cm^{-1}. There is also a broad ν_4 peak, which is typical of poorly crystallized (amorphous) calcium carbonate. To show the stability of ACC, the ACC solids were stored in the ambient environment for a longer period (3 days) or heated at 70 °C for 5 hours. As shown in Figure 2.5, compared to the ACC air-dried for 12 hours, the water IR peaks (3400 cm^{-1}and 1600 cm^{-1}) decreased considerably due to the loss of surface water. However, there are still significant water features left, indicating the presence of robust structural water in the ACC.

At room temperature, without adding Mg, the synthesized solid has calcite as the primary phase, as described above. After the addition of Mg (Mg:Ca 1:1), the

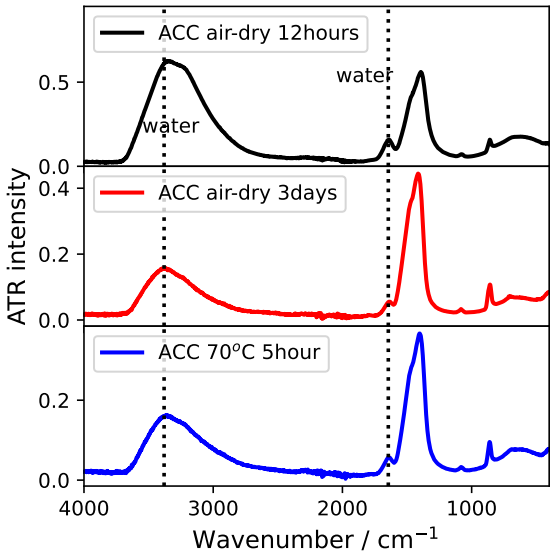

Figure 2.5: Representative ATR-FTIR spectra of synthesized ACC under different storage conditions. The black dotted lines with band labels correspond to water peaks.

aragonite and calcite ν_2 peaks appeared simultaneously (Figure 2.6), indicating the aragonite and calcite mixed phase in the solid. This confirmed that Mg is conducive to the formation of aragonite. As mentioned above, with higher synthesis temperature (70 °C), the synthesized solid is aragonite dominant. When a small amount of Mg (Mg:Ca 0.25:1) was added, the IR spectra showed a very pure aragonite solid precipitated, with no evidence of calcite ν_2 shoulders (872 cm^{-1}) in the spectra (Figure 2.6). When Mg content in the starting solution is higher (Mg:Ca 1:1 or 3:1), the calcite ν_2 shoulder (872 cm^{-1}) appeared again and peak intensity got stronger (Figure 2.6), indicating more of the calcite phase in the solid.

For Mg influence, my primary goal is to use Mg to trigger aragonite formation without incorporating Mg into the structure. Therefore, I did not try all the Mg:Ca ratios to observe the possible Mg incorporation in $CaCO_3$. What is certain is that Mg does contribute to the formation of aragonite and ACC during precipitation, as expected based on other reports in the literature [100, 101, 113].

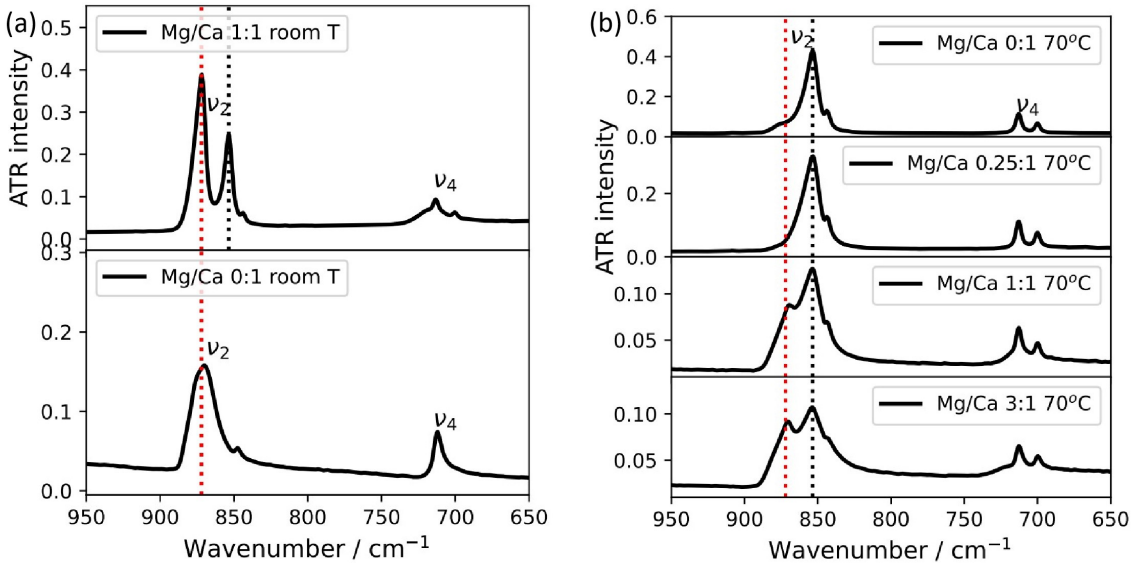

Figure 2.6: Representative ATR-FTIR spectra of synthesized calcium carbonate with the addition of Mg ion. a: precipitation at room temperature, b: precipitation at high temperature (70 °C). The spectra emphasizes the ν_2 and ν_4 peaks. The red dotted lines indicate the calcite ν_2 peak, whereas the black dotted lines indicate the aragonite ν_2 peak.

2.4.2 Solvent effect

Firstly, I tried calcium carbonate synthesis by ethanol rinsing. In this procedure, Na_2CO_3 (60 mM, water as solvent) and $CaCl_2$ solution (60 mM, water as solvent) were prepared in an ice bath, ensuring temperature around 10 °C. After I quickly mixed the solutions, I added different amounts of ethanol to the suspension immediately. The volume of ethanol added was determined by water: ethanol volume ratios (1:0, 1:0.5, 1:1, 1:2). Suspensions were then centrifuged and filtered. The solid particles were dried in an ambient environment for 12 hours.

According to the FTIR results, phases of $CaCO_3$ changed depending on the volume ratio of water:ethanol. In the absence of ethanol, the IR spectra shows only the characteristic peaks of calcite, with only calcite ν_2 and ν_4 peaks (Figure 2.7). With the addition of ethanol (water:ethanol 2:1), the FTIR shows the mixture phase of

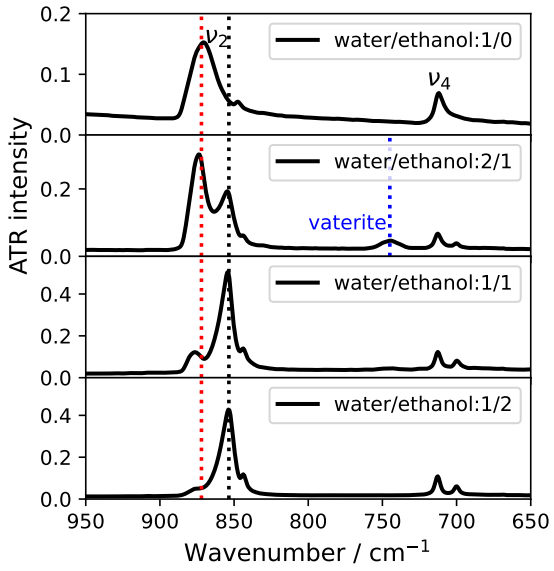

Figure 2.7: Representative ATR-FTIR spectra of synthesized calcium carbonate with different amounts of ethanol rinsing. The spectra emphasize the ν_2 and ν_4 peaks. The red dotted line indicates the calcite ν_2 peak, whereas the black dotted line indicates the aragonite ν_2 peak. The blue dotted line shows a vaterite peak.

calcite and aragonite (both ν_2 peaks in the spectra), with the calcite phase as the dominant (Figure 2.7). As more ethanol added (water:ethanol 1:1), the aragonite gradually became the dominant phase, and only small calcite ν_2 shoulder (872 cm^{-1}) left in the spectra (Figure 2.7). When water:ethanol reaches 1:2, the FTIR shows an almost phase-pure aragonite (Figure 2.7). Others [105] have found that the larger the polarity difference between ethanol and water (higher ethanol:water ratio), the more elongated the aragonite needle-shaped crystallites would form. Therefore, ethanol does support the formation of aragonite crystals. It is worth mentioning that some vaterite phases (the peak where the green dotted line is located in Figure 2.7) may occur in the solids. My experiments showed that the vaterite phase sometimes forms under low-temperature environment and can disappear immediately when the solids are re-exposed to water.

I also tried to produce amorphous calcium carbonate (ACC) by using ethanol as

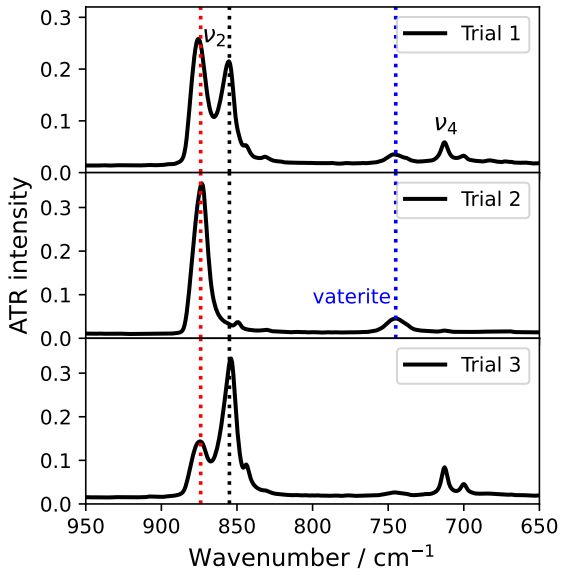

Figure 2.8: Representative ATR-FTIR spectra of synthesized calcium carbonate with ethanol as the solvent. The spectra emphasize the ν_2 and ν_4 peaks. The red dotted line indicates the calcite ν_2 peak, whereas the black dotted line indicates the aragonite ν_2 peak. The blue dotted line indicates the vaterite phase.

the solvent. 60 mM Na_2CO_3 solution was prepared using 40% ethanol as the solvent and 95% ethanol for 60 mM $CaCl_2$ solution. I placed both solutions in an ice bath until the solutions decreased to 10 °C, then mixed them together. The suspension underwent centrifuge and filtration, and the precipitates were air-dried in the ambient environment for 12 hours.

The above experimental procedure was repeated several times. Unfortunately, there is no consistent $CaCO_3$ phase observed in repeated experiments. Trial 1 and Trial 3 show the mixture phase of calcite and aragonite (Figure 2.8). In Trial 2, only calcite phase exists in IR spectra (Figure 2.8). However, the calcite phase in Trial 2 has no ν_4 peak, which is abnormal. In addition, vaterite peaks appear, which may be due to the low-temperature effect. More importantly, none of my ethanol experiments showed ACC formation, which is different from the results of others' work [106, 114].

2.5 Conclusion

This chapter summarizes all of my efforts related to calcium carbonate synthesis. I chose solution methods for syntheses because of its simple experimental procedure and easy phase control. Phase-pure calcite and aragonite can be formed only by changing the reaction temperature. I also explored the effect of Mg ions and ethanol on $CaCO_3$ phase selection. In general, both Mg and ethanol can trigger aragonite formation. Moreover, low temperature and the involvement of Mg can induce ACC formation, and the synthesized ACC remains stable even stored for a long time.

In subsequent chapter of this thesis, the main focus is using phase-pure $CaCO_3$ to study phase conversion and phosphate interactions. Therefore, phase-pure calcite and aragonite serve as important starting materials: I use room temperature to produce calcite, and increased temperatures to produce aragonite. Although Mg and ethanol contribute to aragonite formation, the final product is mostly a mixed phase of aragonite and calcite. In addition, adding Mg may lead to form other carbonates, such as magnesite. Thus, temperature-controlled solution syntheses best meet our needs. In this chapter, some related work on tracking ACC crystallization products is submitted as a paper [84].

Chapter 3

Aragonite-to-calcite thermodynamic pump: a dissolution and recrystallization study

We plan to publish the main findings in this chapter as a peer-reviewed manuscript. The authors of this paper are Boyang Gao, Dr. Kristin M. Poduska, Dr. Asher Schmidt and Dr. Shifi Kababya. Boyang Gao carried out the experiments, data collection and analysis and contributed to the writing of the manuscript. Dr. Kristin M. Poduska provided guidance on the experimental design, data analysis, and the writing of the manuscript. Dr. Asher Schmidt and Dr. Shifi Kababya (Technion, Israel) conducted solid-state NMR experiments and analyses, and helped writing the manuscript drafts, including portions of this chapter.

3.1 Introduction

Carbonate equilibria in water-based environments help to link carbon exchange between atmospheric carbon dioxide (CO_2), carbonic acid and carbonate ions, and carbonate mineral solids. Each of these carbon-containing species is highly studied in environmental science contexts, but their interplay is extremely complex, particularly since most real-life systems are out-of-equilibrium and cannot be adequately described by equilibrium balance equations [115]. This means that improving our understanding of processes such as ocean acidification, water remediation, and atmosphere-water interactions requires a better understanding of the chemistry of non-equilibrium systems.

Surface processes for calcium carbonate ($CaCO_3$) in aqueous environments are relevant for biomineralization and other kinds of research questions. As such, they have been the focus of many experimental and theoretical investigations over the last few decades. While earlier studies focused on issues such as the kinetics of crystallization and factors contributing to polymorph nucleation and growth in pure $CaCO_3$ phases [116], there has also been a strong emphasis on understanding how other ions alter the resulting products.

Few studies have studied the interplay between aragonite and calcite when they are both in aqueous environments. The mechanisms that govern phase-specific dissolution-recrystallization rates for calcite and aragonite (individually) have not been fully resolved [117]. Even so, a recent study [3] suggests that considering each element separately does not capture the most important responses of the combined system, which has important implications for marine and freshwater systems. In this work, we describe our strategy for quantitatively following the kinetics of the aragonite-to-calcite conversion of a single or mixture phase system. This includes bulk and structural characterization of the mineral particulates (before and after immersion)

and tracking suspension pH values during different phases of the dissolution and recrystallization process.

In addition, we also show that aqueous sodium hexametaphosphate (SHMP) treatments add small amounts of phosphate to the surface of calcite and aragonite powders. Specifically, by immersing single-phase powders or mixture powders in either pure water or a water-SHMP solution, we identify differences in dissolution-recrystallization processes, cocomitant with phosphate surface-occlusion. Solid-state NMR (ssNMR) experiments give us detailed and unique information about ^{31}P and ^{13}C and ^{1}H environments that, taken together, allow us to demystify the structure of phosphate incorporated into calcite and aragonite surfaces during dissolution-recrystallization processes.

3.2 Materials and Methods

3.2.1 Precipitation

We synthesized aragonite and calcite powders separately using an aqueous precipitation reaction that is well-documented for phase selectivity [96]. Sodium carbonate (Na_2CO_3) and calcium chloride ($CaCl_2$) salts (Sigma Aldrich) were each mixed with ultrapure water (Barnstead Nanopure, 18.2 MΩ·cm) to make 60 mM solutions (starting pH of 10.9 and 7.2, respectively). The carbonate solution (25 mL) was added dropwise to the chloride solution (25 mL) over a 3 min time span while stirring at 400 rpm, to yield a fine white calcium carbonate precipitate. The key to phase selectivity was temperature: calcite dominates when the precipitation reaction took place at room temperature, whereas aragonite dominated when both reactant solutions were maintained at 90 °C. In all cases, stirring was important to prevent phase heterogeneity in the final product. Final supernatant pH values were 8.5 (room temperature,

calcite) and 8.7 (90 °C, aragonite). The precipitates were separated from the suspension by centrifuge (4000 rpm for 10 min) and filtration, and then dried at ambient temperature for 12 hours. I call these samples "neat powders".

To follow the dissolution and recrystallization more unambiguously by ssNMR, in some syntheses I altered the carbon isotopic compositions of the starting materials by using different combinations of sodium carbonate salts: ^{13}C-Na_2CO_3 (99 atom% ^{13}C, Aldrich) and ^{12}C-Na_2CO_3 (100 atom% ^{12}C, Aldrich). Overall, aragonite was enriched by the stable ^{13}C isotope (20% or 100%), while calcite was used at either 20% ^{13}C enrichment, natural abundance (1.1%), or fully depleted (0%). Thus, only calcite that forms from dissolved aragonite will have a ^{13}C signature.

3.2.2 Aqueous treatments

The goal of our experiments was to investigate calcite-aragonite mixtures in suspension. In most experiments, we did this by making physical mixtures of the two separate polymorphs using different combinations and ratios. The comparisons involved: precipitated aragonite (different isotopic contents) and precipitated calcite (different isotopic contents) or purchased calcite (natural ^{13}C abundance = 1%). In all cases, starting total powder mass was 0.1 g. Table 3.1 summarizes the range of suspensions.

Solids were surface treated by suspension in either ultrapure water (Baenstead Nanopure, 18.2 MΩ·cm) or in sodium hexametaphosphate (SHMP, Alfa Aesar) solutions. Most analyses described in this work focus on samples that were treated with 10 mM SHMP (0.1 g of solid in 10 mL) for up to 1 week in capped glass sample vials. We call these samples "SHMP-treated powders". In control experiments, the same amount of solid was added to 10 mL of nanopure water (Barnstead, 18.2 MΩ·cm). We call these samples "water-treated powders". These suspensions were maintained for long periods of time (days to weeks), without stirring. At regular intervals, aliquots

Table 3.1: Summary of mixed-phase aragonite-calcite suspensions and associated controls, including the source materials and their ratios. Natural abundance is 1% ^{13}C.

aragonite source	calcite source	initial aragonite (%)	initial calcite (%)
precip (natural)	–	100	∼0
precip (100% ^{13}C)	–	100	∼0
–	purchased	0	100
–	precip (100% ^{12}C)	0	100
precip (100% ^{13}C)	purchased (physical mixture)	50	50
precip (100% ^{13}C)	precip (100% ^{12}C) (physical mixture)	50	50
precip (natural)	purchased	90	10
	(physical mixture)	70	30
		50	50

of suspension were extracted and dried so that I could assess any changes in the solid. In some experiments, a pH meter was inserted in the supernatant to record pH at different time intervals.

3.2.3 Characterization

We use attenuated total reflectance Fourier transform infrared (ATR-FTIR) spectra (Bruker Alpha, diamond ATR crystal) to assess phase purity, which is well-suited to distinguishing among different polymorphs. The relative peak intensity changes serve as a qualitative measure of relative proportions in multi-phase samples. Spectra spanned the mid-IR range (400-4000 cm^{-1}, resolution 2 cm^{-1}). We note that ATR-FTIR measurements have a penetration depth ~ 1 μm, which implies that the spectra will include both surface and bulk contributions.

Powders were imaged by FEI MLA 650F scanning electron microscope (SEM) using secondary electron imaging. To obtain high-resolution images, powders were mounted on carbon tape and then gold coated for better electrical conductivity, and

imaged with 20kV accelerating voltage.

To assess elemental composition, SHMP-treated powders were dissolved 1% nitric acid, then analyzed by Perkin-Elmer 5300 DV ICP-OES spectrometer.

Powders were characterized with several different kinds of NMR experiments. To look at ^{13}C and ^{31}P, we used 75.4 MHz ^{13}C and 121.8 MHz ^{31}P ssNMR, respectively. For both C and P, direct excitation experiments as well as cross-polarization experiments were explored. Direct excitation (DE, also known as Chemical Shift Echo (CSE)) is a quantitative measurement, but it can suffer from poor signal:noise for ^{13}C, but not in the case of ^{31}P. The DE spectra were recorded by acquiring 8-32 transients using 2400s repetition delay to assure close to quantitative conditions. Cross polarization (CP) selectively enhances atoms that are close to hydrogen environment. Overall, relaxtation delay of 20s and spinning speed of 10kHz were employed for ssNMR analysis.

Rotational echo double resonance (REDOR) is the ssNMR technique that relies on dipolar coupling, which leads to the quantification of inter-nuclear distance. For our study, the dipolar interaction between ^{13}C and ^{31}P from REDOR sheds light on estimating the distance between phosphate and $CaCO_3$ to outline the mechanism of the surface interaction.

$^{31}P\{^{13}C\}$ and $^{13}C\{^{31}P\}$ REDOR data in this project were collected using the CP and DE excitation techniques. REDOR experiments were carried out with a REDOR pulse sequence with employing 6.4 ms and 12.8 ms recoupling period (64 and 128 rotor-cycles, T_R). From the data acquisition, S_o stands for the reference signal, which has no dipolar recoupling. The dipolar dephased signal S_r is obtained by applying a series of π pulses in the channel.

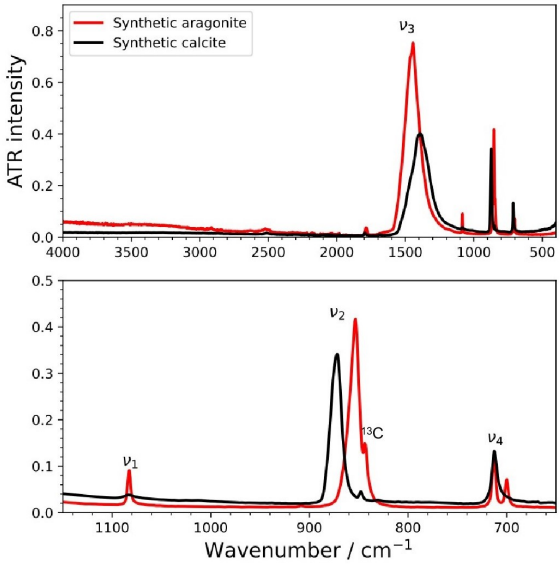

Figure 3.1: Representative ATR-FTIR spectra of neat calcite (black) and neat aragonite (red). There is a small amount of aragonite present in the calcite samples (see the small ν_1 peak near 1090 cm^{-1}). Top: full spectrum. Bottom: Emphasizing the aragonite and calcite ν_1, ν_2 and ν_4 peak.

3.3 Results

3.3.1 ATR-FTIR spectra of starting materials

ATR-FTIR spectra confirm the assignment of calcite and aragonite phases. The neat samples (Figure 3.1) show typical spectra for calcite (black) and aragonite (red). We pay particular attention to the ν_2 peak (Figure 3.1 bottom), which for aragonite (854 cm^{-1}) has a slight lower energy compared to that of calcite (872 cm^{-1}). In addition, aragonite can be uniquely identified by its ν_1 peak (1082 cm^{-1}) that does not have a counterpart in the calcite IR spectrum.

Overall, the ν_2 peaks correspond to the vibrational mode in which the oxygens remain planar while the carbon moves in and out of plane [110]. For ATR-FTIR, the carbonate ν_2 peak (in the 800-900 cm^{-1} range) not only clearly identifies calcite and aragonite, but also provides information about ^{12}C and ^{13}C. Therefore, all ATR

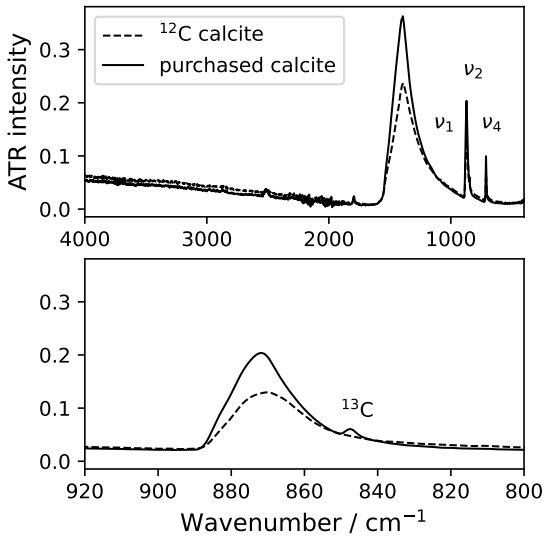

Figure 3.2: Representative ATR-FTIR data for natural abundance calcite and ^{12}C calcite. Top: full spectrum. Bottom: Emphasizing the calcite ν_2 peak (872 cm^{-1}). The small peak near 848 cm^{-1} is the ^{13}C ν_2 peak for calcite due to the 1% natural abundance of that isotope.

spectra in the following sections of this chapter emphasize the ν_2 peak region.

The natural abundance of ^{13}C is 1%, so we compared the synthesized natural abundant calcite and ^{13}C-depleted calcite (nominal 0% ^{13}C). As seen in Figure 3.2, the natural abundance calcite has a small peak at 848 cm^{-1}. This small peak is the ^{13}C ν_2 peak for calcite due to the 1% natural abundance of that isotope. However, the ^{13}C-depleted calcite shows no such ^{13}C peak at 848 cm^{-1}, representing no ^{13}C in the solid.

As seen in Figure 3.3, the natural abundance aragonite has a small ^{13}C peak at 844 cm^{-1}, due to 1% ^{13}C. Besides the different ^{12}C ν_2 peak position, the aragonite and calcite phases can be also distinguished by the different ^{13}C ν_2 peak positions (848 cm^{-1} for ^{13}C calcite and 844 cm^{-1} for ^{13}C aragonite). With the increase of aragonite ^{13}C enrichment, the ^{12}C ν_2 peak begins to weaken, and the ^{13}C ν_2 peak increases, accompanied by a ^{13}C peak shift (Figure 3.3). When aragonite is fully

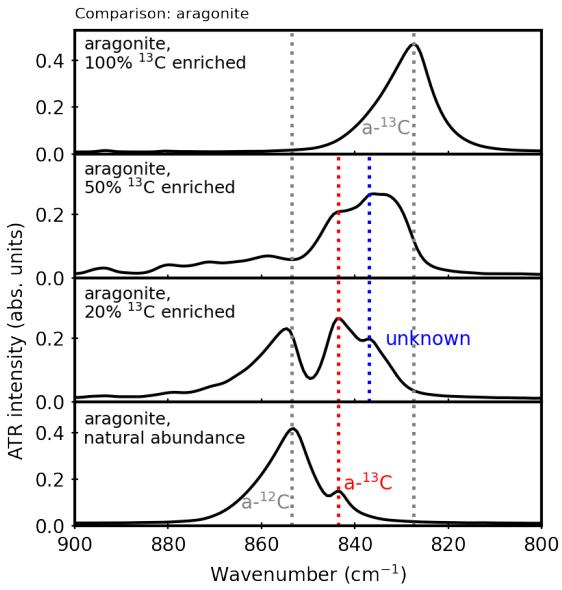

Figure 3.3: ATR-FTIR spectra for isotopically altered aragonite, focusing on the ν_2 carbonate vibrational modes. From bottom to top: (a) natural abundance (1% ^{13}C) aragonite, (b): 20% C ^{13}C enriched aragonite, (c): 50% C ^{13}C enriched aragonite, (d) fully enriched (100% ^{13}C) aragonite. Vertical dashed lines serve as a guide to represent where the aragonite ^{12}C or ^{13}C peak would be located.

enriched ^{13}C (100%), there is only one peak (Figure 3.3). The ^{13}C peak shift remains a mystery, and are beyond the scope of this thesis.

3.3.2 Single polymorph experiments

As control experiments, we first followed the dissolution behaviour of aragonite-only and calcite-only suspensions, either with or without stirring, for periods of at least one week. We did not attempt to measure the amount of undissolved solid; instead, we used SEM and ATR-FTIR, to track evidence of increased amounts of calcite, which occur after aragonite dissolution.

Scanning electron micrographs of neat powders (Figure 3.4) show typical crystal morphologies for each polymorph. Neat aragonite shows acicular or columnar crystal habits (Figure 3.4A), while calcite shows larger blocky crystallites (Figure 3.4D). Both

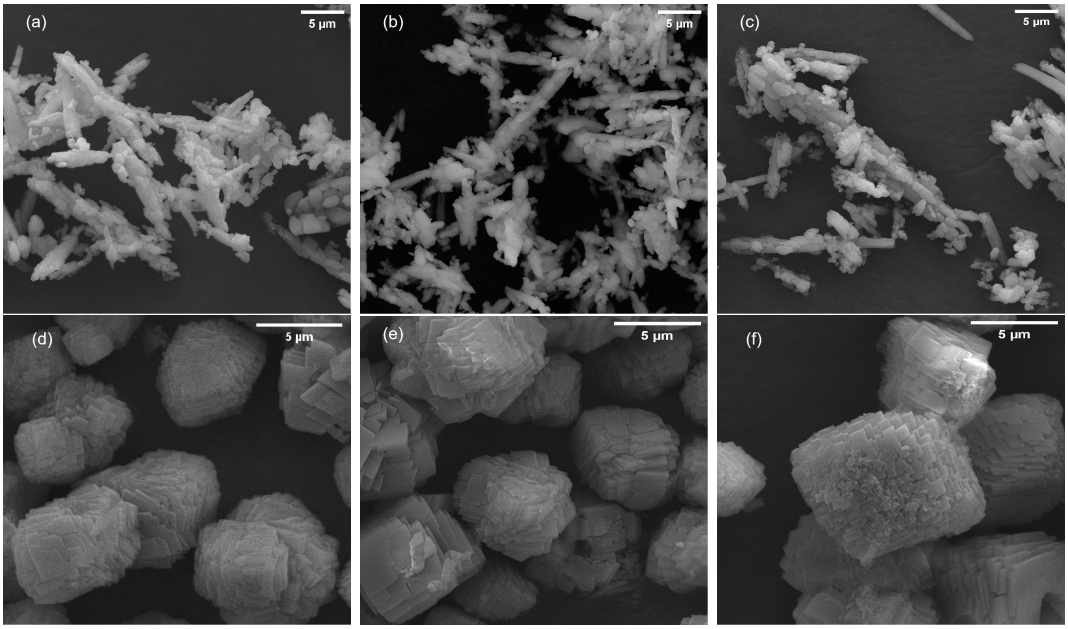

Figure 3.4: Representative SEM images of aragonite (top row) and calcite (bottow row). A: neat aragonite. B: water-treated aragonite (1 week). C: SHMP-treated aragonite (10 mM, 1 week). D: neat calcite. E: water-treated calcite (1 week). F: SHMP-treated calcite (10 mM, 1 week).

aragonite and calcite crystallites show imperfect crystal shapes with evidence of many different nucleation sites.

ATR-FTIR data for the water-treated, unstirred aragonite show no evidence of phase conversion to calcite (Figure 3.5a), with aragonite remaining the dominant phase even after one week of water suspension. From SEM images, these samples maintained similar needle-like crystal habits like its neat precursor (Figure 3.4B). To exclude the effect of solution saturation, precipitated aragonite was exposed to an unstirred saturated $CaCO_3$ solution. The saturated solution was prepared by adding calcite in water for two weeks. The supernatant was then taken to a new sample vial, and aragonite was added. The ATR-FTIR spectra of these water-treated aragonite powders still show no evidence of calcite recrystallization, even after one month of immersion (Figure 3.5c). However, stirring caused a small calcite IR shoulder to

appear at the ν_2 position (Figure 3.5b), suggesting that some aragonite dissolved and recrystallized as calcite. Based on repetitions of this stirring experiment, we observed small variations in the relative aragonite and calcite ν_2 peak intensities (Figure 3.5d).

For water-treated calcite, ATR-FTIR spectra on dried aliquots (Figure 3.6) showed that calcite remained the dominant phase after suspension in water. However, the small amount of secondary-phase aragonite decreased the longer that the solid was in suspension. We monitored this change by tracking the decreasing relative intensity of the aragonite ν_1 peak. The SEM images do not show an appreciable change in the calcite crystallite habits or sizes after 1 week of water immersion (Figure 3.4E).

As further evidence of aragonite dissolution and calcite reprecipitation, we used ^{13}C solid-state NMR to compare the as-precipitated aragonite powders with those suspended in water for one week (either stirred (AWS) or unstirred (AWNS)). In Figure 3.7, all samples exhibit the characteristic aragonite peak (170.7 ppm) in their ^{13}C DE spectra as the major component. While the control sample shows primarily aragonite, the DE spectrum of the AWNS and AWS samples shows calcite peaks (168.4 ppm) that indicate 7% and 16% aragonite-to-calcite conversion, respectively.

All samples also exhibit pronounced CP signal, which suggests more complex content including contributions from disordered aragonite (DA, 170.1 ppm). Since aragonite is largely preserved after the water treatments, we speculate that the disordered phase spread throughout the bulk. In contrast, if the disordered phase is restricted to exposed surfaces, then we might expect a larger phase conversion percentage. Based on the deconvolution of the DE spectral peaks (Table 3.2), the distribution of crystalline aragonite phase in AWNS or AWS is 70% and 66%, respectively. This is smaller than that of the as-prepared aragonite (75%). This suggests that there is dissolution when the aqueous suspension is unstirred, and even more dissolution while stirring. The stirred product contains the least amount of DA phase (18%) and the most calcite

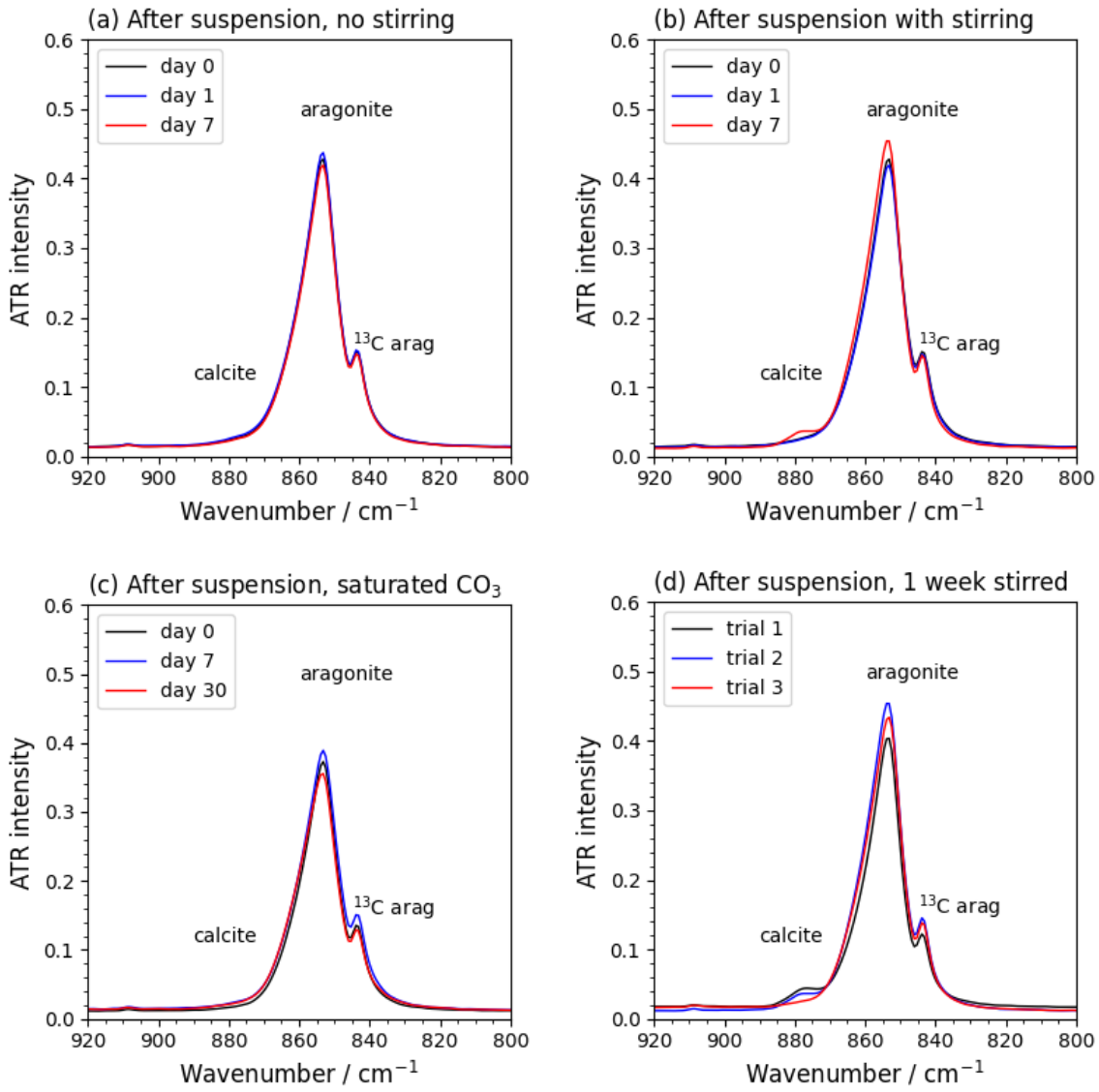

Figure 3.5: Representative ATR-FTIR spectra. (a) Aragonite ν_2 peak after suspension in water, unstirred. (b) Aragonite ν_2 peak after suspension in water while stirring; the weak shoulder at 872 cm^{-1} is calcite ν_2. (c) Aragonite ν_2 peak after suspension in a saturated solution with respect to aragonite. (d) Repeated stirring experiments show the persistence of a dominant aragonite ν_2 peak and slight variations in the intensity of the calcite ν_2 shoulder.

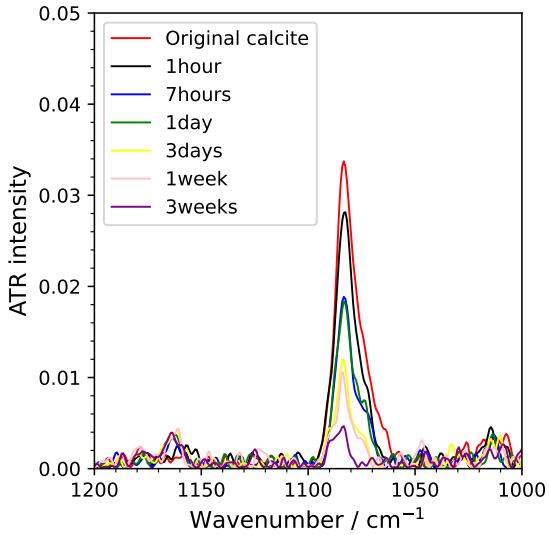

Figure 3.6: Representative ATR-FTIR spectra. (a) Water-treated calcite, highlighting the change in the secondary-phase aragonite's ν_1 peak after exposure to water for up to three weeks. All spectra were normalized to the calcite ν_2 peak (not shown) to emphasize that the aragonite ν_1 peak decreases in relative intensity the longer the suspension sits.

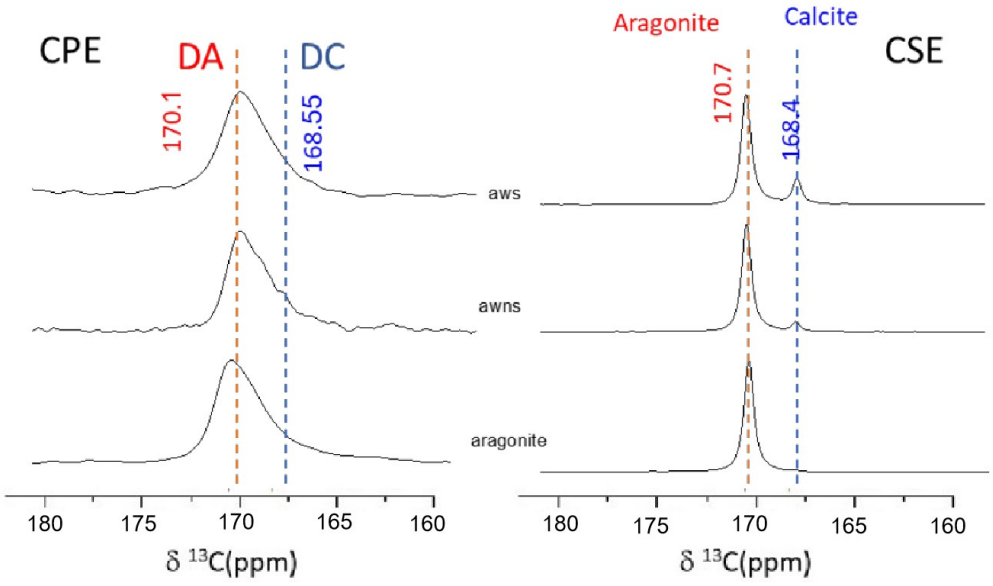

Figure 3.7: ^{13}C DE(CSE), CP ssNMR spectra of control aragonite, one-week non-stirring water-treated aragonite (AWNS) and one-week stirring water-treated aragonite (AWS). CP (left) and DE (right). DA and DC represent disordered aragonite and disordered calcite, respectively. The horizontal axis is ^{13}C chemical shift (ppm).

Table 3.2: Distribution of species in samples obtained by deconvolution of the ^{13}C DE spectra and NMR parameters.

Sample	Aragonite phase	Calcite phase	DA phase
Control aragonite	75	0	25
AWNS	70	7	23
AWS	66	16	18

(16%), indicating the most recrystallization.

Taking these ATR-FTIR, SEM, and ssNMR data together, we conclude that:

- Whenever the aragonite powder is suspended in water, there is some dissolution and recrystallization as calcite. Small amounts of phase conversion may be undetectable by ATR-FTIR, but ssNMR provides clear evidence.

- Stirring triggers more dissolution and recrystallization than for an unstirred suspension monitored for the same one-week time period. This is not surprising, given that stirring will increase the diffusion rates of calcium and carbonate ions in solution.

- The amount of calcite recrystallization over the span of one week fluctuates somewhat with repeated experiments under nominally the same conditions. This emphasizes that slow kinetics affect the dissolution and recrystallization processes.

3.3.3 Mixed polymorph experiments

Interesting results occur when we move to a two-component system: a mixture of calcite and aragonite powders that are suspended in water. The presence of calcite in the initial mixture boosts the speed of the aragonite dissolution and subsequent calcite precipitation so that it is noticeable during a 1 week immersion experiment.

To demonstrate unambiguously that the dissolution of aragonite is followed by recrystallization of calcite, we used isotopes as tracers to follow phase composition changes over time. To follow the phase composition over time, we used both ATR-FTIR and ssNMR, since each is sensitive to carbon isotopes in different and complementary ways.

The natural abundance of ^{13}C is 1%, so we synthesized highly ^{13}C-enriched aragonite (nominal 100% ^{13}C) and highly ^{13}C-depleted calcite (nominal 0% ^{13}C) to pair together in an aqueous suspension. By using highly-^{13}C-depleted calcite as a starting material, there will be no NMR-detectable calcite signature because ^{12}C is not NMR-active. Using the ^{13}C-depleted calcite in combination with highly-^{13}C-enriched aragonite, this ensures that all signal in ssNMR spectra, including that of any calcite, must come from carbon that originated from the ^{13}C-aragonite. As mentioned above, ATR-FTIR can detect relative changes of both isotopes in each calcium carbonate phase (See Figure 3.2 and Figure 3.3). In other words, by using isotopic labelling with these two isotope-sensitive material characterization methods, it is certain that if any ^{13}C calcite is detected, the calcite phase must have recrystallized from the dissolved aragonite.

To illustrate the results of this experiment, Figure 3.8 shows data for a 1:1 aragonite-calcite mixture before and after one week of immersion in water. The mixture exhibits a dominant characteristic aragonite peak in both the ATR-FTIR spectrum (Figure 3.8a) and the ^{13}C DE MAS spectrum (Figure 3.8b). There is also a small characteristic peak for calcite in ssNMR, and the peak quantification to show that calcite is a minor component with 2% abundance. Following one week of water-treatment, both the ATR-FTIR and ssNMR data show ^{13}C calcite. Quantification from the ssNMR data shows a 59% increase in calcite phase, which is 15 times more calcite than what forms from an aragonite-only suspension over the same 1 week pe-

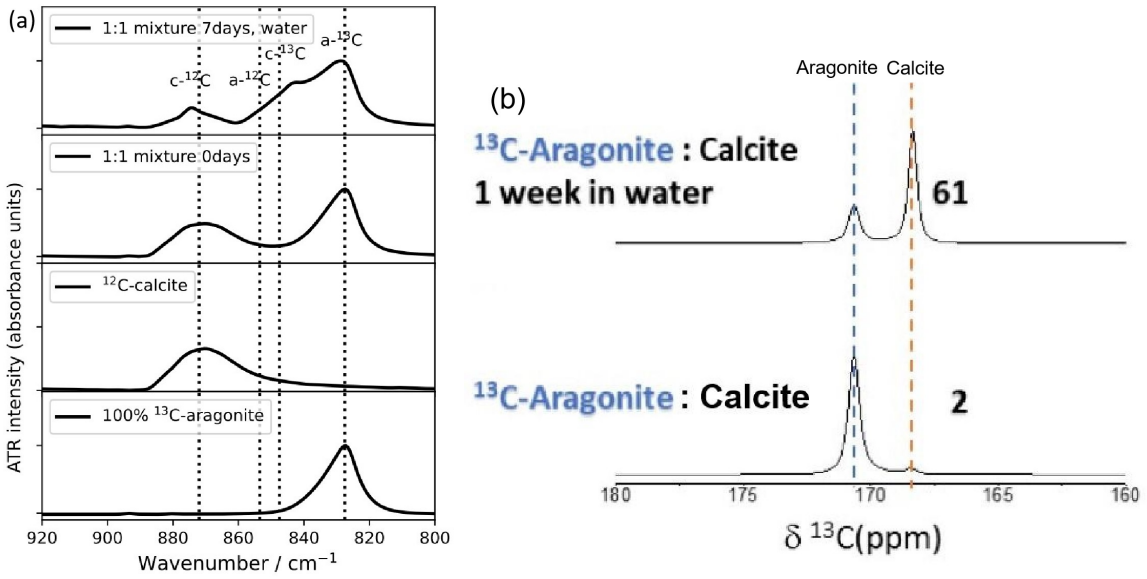

Figure 3.8: Representative ATR-FTIR spectra (a) and ^{13}C DE ssNMR spectra (b) of a 1:1 ^{12}C calcite-^{13}C aragonite mixture before and after 1 week of water immersion. For clarity, the ATR-FTIR data focuses on the carbonate ν_2 peak region. The IR plots from bottom to top represent: 100% ^{13}C aragonite, ^{12}C calcite, mixture and mixture after 1 week water treatment. Dashed vertical lines indicate calcite ^{12}C ν_2 (872 cm^{-1}) , aragonite ^{12}C ν_2 (854 cm^{-1}), calcite ^{13}C (848 cm^{-1}) ν_2 and aragonite ^{13}C ν_2 peak (828 cm^{-1}). For ssNMR, the plot on the top is 100% ^{13}C aragonite, and the bottom plot indicates 100% ^{13}C aragonite, ^{12}C calcite mixture after 1 week water treatment.

riod. These results clearly demonstrate enhanced aragonite phase conversion in the presence of suspended calcite particles, and it also demonstrates that the dissolved aragonite recrystallizes as calcite.

To demonstrate the time-evolution of the dissolution recrystallization process, we show representative ATR-FTIR, DE ssNMR, and CP ssNMR data in Figure 3.9. In this case, we used a starting mixture that was the same aragonite:calcite ratio as described above (1:1), but with natural-abundance (1% ^{13}C) calcite (purchased) with the same highly-^{13}C-enriched aragonite (100%). The time series follows phase changes between 1 hour and 1 week of immersion. The ATR-FTIR data (Figure 3.9a) show an increased ^{13}C calcite ν_2 peak as a function of time. The ssNMR data are consistent

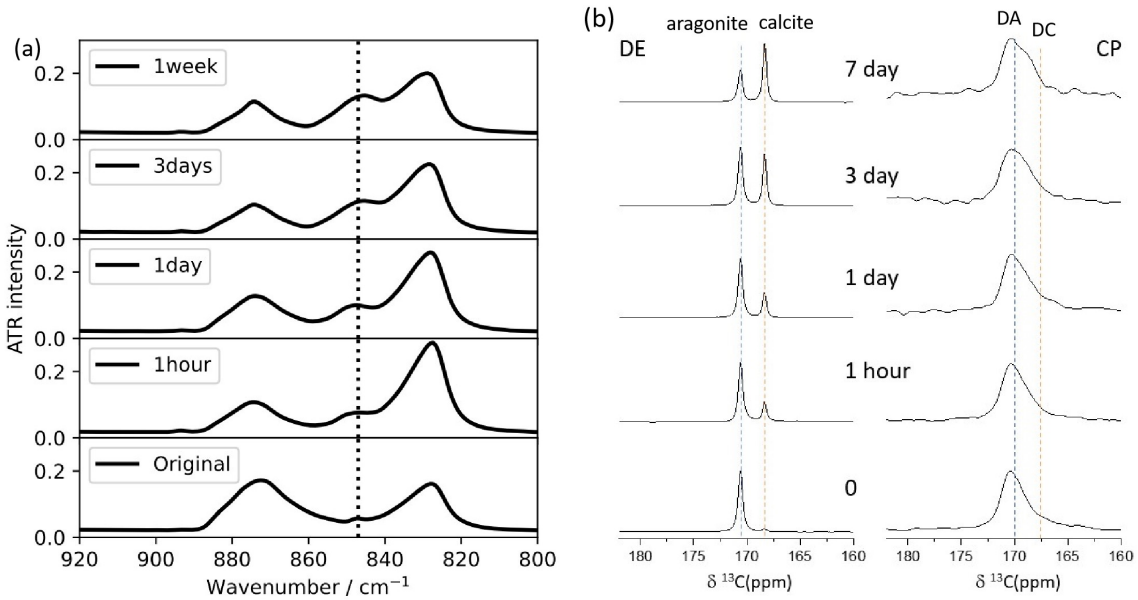

Figure 3.9: Representative ATR-FTIR spectra (a) and ^{13}C DE, CP ssNMR spectra (b) for 1:1 aragonite-calcite powders as function of suspension time in water. The isotopic content of aragonite was highly-enriched (100% ^{13}C) while the calcite had natural abundance (1% ^{13}C). The dotted line in (a) corresponds to the ^{13}C calcite peak (848 cm^{-1}). In CP ssNMR spectra, DA and DC represent disordered aragonite and disordered calcite, respectively.

with the ATR-FTIR trends, but also provide additional insights. The broad (partially resolved) peaks in the CP spectrum (Figure 3.9b) represent the population of disordered carbonates of disordered aragonite (DA) and disordered calcite (DC) that are in the vicinity of residual water molecules. Sampling the mixture compositions after different suspension times shows that the calcite-to-aragonite ratio increases, until eventually after 7 days (the longest suspension time), calcite becomes the dominant component (calcite:aragonite 60:40). A similar trend is shown by the disordered carbonates, where the fraction of DC grows relative to DA for longer suspension times.

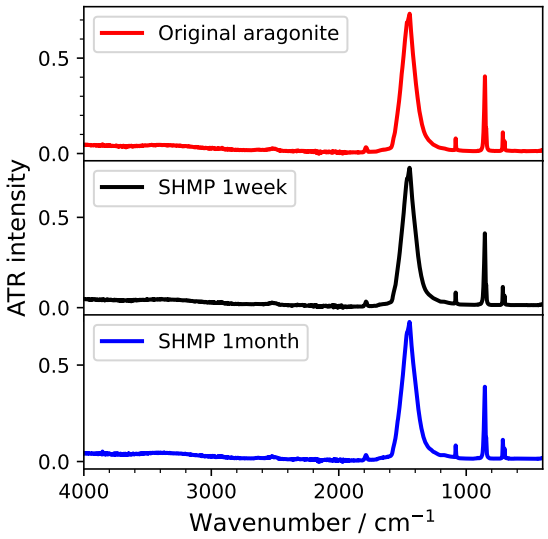

Figure 3.10: Representative ATR-FTIR spectra of neat aragonite and SHMP-treated aragonite, indicating no phosphate secondary phases even after one month of SHMP treatment.

3.3.4 Phosphate treatment experiments

We monitored SHMP-treated calcite and aragonite suspensions for periods of up to three weeks. Spectra of dried aliquots showed that the SHMP-treated calcite and SHMP-treated aragonite had FTIR spectra (Figure 3.10) that showed little or no evidence of phosphate secondary phases, even up to three weeks of immersion in the highest concentration (10 mM) of SHMP solution we tried. It is worth mentioning that the concentration of SHMP used in industry to control calcium carbonate scaling is only in the mg/L range [23, 118], which is much smaller than the concentration of SHMP (10 mM) used in this study. The crystal morphology of SHMP treated aragonite and calcite (Figure 3.4c,f) does not change much. It is still like the crystal habit of as-precipitated aragonite and calcite.

Elemental analyses from ICP-OES confirm the existence of low P content in SHMP-treated samples, with mass fractions that are $\sim$ 500 times less than for Ca (Table 3.3). I note that there is also a tiny amount of Mg, as well as a large amount

Table 3.3: Mass fractions from ICP-OES for SHMP-treated calcite and aragonite, after one week treatment (0.1 g solid in 10 mL of 10 mM solution).

sample type	P:Ca (mol %)	Ca (mg/g)	P (mg/g)	Mg (mg/g)	Na (mg/g)
aragonite-SHMP	0.30	369	0.90	0.031	6.73
calcite-SHMP	0.23	377	0.66	0.029	6.61

of Na (either excess SHMP or residual NaCl byproduct from the initial synthesis).

The $CaCO_3$ phase conversion in SHMP and water treatments show different behaviors in the mixed polymorph system. Based on ssNMR spectra (Figure 3.11), after one week of water immersion, the aragonite phase in the mixture decreased to 35%, while calcite phase increased to 61%, attesting for notable aragonite dissolution and calcite crystallization. After one week of SHMP treatment, a small reduction of both the aragonite and calcite components is observed (84 and 4%), without seeing the dramatic formation of the calcite phase (Figure 3.11). The behavior of mixed powders in SHMP solution indicates that phosphate protects aragonite from transformation to calcite in solution.

To understand more about where the P is incorporated, we relied on ^{31}P solid state NMR characterization, which clearly identifies the presence of the P-bearing species of SHMP. Both direct excitation (DE) and cross-polarization (CP) MAS spectra show notable P-content in the solids (Figure 3.12a). In general, peaks in the CP spectra imply that there are different sub-populations of P species weighted by proximity to hydrogen, such as water molecules, H-bearing P-species, and/or bicarbonates. In this case, the ^{31}P DE and CP MAS spectra expose three broad peaks (centered at 4, -5, -20 ppm) of orthophosphate (labelled Pi), pyro- and/or terminal polyphosphate, and internal P of polyphosphate, respectively. These species represent the speciation of hydrolysis products of SHMP.

The ^{31}P$\{^{13}$C$\}$ CP-REDOR spectra (Figure 3.12b) show notable REDOR attenu-

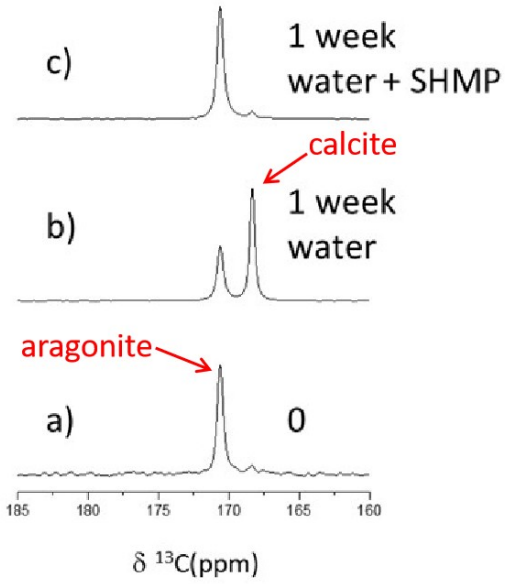

Figure 3.11: ^{13}C DE ssNMR spectra of (a) a 1:1 mixture of 20% ^{13}C-aragonite and natural abundance (n.a., 1.1% ^{13}C) calcite, (b) the mixture after suspension in water for one week, (c) mixture after one week suspension in 10 mM aqueous solution of SHMP.

ation. The relative peak attenuation is represented by $\delta S/S_0$. At the longest dipolar recoupling time, 12.8 msec, it reaches 25% for the Pi and pyro/terminal components, whereas at half recoupling time, 6.4 msec, the Pi peak attenuation is halved, ∼12%, and that of pyro/terminal further reduced to 8%. Accounting for the 20%-13C enrichment level, the implication of the extent of the REDOR effect is that all phosphorous are within 1 nm distance from at least two carbonate ions (Ca^{2+}-mediated interaction). Charge-wise, these close proximities between the two negatively charged anions (PO_4^{3-} and CO_3^{2-}) must represent interactions that are mediated by positively charged Ca^{2+} cations. This result rules out the occurrence of a phosphate-rich phase (P-aggregates) and is consistent with molecularly dispersed P-species which are surface intercalation species.

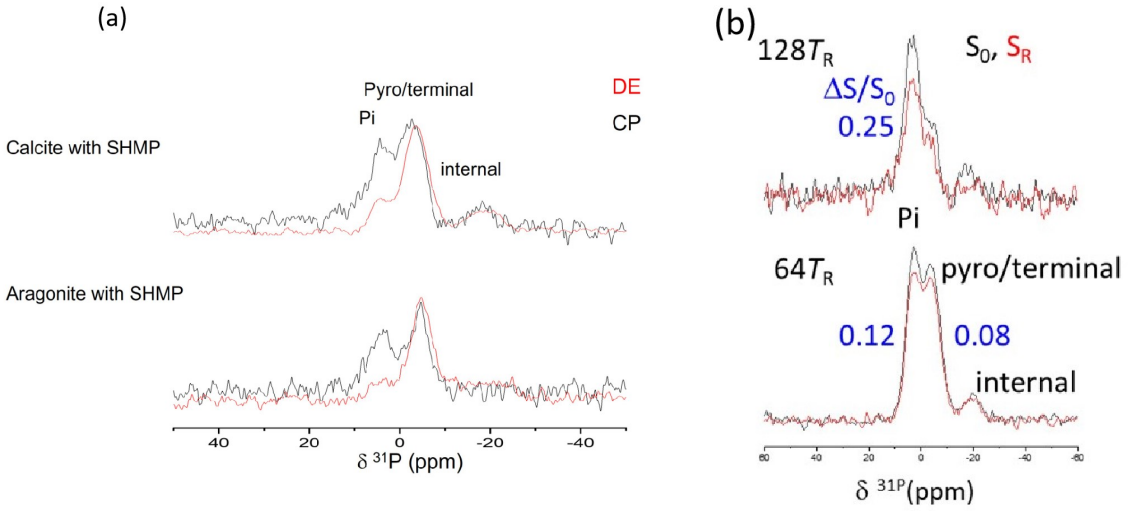

Figure 3.12: ssNMR of (a): ^{31}P ssNMR DE (CSE) (red) and CP (black) spectra of SHMP treated particles with three different P-species labelled at 4, -5 and -20 ppm. (b): representative ^{31}P{^{13}C} CP-REDOR. S_0 – reference (black), S_R (red) after 64 (bottom) and 128 (top) recoupling cycles (6.4, 12.8 ms periods) for 1:1 mixture of [20%-^{13}C]aragonite and natural abundance calcite after suspension aqueous SHMP solution for one week.

3.4 Discussion

3.4.1 Aragonite conversion in the presence of calcite

Our data show that lab-synthesized neat aragonite indeed undergoes dissolution-recrystallization in solution. However, such phase conversion is so slow and small that bulk characterization, such as IR, is not capable of detecting the phase transformation. However, by mixing of calcite and aragonite powders in water, an evident aragonite to calcite phase conversion is observed.

To better understand the role of calcite for the aragonite dissolution and recrystallization, we made a physical mixture of neat aragonite and neat calcite, with various mass ratios (aragonite: calcite 0.9:0.1, 0.7:0.3 and 0.5:0.5). 0.1 g of each starting material was added to 10 mL water, and then sonication was done to ensure a uniform

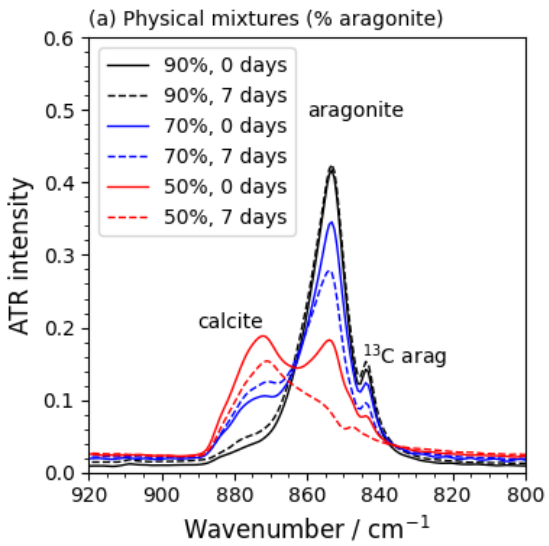

Figure 3.13: Representative ATR-FTIR spectra, emphasizing aragonite ν_2 and calcite ν_2 peaks. Physical mixtures (90%, 70% and 50% aragonite, respectively) before and after one week of suspension in water.

mixture in the suspension. At specific time intervals, 1 mL suspension was withdrawn and centrifuged. Although FTIR peak intensity ratios do not provide rigorous quantitative information about the recrystallization rate, we found that samples that start with a larger fraction of calcite undergo more aragonite dissolution for the same amount of immersion time. ATR-FTIR spectra (Figure 3.13) indicate that the 90%-aragonite mixture does not show considerable calcite recrystallization over a one-week period. However, over the same length of time, the 70%-aragonite and 50%-aragonite mixtures show a successively larger reduction in the aragonite ν_2 peak, with the near total disappearance of the aragonite phase in the 50%-aragonite mixture.

For a single calcium carbonate phase (either calcite or aragonite), it is typically appropriate to assume that equilibrium conditions prevail. For example, we can consider that the solubility product (K_{sp}) is an equilibrium constant that only varies with temperature. At ambient environment, calcite ($pK_{sp} = 8.48$) is slightly less soluble than aragonite ($pK_{sp} = 8.34$). Using the pK_{sp} values for each polymorph, a straight-

forward analysis give an interesting result that matches our experimental findings. If a single polymorph is immersed in water, less than 1% of the total mass in our experiments would be dissolved in solution in order to reach saturation conditions. For example, in 10 mL of water, 100 mg of aragonite would dissolve 0.0675 mg to reach equilibrium, while 100 mg of calcite would dissolve 0.0575 mg to reach its equilibrium. Thus, either phase persists because the large amount of solids are present in solution.

However, a different result unfolds when calcite and aragonite are mixed together in the suspension. We saw enhanced aragonite-to-calcite phase conversion. Since conversion in the absence of the co-suspended calcite particles does not advance beyond a few mol%, it indicates these particles serve as nuclei which induce crystallization and promote overgrowth on their exposed surfaces. By removing free (dissolved) calcium carbonates, they incite continued dissolution of aragonite. We view this situation as a thermodynamic "pump". As a higher percentage of calcite particles are mixed in the suspension, more ion attachment sites will cause higher rate and extent of conversion (See ATR result from Figure 3.13). This observation implies the more calcite surface area would enhance the conversion rate from aragonite to calcite.

This line of reasoning helps to explain why our neat aragonite samples show very slow rates of conversion to calcite. As aragonite reaches its saturation state in suspension, the solution is supersaturated with respect to calcite phase. Thus, we would expect calcite precipitation to counteract the supersaturation condition. However, the ssNMR shows only 2 to 4% growth of the calcite content as neat aragonite immersed in water (Figure 3.5 and Figure 3.7). We expect that calcite growth should begin with cluster formation to crystalline particles. The remaining aragonite solid fails to serve as sites for direct ion attachment of calcite. Therefore, the cluster nucleation (energy penalty) makes this process rate-limiting and time consuming. Such kinetic effects could be slightly promoted by stirring: the fast diffusion of Ca and CO_3 ions favours

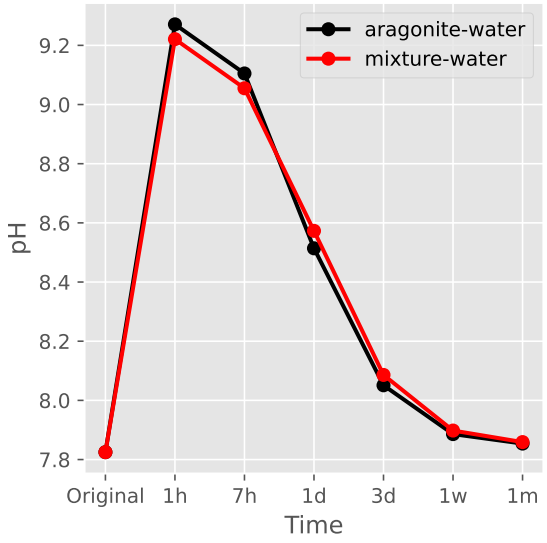

Figure 3.14: Representative pH vs time trends for suspensions of neat aragonite and 1:1 aragonite/calcite physical mixture. The first data point in each curve (labelled “original") corresponds to the pH of the initial solution (water) before any solid is added.

the cluster nucleation, accelerating crystal growth (for our stirring experiments 16% growth of the calcite after one week) (Figure 3.5 and Figure 3.7).

We note an interesting point, that neat-aragonite and the physical mixture show very different dissolution recrystallization rates but yet the pH vs time trends are quantitatively similar. The neat aragonite has a small amount of calcite in it (2%), so we expect the aragonite-to-calcite pump process to occur in both suspensions, but at a signficantly faster rate in the 1:1 mixture. This could suggest that the pH vs time trends do not depend on the rate of dissolution-recrystallization, but rather reflects the stage of the non-equilibrium process. The rapid pH rise in the first hour corresponds to rapid dissolution due to the undersaturation conditions in the solution, while the slow pH decline back to near starting represents the stage during which the recrystallization of calcite is rate-limited by the rate of the aragonite dissolution.

3.4.2 Phosphate-calcium carbonate interaction

We see two possible explanations for SHMP protection: SHMP stabilizes the aragonite surfaces against dissolution, or/and SHMP stabilizes calcite surfaces and reduces their affinity and action as nucleation agents that enhance overgrowth. We propose that both explanations play a role in our experiments, but at different stages of the immersion process.

First, the ssNMR data suggest that SHMP does not prevent disordered regions from forming (Table 3.4). After 1 week of immersion, the mixture in water shows 4% disordered aragonite (DA), which slightly less than the DA percentage in original mixture (6%). This make sense if we assume that disordered carbonate is more likely to dissolve and contribute to new calcite (61% growth after 1 week). However, for the same kind of mixture in SHMP, the DA phase increased from 6% to 12%. To look more critically at this possibility, we compared the DA growth of neat-aragonite in both water and SHMP suspensions. Based on the DE spetra peak deconvolution (Table 3.5), both water and SHMP immersion (1 week) show a DA increase of 8-18% when compared to the DA of original neat-aragonite. If we assume that the disordered phase is a direct result of dissolution, then our results suggest that SHMP did not prevent the dissolution.

Even though the SHMP may not prevent all dissolution, it clearly slows very dramatically the aragonite-calcite thermodynamic pump. In Table 3.4, there was no increase in the calcite phase of the mixture powders after 1 week of immersion in SHMP, whereas there was a 61% increase after one week in water. To explain this, we look in more detail at where the phosphate species reside.

From $^{13}C\{^{31}P\}$ DE- and CP-REDOR (Figure 3.15), we could tell that SHMP treated calcite and aragonite both show small-to-vanishing REDOR effect, confirming that the carbonates close-by to P-species are only a minute fraction of the bulk and

Table 3.4: DE spectra peak deconvolution, for 1:1 physical mixture (100%-^{13}C) aragonite and natural abundance calcite (1%-^{13}C), before and after immersion treatments in either water or SHMP solution.

Sample	Aragonite	Calcite	Disordered aragonite (DA)
Aragonite/calcite mixture starting powders	87%	6%	6%
Aragonite/calcite mixture one-week water	35%	61%	4%
Aragonite/calcite mixture one-week SHMP	84%	4%	12%

the surface. This is consistent with the occlusion/adsorption of P-species only at the surface.

The interpretation of the NMR data results is also supported by pH *vs.* time trends, shown in Figure 3.16. Both the SHMP and water treatment shows rapid pH change at first one-hour period, suggesting the dissolution at the early stage. The subsequent pH decrease, however, indicates different results between water and SHMP treatments, where the particles in SHMP experience slower pH decline compared to water. Since such a pH decrease has been attributed to the consumption of free carbonate or bicarbonate for cluster nucleation (recrystallization), the slower pH decline in SHMP suggests the recrystallization has retarded due to the phosphate adsorption on the particle surface.

Table 3.5: DE spectra peak deconvolution, for 20% ^{13}C enriched aragonite, before and after immersion treatments in either water or SHMP solution.

Sample	Aragonite	Calcite	Disordered aragonite (DA)
Aragonite starting powders	87%	1%	12%
Aragonite one-week water	77%	2%	20%
Aragonite one-week SHMP	69%	5%	29%
Aragonite one-week SHMP trial2	77%	2%	21%

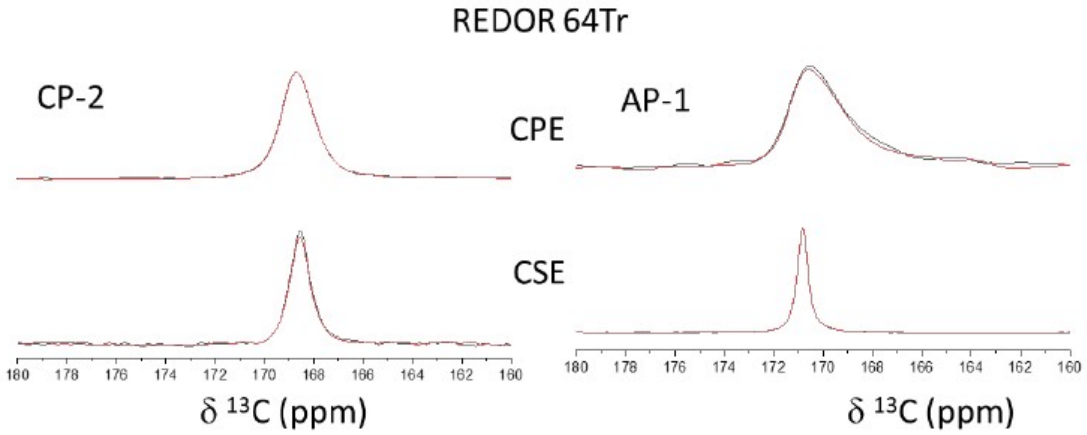

Figure 3.15: $^{13}C\{^{31}P\}$ DE(CSE)- and CP-REDOR spectra. Left plots: SHMP treated [20%-^{13}C]calcite. Right plots: SHMP treated [20%-^{13}C]aragonite. The reference (S_0, black) and REDOR-attenuated (S_R, red) spectra are overlaid. The representative spectra were obtained with 6.4 ms recoupling period (64 T_R).

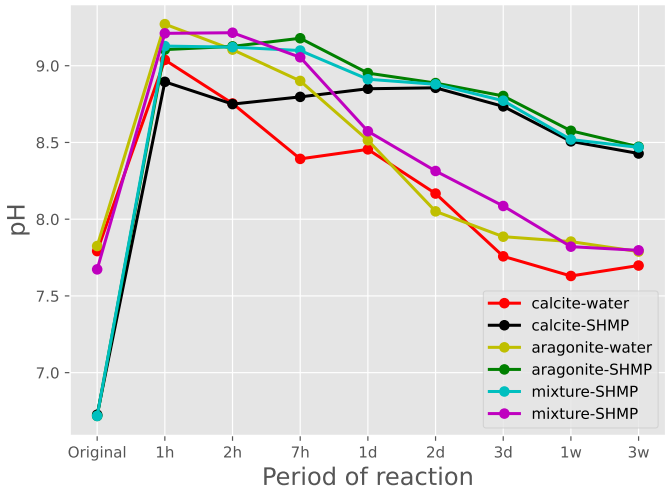

Figure 3.16: Representative pH *vs.* time trends for suspensions of neat aragonite, neat calcite and 1:1 aragonite/calcite physical mixture. The first data point in each curve (labelled "original") corresponds to the pH of the initial solution (water or SHMP) before any solid is added.

3.5 Conclusion

when the neat particles are immersed in water, very limited dissolution and recrystallization is observed. However, as aragonite and calcite solids are mixed together, the mixed particles in the water cause continuous aragonite dissolution (non-equilibrium), speeding up the aragonite-to-calcite conversion.

However, with the addition of phosphate species, the aragonite-to-calcite conversion in the mixture suspension is largely retarded. The phosphate species is dispersively adsorbed on the surface of $CaCO_3$ particle, without forming any separate phosphate-rich phase. However, the surface-embedded phosphate entities stabilize aragonite solids against dissolution- recrystallization (and polymorph conversion) in an aqueous environment. SHMP fails to prevent $CaCO_3$ dissolution within the first hour, but phosphate adsorption prevents Ca^{2+} and CO_3^{2-} ions from recrystallization.

Chapter 4

Comparing polyphosphate and orthophosphate treatments of solution-precipitated aragonite powders

This chapter is being published as Boyang Gao and Kristin M. Poduska "Comparing polyphosphate and orthophosphate treatments of solution-precipitated aragonite powders" *Solids*. Accepted date: November 18^{th} 2022. doi.org/10.3390/solids1010000. The content of this chapter is same as the accepted article, but the formatting has been changed to fit the thesis format.

We chose to submit it to this journal because it is an open-access journal that is easy for chemists and engineers to read and because this particular work may apply to

industrial use. Boyang Gao carried out the experiments, data analysis and contributed to the writing of the manuscript. Dr. Kristin M. Poduska provided guidance over the experimental design, data analysis, and the writing of the manuscript.

4.1 Abstract

The aqueous and thermal stabilities of aragonite ($CaCO_3$) powders against phase conversion are important for industrial applications that rely on calcium carbonate. We describe the synthesis and characterization of solution-precipitated aragonite powders before and after exposure to different aqueous polyphosphate (SHMP) or orthophosphate (PO_4) treatments with concentrations in the range of 1-10 mM ($\sim$1 g/L). Based on infrared spectra, differential scanning calorimetry, and thermogravimetric analyses, results show that orthophosphate treatments lead to secondary phase formation and complex thermal annealing behaviors. In contrast, polyphosphate treatments help to prevent against aragonite dissolution during exposure to water, and they also provide a slight increase in the thermal stability of aragonite with regard to conversion to calcite.

4.2 Introduction

The aqueous and thermal stabilities of aragonite ($CaCO_3$) powders against secondary phase formation are important for industrial applications that rely on calcium carbonate [95]. Surface treatments on calcium carbonate powders – whether aragonite or calcite – are common to prevent particle aggregation [119]. $CaCO_3$ precipitation and scaling are formidable concerns in industrial processes, especially those that involve pipelines; unwanted deposits can reduce heat transfer efficiency or accelerate corrosion, both of which have detrimental economic impacts [120, 121].

Polyphosphate, in the form of the hexamer sodium hexametaphosphate (SHMP), is widely used to disperse calcium carbonate particles in industrial applications, and has also been used in laboratory sample preparations [122] and surface-charge measurements [20]. Even though SHMP is widely used, it is still the subject of active study, with recent work highlighting its efficiency in inhibiting $CaCO_3$ scaling [53,123]. Other work reports that SHMP mixed with liquid cement can accelerate the healing of concrete cracks by promoting anisotropic high-aspect-ratio aragonite crystal formation that are more effective in sealing cracks than the more blocky, isotropic calcite crystals [124]. Despite the widespread use of SHMP, its surface-specific interactions with calcium carbonate are poorly studied.

Orthophosphate salts, containing single phosphate units, are also widely used and studied for their interactions with calcium carbonate. For example, aragonite cement has been investigated as an interfacial material to accelerate bone tissue replacement and repair, due to its higher solubility relative to calcite and calcium phosphates such as hydroxyapatite (HAp) [125,126]. In other instances, orthophosphate in waste water has been studied for its interactions with aragonite, as a way to remove waterborne phosphate contaminants [127].

In this work, we compare the effect of aqueous polyphosphate and orthophophate treatments – with similar phosphate concentrations – on solution-precipitated aragonite powders, including subsequent annealing treatments, while focusing on which conditions trigger secondary phase formation.

4.3 Materials and Methods

4.3.1 Precipitation

A solution-based precipitation reaction [96] used stirring and temperature control to minimize phase heterogeneity in the final product. Starting solutions were both held at 90°C: 60 mM Na_2CO_3 (ACS reagent grade (Sigma Aldrich) salt in ultrapure water (18.2 MΩ·cm), 25 mL with starting pH 10.9) and 60 mM $CaCl_2$ (ACS reagent grade (Sigma Aldrich), 25 mL with starting pH 7.2), drop by drop over a 3 min time span while stirring at 400 rpm, to yield a white precipitate. The suspension cooled to room temperature, and was then centrifuged (4000 rpm for 10 min) and filtered to yield a supernatant (pH 8.7) and white solids, which were dried at ambient temperature for 12 hours.

4.3.2 Annealing

In some experiments, the as-precipitated (untreated) powders were annealed in a pre-heated 400°C furnace for 20 min.

4.3.3 Aqueous treatments

After precipitation, some powders were treated in solutions with either polyphosphate or orthophosphate solutions. Since pH is one of the key factors that determines phosphate speciation in solution [128], treatments used different starting pH values (ranging from 6.5 to 10.5) and different phosphate concentrations (1-10 mM).

For polyphosphate treatments, we used $Na_6[(PO_3)_6]$ (sodium hexametaphosphate, (SHMP), ACS reagent grade, Alfa Aesar) solutions at 1, 5, or 10 mM concentrations, with an initial pH value of 6.8. For some treatments, the pH was adjusted to 7.0 or 10.5 with NaOH (ACS reagent grade).

For orthophosphate treatments, we used standard phosphate buffer salts, but at concentrations and initial pH values that are similar to the SHMP treatments described above. The near-neutral solutions used K_2HPO_4 (Fisher Biotec, ACS reagent grade) and KH_2PO_4 (J.T.Baker, ACS reagent grade); pH 7 used 5.3 mM and 4.6 mM, respectively, while pH 8 used 9.3m M an 0.65 mM, respectively). The more alkaline solutions used a mixture of K_2HPO_4 and K_3PO_4 (BDH chemicals, ACS reagent grade); pH 9.5 used 9.5 mM and 0.5 mM, respectively, while pH 10.5 used 6.9 mM and 3.1 mM, respectively. The amounts above refer to the 10 mM orthophosphate treatment solutions; some experiments used diluted solutions at 5 mM and 1 mM.

For all treatments, suspensions used 0.1 g of powder in 10 mL of solution for up to 3 weeks in capped glass sample vials, without stirring. At regular intervals, aliquots of suspension were extracted and dried, to track any phase conversion. In some experiments, a pH meter was inserted in the supernatant to record pH at different time intervals.

4.3.4 Characterization

For bulk powder characterization, all measurements used an attenuated total reflectance (ATR) Fourier transform infrared (FTIR) spectrometer (Bruker Alpha-P, collected with a single 45 degree reflection from a diamond ATR crystal, 400-4000 cm^{-1} with 2 cm^{-1} resolution). The air-dried powders were hand ground with an agate mortar and pestle before measurement. To track polymorph conversion, we used a qualitative comparison of relative intensities of the aragonite and calcite ν_2 peaks. This method is not rigorously quantitative, but it does provide a useful metric for relative comparisons. These phase identifications are based on comparisons with mineral spectral libraries [1] We note that, in this work, ATR-FTIR enables identification of poorly crystalline and amorphous phases, which would not be feasible with

some other structural characterization methods, such as X-ray diffraction.

Powder grains were imaged by scanning electron microscope (SEM, FEI MLA 650F) using secondary electron images to assess grain morphologies. To obtain high resolution images, all the powders were mounted on carbon tape and gold coated for better SEM conductivity. Energy dispersive X-ray (EDX, FEI MLA 650F) analysis provided evidence of phosphorous incorporation.

To assess heat-related changes, we used differential scanning calorimetry (DSC, Mettler-Toledo DSC1) measurements with ∼3.5 mg of sample, weighed into an aluminum crucible, placed in a pre-heated chamber (320°C), and then heated from 320-550°C at 10°C/min under flowing N_2 (50 mL/min). To support these DSC data, additional experiments characterized the phase composition before and after heating at 440°C (pre-heated furnace) for 20-30 min, followed by an air quench. Thermogravimetric analysis (TGA, TA Instruments Q500) used 8 mg of powder for each scan, with nitrogen flow (50 mL/min) throughout the analysis. The temperature range spanned 20°C to 100°C, with a heating ramp of 10°C/min.

4.4 Results

4.4.1 Before aqueous treatments

Based on ATR-FTIR spectra (Figure 4.1a), the as-precipitated (untreated) powders show typical vibration peaks of aragonite, with a ν_3 peak (1400 cm^{-1}), ν_1 peak (1082 cm^{-1}), ν_2 (858 cm^{-1}), and ν_4 doublet (712 and 700 cm^{-1}) [129, 130]. We note that these conventional peak labels correspond to specific vibrational modes of the carbonate moieties: ν_3 is an asymmetric stretch, ν_1 is a symmetric stretch, ν_2 is an out-of-plane bend, and ν_4 is an in-plane wag. For clarity, the ATR-FTIR spectra in each Figure have explicit labels for the aragonite ν_2 and calcite ν_2 peaks. (Full-

range FTIR-ATR spectra (400-4000 cm^{-1}) are in Supplementary Material Figure 4.9.) SEM images (Figure 4.1g) show that these powder grains have an acicular morphology, which is also typical of aragonite.

We used ATR-FTIR, supported by SEM imaging, to track the phase stability of as-precipitated powders when they were exposed to water after annealing (0.1 g powder in 10 mL ultrapure water). With no annealing, there was no evidence of a calcite ν_2 peak after up to three weeks of water exposure (Figure 4.1b,h). After annealing the as-precipitated powders (400°C for 20 minutes), a calcite-related shoulder appears at 875 cm^{-1} (Figure 4.1e). Despite this secondary phase, the crystal habits of the annealed powder grains look very similar to the unannealed grains (Figure 4.1i). We note that at lower annealing temperatures (350°C) no calcite formed even after 3 hours of heat treatment (SEM images of 350°C-annealed powders are shown in Supplementary Material Figure 4.10.)

After 1 week of exposure to water (0.1 g in 10 mL nanopure water), there are significant changes to the annealed powders, in terms of the relative aragonite:calcite ATR-FTIR peak intensities (Figure 4.1f) and the crystal habits (Figure 4.1j). The ATR-FTIR data show a more pronounced ν_2 calcite peak, relative to aragonite ν_2. SEM images show many small rhombohedral crystallites that form on the needle faces, consistent with the typical calcite crystal habit (Figure 4.1g).

Based on these experiments, we see that:

(1) Aragonite alone, whether as-precipitated or subjected to a lower temperature (350°C) anneal, has good phase stability in water over a span of one week.

(2) Aragonite annealed at a slightly higher temperature (400 °C) introduces calcite as a secondary phase. Subsequent exposure to water triggers more calcite formation.

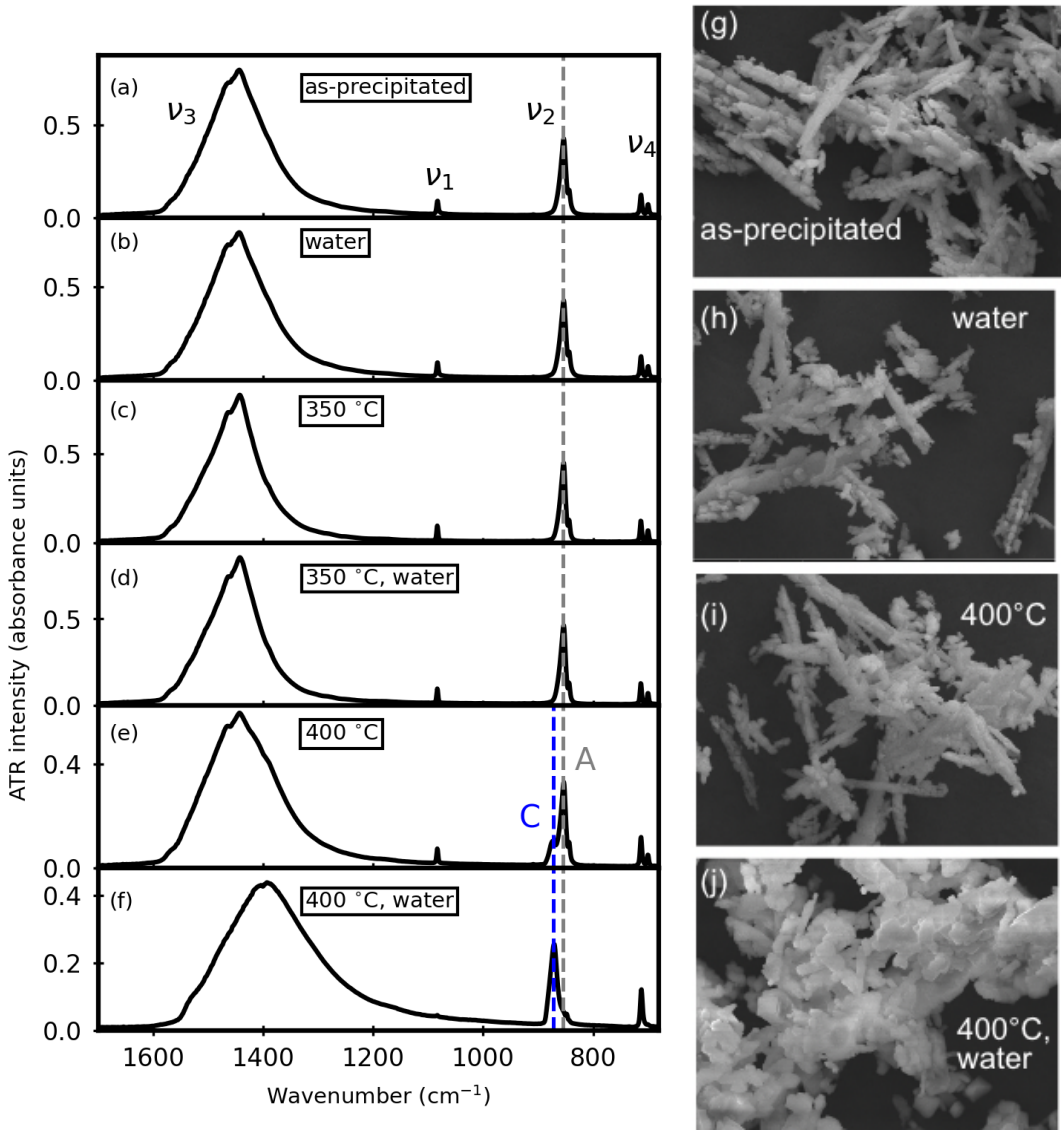

Figure 4.1: Representative ATR-FTIR spectra for (a) as-precipitated powders, (b) as-precipitated powders after 1 week in water, (c) as-precipitated powders + 350°C anneal, (d) as-precipitated powders + 350°C, then 1 week in water, (e) as-precipitated powders + 400°C anneal, and (f) as-precipitated powders + 400°C anneal, then 1 week in water. The grey vertical line (858 cm^{-1}, labelled A) corresponds to the aragonite ν_2 peak, while the blue vertical line (875 cm^{-1}, labelled C) shows the calcite ν_2 peak. Representative SEM images for (g) as-precipitated powders, (h) as-precipitated powders after exposure to water (1 week), (i) annealed, (j) annealed then exposed to water (1 week). Each image covers a width of 50 μm.

4.4.2 After aqueous treatments

We explored two different groups of aqueous phosphate treatments: polyphosphate (SHMP) solutions and orthophosphate (PO_4) solutions. Investigations involved different starting pH values (6.5-10.5) as well as different phosphate concentrations (1, 5, or 10 mM), and all utilized 0.1 g of powder in 10 mL of treatment solution.

For SHMP, whether unannealed or annealed starting powders, the ATR-FTIR spectra showed no evidence of phosphate-containing secondary phases, even up to three weeks of immersion in SHMP (1, 5, or 10 mM). Figure 4.2a,b representative spectra, which have only peaks due to aragonite (in the case of as-precipiated powders, for comparison with Figure 4.1a,b) or a mixture of aragonite and calcite (in the case of 400°C-heated powders, for comparison with Figure 4.1e,f). Furthermore, the relative aragonite:calcite peak intensities remain consistent before and after SHMP treatment, which suggests, qualitatively, that their relative fractions within the sample remain similar. (Full-range FTIR-ATR spectra are shown in Supplementary Material Figure 4.11.) SEM images (Figure 4.2d,e) show that annealing to 400 °C does not change the crystallite morphologies.

Since the SHMP-treated mixed-phase (400°C) powders had very little dissolution during treatment, we checked to see if the polyphosphate treatment created a robust change to the powder by removing it from suspension, drying, and then suspending in water. ATR-FTIR spectra of these re-suspended powders (Figure 4.2c) show consistent aragonite:calcite ν_2 IR peak intensity ratios, suggesting that no further calcite formation occurred in these resuspended powders. We note that EDX data confirmed the presence of phosphorus uniformaly on the SHMP-treated powders, even though the corresponding ATR-FTIR spectra did not show any phosphate-related peaks. Furthermore, even though the data shown in Figure 4.2 correspond to SHMP treatments with initial pH 6.5, outcomes were the same with pH-adjusted treatments at 7.0 and

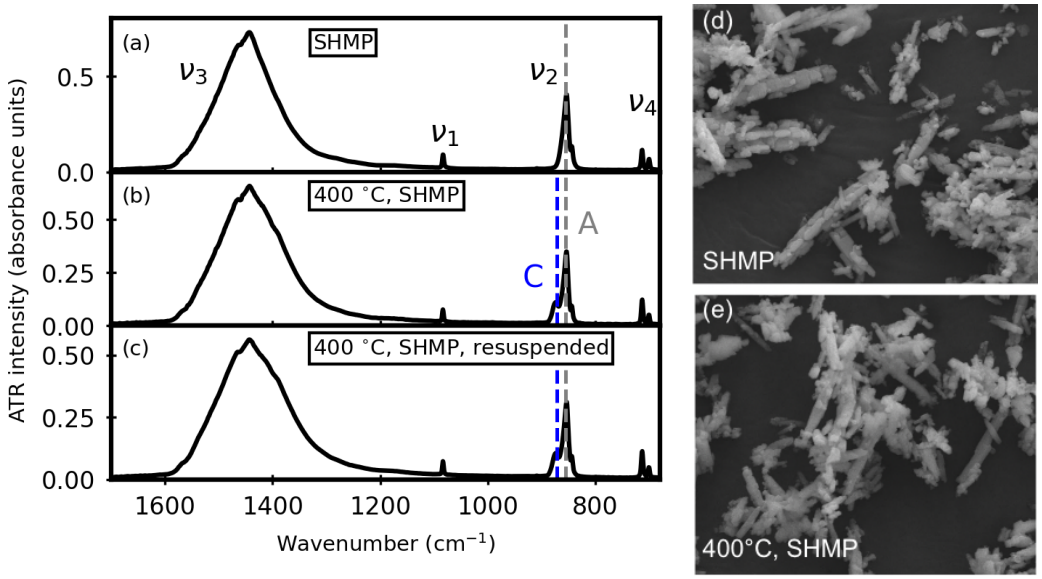

Figure 4.2: Representative ATR-FTIR spectra (a-c) and SEM images (d,e) for polyphosphate-treated powders (1 week suspension in 10 mM SHMP). The grey vertical line (858 cm^{-1}, labelled A) corresponds to the aragonite ν_2 peak, while the blue vertical line (875 cm^{-1}, labelled C) shows the calcite ν_2 peak. In all cases, the ATR-FTIR data show spectra comparable to the starting materials, with no additional peaks, and no discernable change in the relative aragonite:calcite peak intensities (compare with Figure 4.1a,e). The SEM images show that annealing to 400° does not cause any discernable differences to the crystallite morphologies. Each image covers a width of 50 μm.

10.5. (These data are provided in Supplementary Material Figure 4.12). Thus, all SHMP treatments appear to adhere to the powder, and provide protection against aragonite-to-calcite conversion in water.

To explore whether other kinds of phosphate additives have a similar effect, we investigated orthophosphate (PO_4) additives. However, orthophosphate treatments trigger significant amounts of secondary phosphate minerals, as shown by the ATR-FTIR data in Figure 4.3 (Full-range FTIR-ATR spectra are shown in Supplementary Material Figure 4.13.) For the near-neutral (pH<8.0) and the more alkaline (pH>9.5) treatment conditions, hydroxyapatite (HAp, $Ca_5(PO_4)_3(OH)$) was a dominant secondary phase. For intermediate pH values (pH 8 and pH 9.5), some brushite (dicalcium phosphate dihydrate (DCPD), $CaHPO_4{\cdot}2H_2O$) also formed .

4.4.3 pH *vs.* time trends during aqueous treatments

Since phosphate additives have buffering capacity, we monitored pH during the aqueous treatments. Figure 4.4a shows pH *vs.* time trends for a representative SHMP set of samples (analogous to data in Figure 4.2: annealed samples in water only, during SHMP treatment, and after SHMP treatment during re-suspension in water). These data show a qualitatively similar pH trend over time, with two distinct pH regimes: a fast rise in the first hour, then a steady decline thereafter.

The pH trends during orthophosphate treatments are quite different. Figure 4.4b shows trends for a set of samples analogous those described in Figure 4.3 (starting pH values ranging from 7.5 to 10.5, all at 10 mM). It is clear that none of these orthophosphate solutions act as true buffers while the powders are suspended. After 1 week, all solutions converge to a pH value of 8.6.

We are cautious interpreting these pH trends since this is a complex system. When the solid $CaCO_3$ is added to water, we expect a small amount of dissolution based

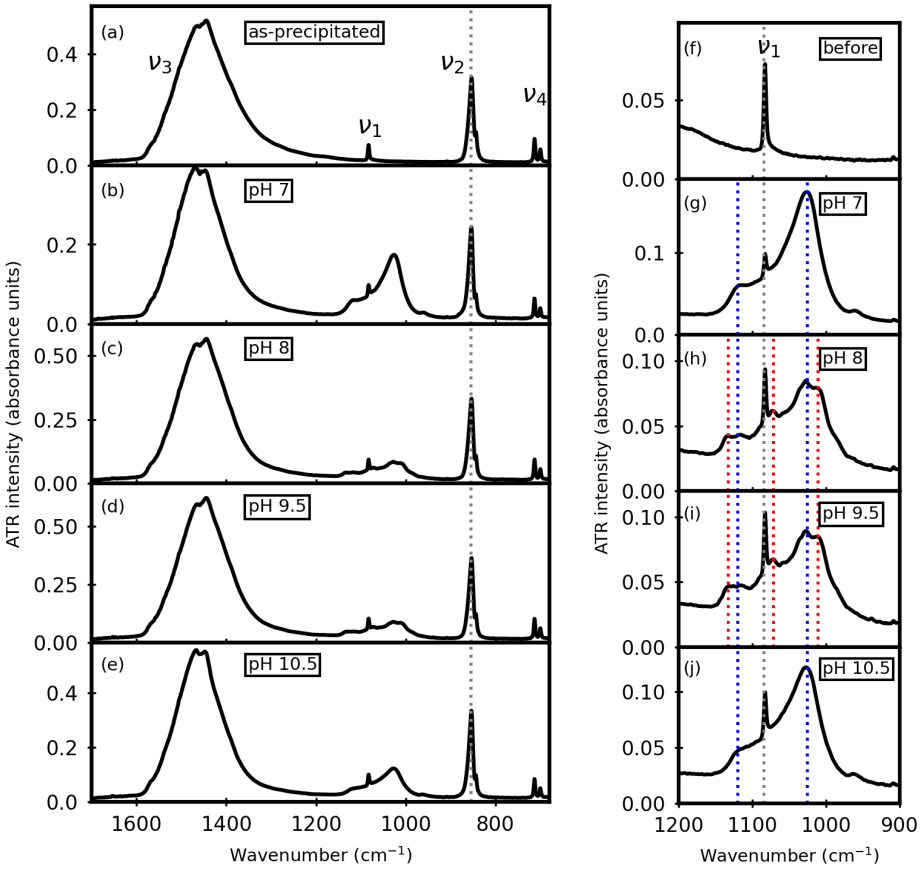

Figure 4.3: Representative ATR-FTIR data of as-precipitated powders before (a) and after orthophosphate treatments beginning near-neutral (pH 7, in (b)) to alkaline (pH 10.5, in (e)). Evidence of secondary phosphate mineral formation (900-1200 cm^{-1}) is emphasized in the zoomed panels (f-j). The grey vertical lines with band labels correspond to aragonite peaks, while the blue vertical lines and red vertical lines denote the peak positions of HAp and brushite, respectively.

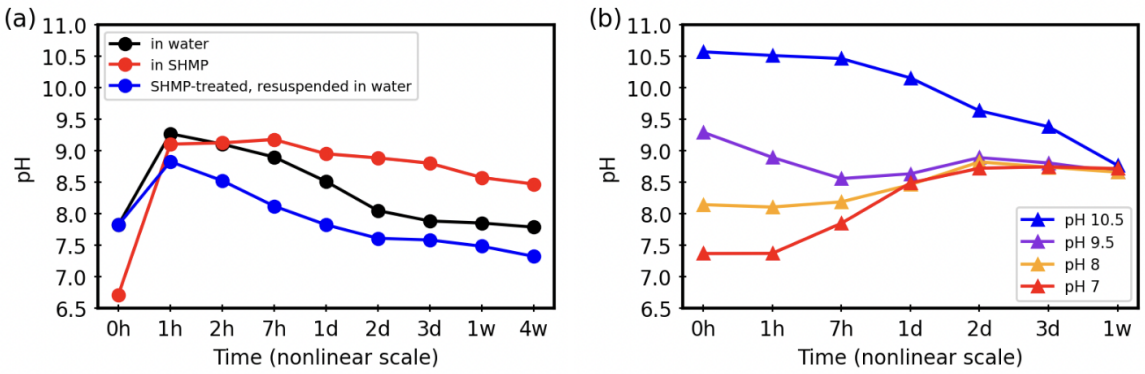

Figure 4.4: Representative pH *vs.* time trends for (a) SHMP-treated samples (annealed, SHMP-treated, and re-suspended SHMP-treated powders; see also Figure 4.2) and (b) orthophosphate-treated samples (different starting pH values, all at 10 mM; see also Figure 4.3).

on the known solubility constants for calcite and aragonite. Dissolution of ambient CO_2 in the water also affects the ionic composition of the solution over time. Both of these factors contribute to changes in the point of zero charge (PZC) for calcium carbonate particles, due to influence by ions in and near the particle surfaces [131].

4.4.3.1 Thermal stability after aqueous treatments

We also followed the phase behaviour when phosphate-treated powders were subjected to thermal treatments, using differential scanning calorimentry (DSC) to look for endothermic peaks related to phase changes. We expect a thermally induced aragonite-to-calcite transition, based on studies by other [132, 133]. Figure 4.5 shows DSC scans at 10°C/min, where endothermic peaks are visible in both treated and untreated samples, with comparable peak areas. However, the DSC peak occurs at higher temperatures in SHMP-treated samples (465°C, regardless of SHMP treatment concentration) compared to the untreated sample (435 °C). We note that the peak area from the as-precipitated aragonite is slightly larger than that of SHMP-treated samples. Our data do not provide a conclusive explanation for this observation, but

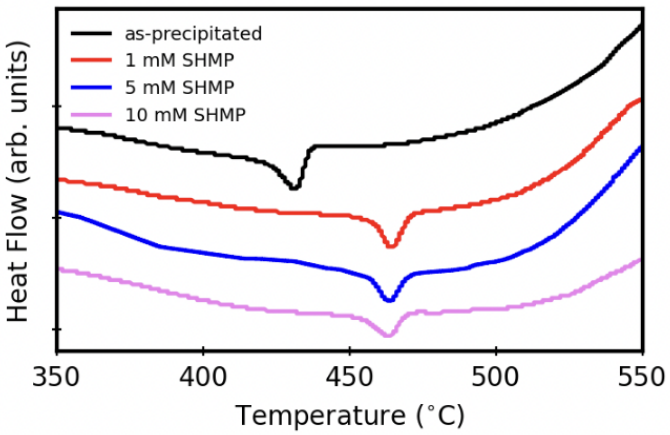

Figure 4.5: Representative DSC traces for as-prepared and SHMP-treated powders, all at 10°C/min heating. Endothermic peaks point downward. Data curves are offset along the vertical axis for clarity.

we speculate that it could be related to phase changes that involve the phosphate.

To confirm that the endothermic DSC peak is due to an aragonite-to-calcite phase conversion, we used ATR-FTIR to assess the phase composition of the samples after the DSC measurement. Figure 4.6 shows that the DSC heating profile caused complete conversion to calcite as-precipitated and SHMP-treated samples; after heating, the aragonite ν_1 and lower-wavenumber ν_4 peaks disappear completely, and the ν_2 peak shifts to slightly higher wavenumber. For the SHMP-treated sample (10 mM), there is also a broad rise in the baseline between 1000-1200 cm^{-1}, which is consistent with what others have reported for poorly crystallized phosphate phases [1]. Therefore, heating SHMP-samples to high enough temperatures can trigger both aragonite-calcite conversion and phosphate secondary phase formation. Even so, SEM images of powders after DSC measurements (Figure 4.6b) do not show any appreciable crystal morphology changes, maintaining their acicular crystal habits. Research by others [134] shows that calcite-after-aragonite pseudomorphs can form, wherein calcite forms after annealing aragonite, but the crystal morphologies do not change. This means that SEM was not effective in tracking heat-induced phase transformations

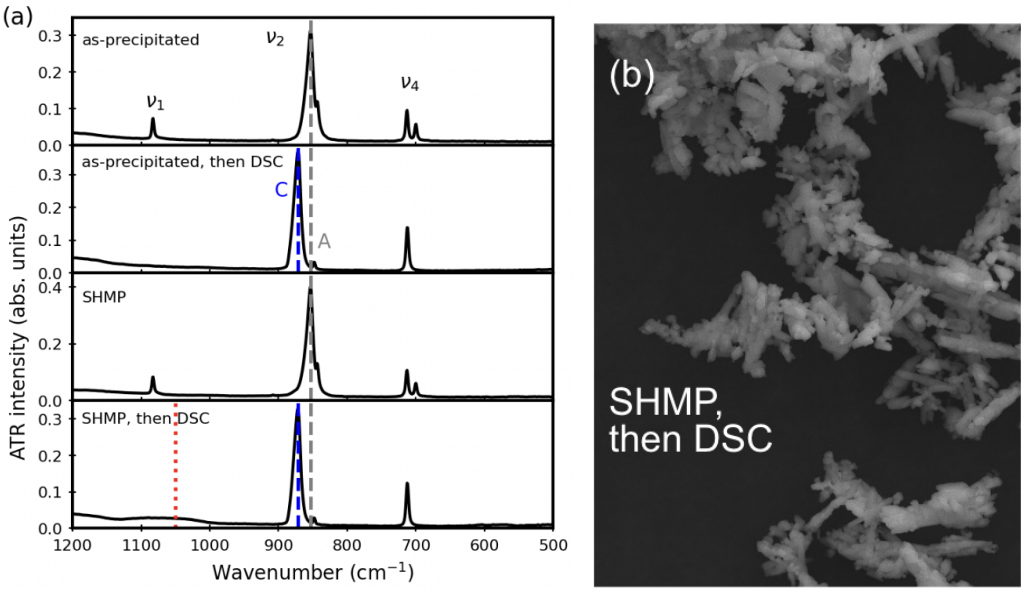

Figure 4.6: (a) Representative ATR-FTIR spectra show that, after DSC measurements, both the as-precipitated and SHMP-treated powders convert entirely to calcite (no ν1 peak, and only one ν4 peak). The grey vertical line (858 cm^{-1}, labelled A) corresponds to the aragonite ν_2 peak, while the blue vertical line (875 cm^{-1}, labelled C) shows the calcite ν_2 peak. The SHMP-treated sample (10 mM) also shows a very broad peak in the 1000-1200 cm^{-1} region (indicated by the red vertical dotted line), suggestive of a small phosphate secondary phase [1]. (b) Representative SEM image of SHMP-treated aragonite after DSC measurement, covering a width of 50 μm.

because calcite appears in an atypical pseudomorphic crystal shape.

In separate experiments, we annealed SHMP-treated aragonite at 440°C for 30 min. This higher temperature and longer annealing time provided even stronger evidence for phosphate remaining on the powders after SHMP treatments. ATR-FTIR data in Figure 4.7a show that higher SHMP solution concentrations during treatment cause show the highest phosphate-related hump (1000-1200 cm^{-1}). We also note that the untreated sample has no aragonite remaining after heating, while the SHMP-treated samples all have some aragonite peak intensity remaining after heating.

For comparison, we also annealed the orthophosphate-treated aragonite under the same conditions (440°C for 30 min). Representative ATR-FTIR data show that, for

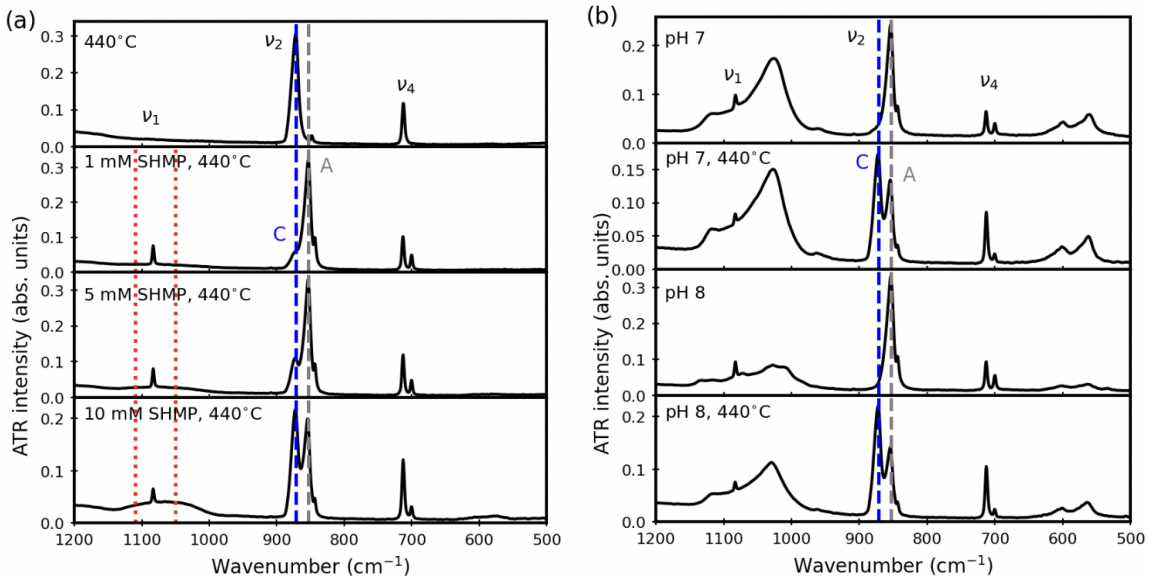

Figure 4.7: Representative ATR-FTIR data for samples annealed at 440°C after aqueous treatment in either (a) SHMP (1, 5, 10 mM) or (b) orthophosphate (pH 7 or pH 8, both at 10 mM). The grey vertical line (858 cm^{-1}, labelled A) corresponds to the aragonite ν_2 peak, while the blue vertical line (875 cm^{-1}, labelled C) shows the calcite ν_2 peak. The red dotted lines indicate poorly crystalline phosphate secondary phases.

samples that had predominant HAp secondary phase before heating, the annealing treatment did not cause a significant change in the HAp peaks. However, these samples did show decreased aragonite peak intensities and increased calcite peak intensities; as an example, the top two panels of Figure 4.7b show samples treated at pH 7 (10 mM) before and after heating. For samples that had both HAp and brushite before heating, the annealing treatment caused thermal conversion of aragonite to calcite, as well as thermal coversion of brushite to HAp. As an example, the bottom two panels of Figure 4.7b show samples treated at pH 8 (10 mM) before and after heating. We note that there are also changes in the relative intensities of the calcite and aragonite peaks, but our ATR-FTIR data cannot provide a definitive answer to whether aragonite is consumed to form the phosphate-bearing minerals at the expense of calcite, or if the phase transition to calcite is an intermediate step.

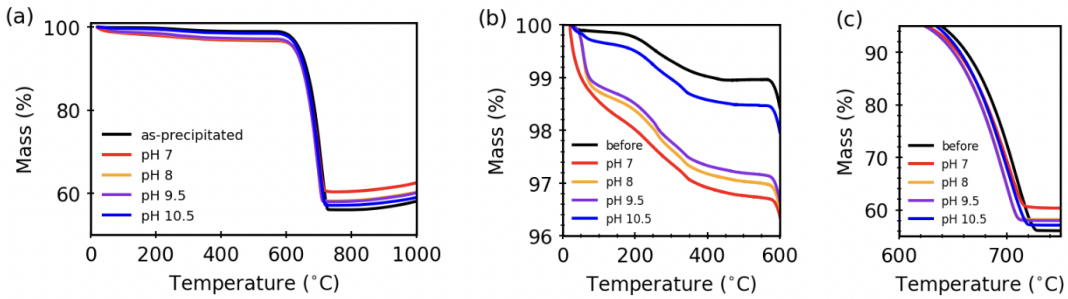

Figure 4.8: Representative TGA traces compared as-precipitated and orthophosphate-treated powders during 10°C/min heating. The full temperature range is shown in (a), while (b) and (c) zoom in on the low-temperature and high-temperature transition regions, respectively.

To analyze the evolution of the phase composition changes in the orthophosphate-treated samples in more detail, we used thermogravimentric analyses (TGA) from 20-800 °C. Figure 4.8 compares the changes in % mass, at 10°/min sweep rate, of powders treated with orthophosphate at different starting pH values (all at 10 mM). The full temperature range (Figure 4.8a) shows qualitatively similar mass changes in all samples, with small mass losses below 600°C and a steep mass loss near 700°C.

Looking more closely at the low-temperature range (Figure 4.8b), the pH 10.5 sample is most similar to the as-precipitated sample, with plateaus at 100-200°C and from 400-600°C, for a total mass loss in the range of 1%. In contrast, Figure 4.8b also shows that there are larger mass losses for samples treated in the pH 7-9.5, range, with no clear plateaus and a total mass loss near 3%. For the higher TGA temperature range (Figure 4.8c), all samples show similar rapid mass losses beginning near 575°C and ending by 750°C, leaving only 58-63% of the total weight in the solid. Values for these changes are compared in Table 4.1.

The large mass loss near 700°C is consistent with calcination, whereby $CaCO_3$ transforms to CaO as CO_2 is released [135]. Based on this, we calculate the ideal % mass loss due to calcination. Then, we assume that the difference between this

Table 4.1: Summary of % mass losses during TGA measurements for powders with orthophosphate treatements at different starting pH values.

Sample/Mass (%)	Low T loss (20-575°C)	High T loss (575-750°C)	Assumed CaO mass remaining	Excess mass remaining
ideal	0.0%	43.0%	57.0%	0.0%
as-precipitated	1.1%	40.9%	54.2%	3.8%
pH 10.5	1.6%	39.4%	52.2%	6.8%
pH 9.5	2.9%	37.0%	49.0%	11.1 %
pH 8	3.0%	36.7%	48.6%	11.7 %
pH 7	3.3%	34.2%	45.3%	17.2 %

ideal mass loss (due to full calcination) and the observed mass loss (Figure 4.8) is due to calcium phosphate secondary phases, which gives us an estimate of % mass of secondary phases and/or uncalcined $CaCO_3$ that remains in each sample. A summary of these estimates appears in Table 4.1.

4.5 Discussion

Here, our work contrasts the differences between polyphosphate and orthophosphate treatments, as applied to solution-precipitated aragonite powders. Polyphosphate treatments not only help to prevent against aragonite dissolution during exposure to water, but they also provide a slight increase in the thermal stability of aragonite with regard to conversion to calcite. In contrast, orthophosphate treatments trigger secondary phases to form during the treatments, which leads to more complex thermal annealing behaviours.

In the aqueous treatments described herein, we used comparable phosphate concentrations between the polyphosphate and orthophosphate solutions. As a result,

our orthophosphate treatments were not designed to be effective buffers, even though they used standard buffer salts. To explain this in more detail, the normal range for potassium phosphate buffers based on K_2HPO_4 and KH_2PO_4 is pH 6-8, based on the Henderson-Hasselbalch Equation [136] (Equation 4.1)

$$\mathrm{pH} = \mathrm{p}K\mathrm{a} + \log([\mathrm{base}]/[\mathrm{acid}]). \tag{4.1}$$

In this case, KH_2PO_4 functions as the acid while K_2HPO_4 is the conjugated base. To achieve buffering at higher pH values, K_2HPO_4 becomes the acid and one must use a different salt, K_3PO_4, as the conjugated base. In general, a buffer is effective only when the base:acid ratio is in the range of 0.1-10, with the best buffering at a ratio of 1. Our orthophosphate treatments have ratios that are not unity: some are within the useful range (1.1 for pH 7 and 0.4 for pH 10.5), but others are well outside of it (15 for pH 8 and 0.05 for pH 9). Therefore, it is not surprising that Figure 4.4 shows that none of the orthophosphate treatments function as true buffers while the powders are in suspension. Furthermore, we note that Figure 4.4 shows pH *vs.* time data for suspensions with the highest orthophosphate concentrations of this study (10 mM); the diluted treatments (1 mM, 5 mM) have even less buffering capacity.

Our TGA data (Figure 4.8 and Table 4.1) provides a useful complement to the secondary phase information we gathered from ATR-FTIR spectral data (Figures 4.3). Mass loss at lower temperatures may be due to the loss of the structural water, especially in phases such as brushite [137]. However, we see that even in the as-precipitated sample, there is 1% mass loss below 575 °C. Furthermore, the pH 7 sample, which showed only HAp and not brushite, shows the highest mass loss below 575 °C (just above 3%). Based on these data, it is likely that the low T mass losses are not due solely to structural water.

For the high temperature mass loss (575-750 °C) that we attribute to $CaCO_3$

calcination, we see in Table 4.1 that even the as-precipitated sample has incomplete calcination (3.8% excess mass). The excess mass increases as the pH of the orthophosphate treatment decreases, reaching a maximum of 17% for the pH 7 treatment. For the orthophosphate-treated samples, the ATR-FTIR spectra confirm that secondary phosphate phases HAp and brushite are present; work by others shows that the thermal decomposition temperature for HAp happens at temperature above our TGA data range (1000-1360 °C [138]). Thus, we infer that the excess mass likely includes a combination of uncalcined $CaCO_3$, HAp, and monetite ($CaHPO_4$, anhydrous form of brushite [139]).

Work by others provides support for our pH-dependent trends in secondary phase formation. While μM concentrations are often too low to trigger significant phosphate mineral formation in the presence of $CaCO_3$ [56, 57], higher (mM) phosphate concentrations have been shown to cause phosphate mineralization [61]. In acidic and neutral environments, the strong dissolution of calcium carbonate contributes to the interaction between calcium and phosphate ions, resulting in calcium phosphate precipitates [58]. However, as pH increases, phosphate uptake gradually decreases due to inhibition of calcium carbonate dissolution; is is consistent with the excess mass trend we see from TGA data (Table 4.1), where the excess mass (due in part to phosphate uptake) is largest for the most acidic orthophosphate treatment (pH 7).

With respect to phases formation, ${HPO_4}^{2-}$ ion is ubiquitous at pH 7-10 and this range often produces brushite. Outside of this range, HAp is the dominant phase [59], which is consistent with our findings of brushite only after pH 8.0-9.5 orthophosphate treatments.

Comparing the phase complexity of the orthophosphate-treated powders to the almost-unchanged SHMP-treated powders, it is apparent why polyphosphate is widely used as a dispersant and anti-flocculant. It is worthy of note that our 10 mM treat-

ments are equivalent to 6 g/L, which is at orders of magnitude higher concentrations compared to other recent studies [24]. Even with the high concentrations, we find that any secondary phosphate phases are barely detectable with ATR-FTIR spectra, even after annealing. Despite the widespread use of SHMP, its surface-specific interactions with calcium carbonate are poorly studied.

Finally, we note that aragonite dissolution in the presence of calcite has been noted by others [3]. Aragonite powders are only slightly soluble in water, based on their solubility constants [140]. However, the presence of secondary calcite can cause aragonite to dissolve much more rapidly [115].

4.6 Conclusions

Our work compares aqueous polyphosphate and orthophosphate treatments on aragonite, using similar phosphate concentrations throughout. Polyphosphate treatments not only help to prevent against aragonite dissolution during exposure to water, but they also provide a slight increase in the thermal stability of aragonite with regard to conversion to calcite. In contrast, orthophosphate treatments trigger secondary phases to form during the treatments, which leads to more complex thermal annealing behaviours.

4.7 Supporting information

Figure 4.9: Full-range ATR-FTIR data to complement Figure 4.1; Figure 4.10: Additional SEM images to complement Figure 4.1; Figure 4.11: Full-range ATR-FTIR data to complement Figure 4.2; Figure 4.12: ATR-FTIR data to complement Figure 4.2; Figure 4.13: Full-range ATR-FTIR data to complement Figure 4.3.

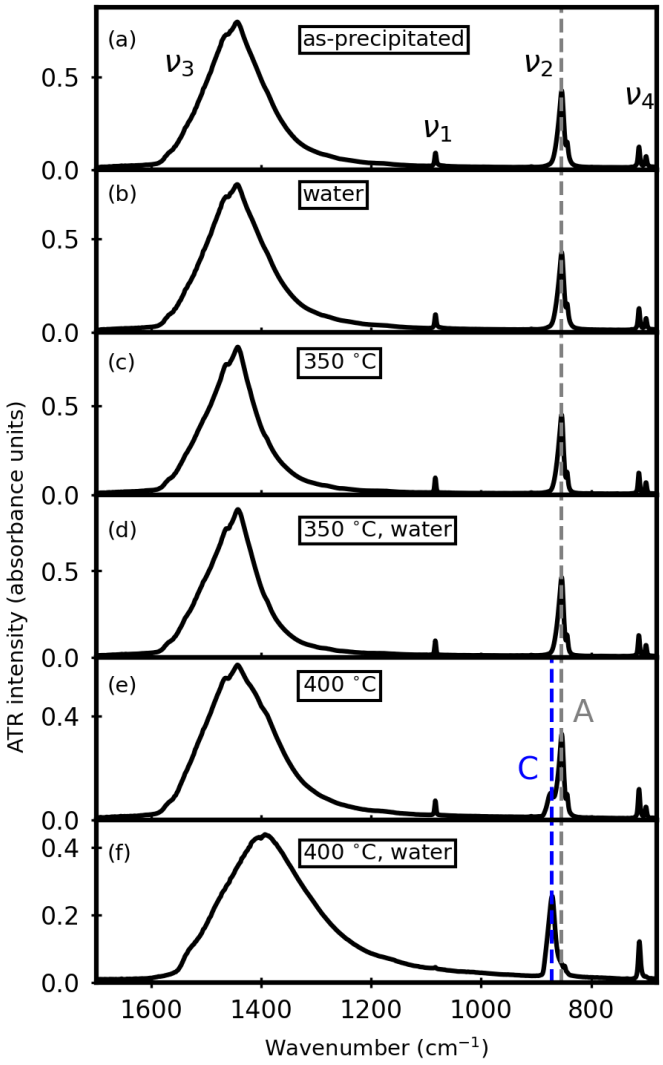

Figure 4.9: Representative full range ATR-FTIR spectra (400-4000 cm^{-1}) for (a) as-precipitated powders, (b) as-precipitated powders after 1 week in water, (c) as-precipitated powders + 350°C anneal, (d) as-precipitated powders + 350°C, then 1 week in water, (e) as-precipitated powders + 400°C anneal, and (f) as-precipitated powders + 400°C anneal, then 1 week in water. These data complement Figure 4.1 in the main text.

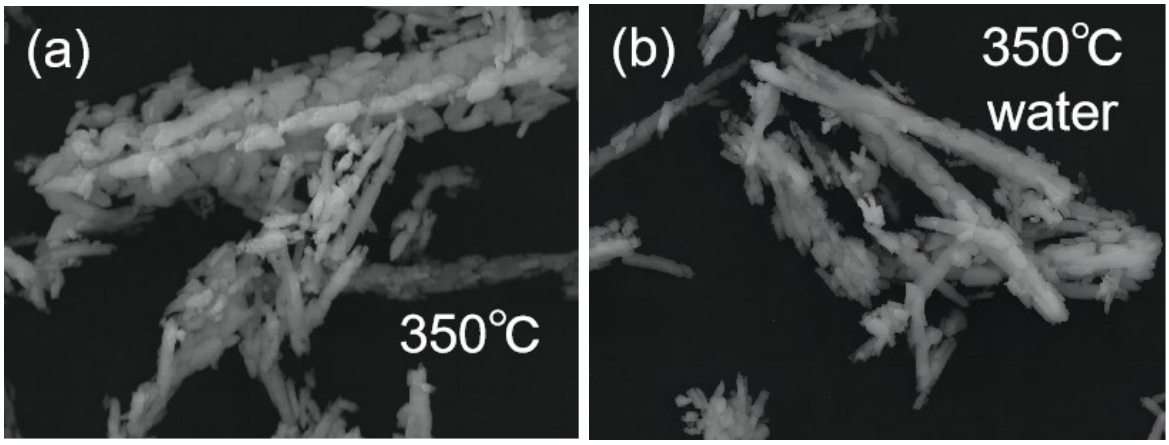

Figure 4.10: Representative SEM images for (a) 350°C annealed, (b) 350°C annealed then exposed to water (1 week). Each image covers a width of 50 μm. These data complement Figure 4.1 in the main text.

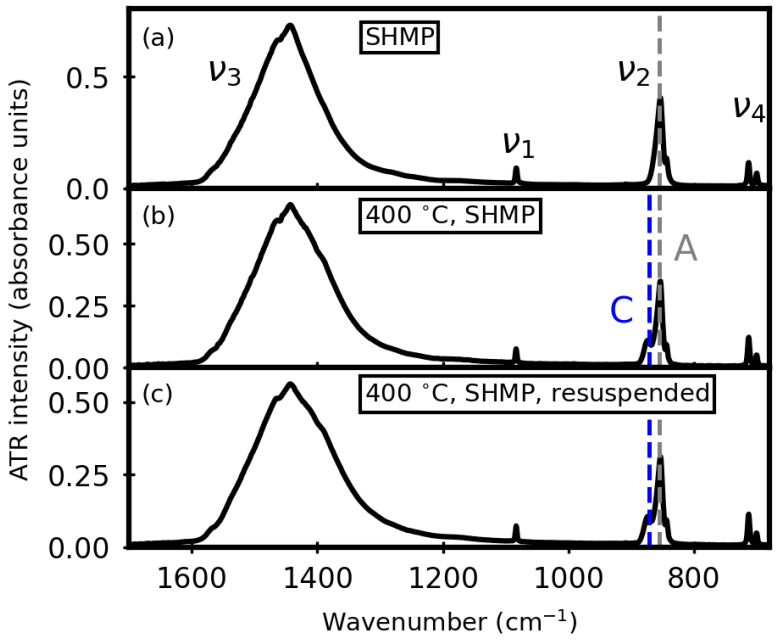

Figure 4.11: Representative full-range ATR-FTIR spectra (400-4000 cm^{-1}) for polyphosphate-treated powders after 1 week of suspension in 10 mM SHMP. These data complement Figure 4.2 in the main text.

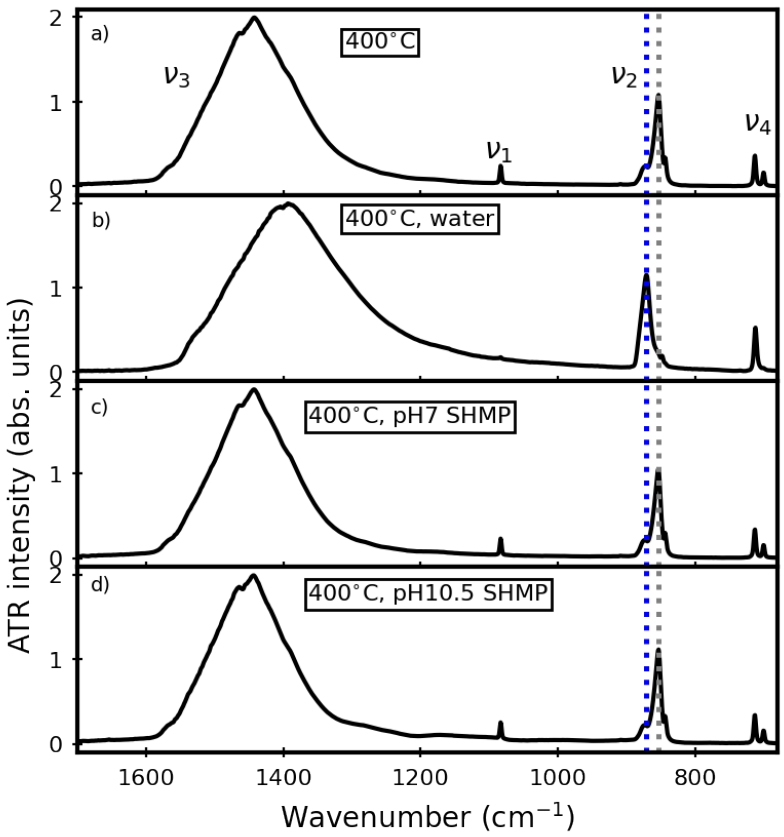

Figure 4.12: Representative ATR-FTIR spectra for (a) as-precipitated powders + 400°C anneal, (b) as-precipitated powders + 400°C anneal, then 1 week in water. (c) as-precipitated powders + 400°C anneal, then 1 week in pH 7 10 mM SHMP. (d) as-precipitated powders + 400°C anneal, then 1 week in pH 10.5 10 mM SHMP. The grey vertical dotted line (858 cm^{-1} corresponds to the aragonite ν_2 peak, while the blue vertical dotted line (875 cm^{-1}) shows the calcite ν_2 peak. These data complement Figure 4.2 in the main text.

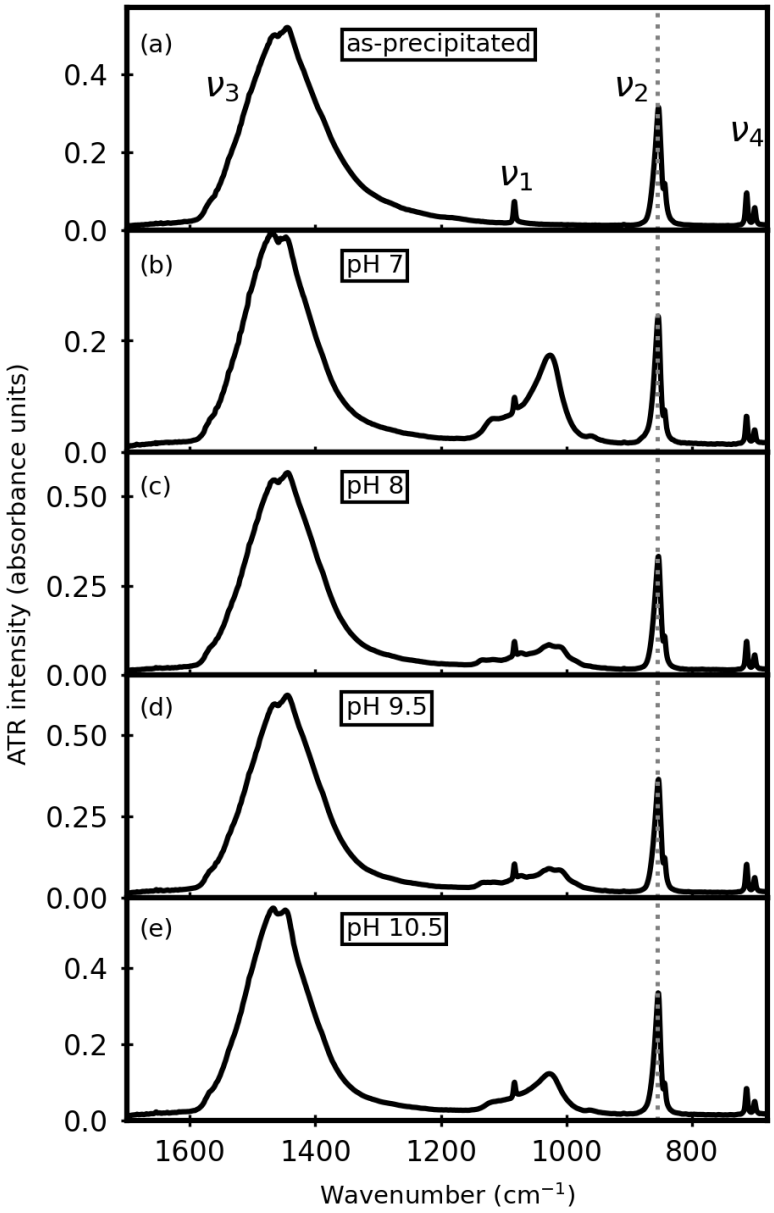

Figure 4.13: Representative full-range ATR-FTIR sepctra (400-4000 cm^{-1}) of as-precipitated powders before (a) and after orthophosphate treatments beginning near-neutral (pH 7, in (b)) to alkaline (pH 10.5, in (e)). These data complement Figure 4.3 in the main text.

4.8 Author contributions

Conceptualization, methodology, writing – original draft preparation, review and editing: B.G. and K.M.P.; investigation and data curation: B.G.; supervision, project administration, and funding acquisition: K.M.P. All authors have read and agreed to the published version of the manuscript.

4.9 acknowledgments

J.B. Lin (ICP-OES, DSC, and TGA at the Centre for Chemical Research and Training) and the Microanalysis Facility (SEM/EDX) of Memorial University's CREAIT network for access to characterization facilities. A. Schmidt and S. Kababya (Technion, Israel Institute of Technology) for insightful conversations.

Chapter 5

Mid-infrared spectra identify carbonate mineral polymorphs at terrestrial sites of serpentinization

We plan to publish the contents of this chapter in an open-access journal related to astrobiology, since the main application of this work is toward detecting signature of past or present life on other planets. The authors of this paper are Boyang Gao, Emmeline Williams, Dr. Kristin M. Poduska and Dr. Penny L. Morrill. Boyang Gao carried out the experiments, data analysis and contributed to the writing of the manuscript. Emmeline Williams helped on the data collection and analysis. Dr. Kristin Poduska provided guidance over the experimental design, data analysis, and the writing of the manuscript. Dr. Penny L. Morrill is the principal investigator (PI) of the whole research project, who proposed the research plan and coordinated the fieldwork.

5.1 Abstract

We use infrared (IR) spectral information from lab-based measurements of ground-truthed samples to detect above-ground expressions of serpentinization in the form of calcium carbonate ($CaCO_3$). The field samples were collected at a Mars-analogue site located in the Bay of Islands Ophiolite Complex (Newfoundland and Labrador, Canada) during the period from 2019-2021. Based on these data, we outline how IR data collection for optimal ground truthing is different from mimicking remote sensing IR spectra from satellites and drones. This includes comparison of ground-truthed samples as well as lab-synthesized standards in the mid-infrared (MIR) range (400-4000 wavenumbers, or 25-2.5 microns). As an example of the value of ground-truthing, we show calcite *vs.* aragonite identification in ground-truthed samples that would not be visible in the wavelengths targeted by remote sensing IR spectrometers. This is due to spatial-resolution and wavelength-resolution differences between the optimal lab-based MIR measurements and optimal remotely sensed IR spectra. We discuss the useful implications this has for Earth-based investigations related to serpentinization.

5.2 Introduction

The presence of carbonate on the surface of serpentine-containing ophiolite rock can be indicative of past or present subsurface water-rock reactions known as serpentinization that have the ability to support microbial life. Serpentinization occurs when groundwater comes into contact with Fe- and Mg-silicate ultramafic minerals, resulting in H_2 production, high pH (11-12) groundwater, and a range of Fe- and Mg-containing secondary mineral phases [141–143]. Previous reports have shown that this H_2 could sustain microbial life [144, 145]. The serpentinization process has also been shown to trigger high Ca^{2+} concentrations due to decomposition of nearby Ca-

containing silicate minerals [142,146]. As the Ca-rich water discharged at the surface and comes in contact with atmospheric CO_2, calcium carbonate precipitation can occur, thereby serving as a surface expression of the subsurface serpentinization reaction [147,148]. Such surface expressions are especially important to identify where serpentinization may have occurred in extraterrestrial environments, such as rocky Mars or icy Enceladus [149, 150]. Thus, surface carbonates adjacent to ultramafic rocks can be a marker for sites of past or present habitable environments. In this work, we show that infrared (IR) spectra of carbonate minerals, obtained from both laboratory and field investigations, play an important role in proof-of-principle exercises that simulate end-to-end missions designed to increase the chance of detecting life on other worlds.

Because remote detection has been a key part of Mars missions, there is already an extensive body of work that compares satellite and drone-based hyperspectral imaging in the visible, near IR (NIR), and short wave IR (SWIR) ranges to identify serpentinization-relevant minerals. Hyperspectral studies involve data in multiple target bands, each of which spans a small range of energies that targets signals from distinct types of materials. For example, the widely used WorldView-3 terrestrial satellite collects data in 6 visible bands (corresponding to the red, red edge, coastal, blue, green, and yellow that our eyes can see), two NIR bands (different electronic excitations in chlorophyll, for example), and 8 SWIR bands (targeting atmospheric gases and other features) [151]. Hyperspectral analyses in similar ranges have been conducted with data from the Mars Curiosity rover and earlier orbital data [152–155]. There is also continued interest in lab-based and field-based investigations that correlate hyperspectral images and visible-NIR-SWIR spectra with structural information from X-ray diffraction (XRD) data and elemental information from energy dispersive X-ray (EDX) mapping [156–158]. In all of these examples, there is a balance of factors

at play in making connections between lab-based and field-based data: spatial range and spatial resolution of the images, and spectral range and spectral resolution of the infrared spectral data [159]. In addition to these factors, the literature also shows that surface texture alters spectral data due to angle-dependent reflection and absorption differences, which can make remote detection challenging [160].

Even with the success of hyperspectral imaging in the visible-NIR-SWIR range, there are major disadvantages when it comes to mineral identification. In this energy range, photons are absorbed by atmospheric gases [161], and also in solids due to electronic transitions. In materials such as carbonates, any such electronic transitions are due to transition metal impurities (such as Fe^{2+}), rather than elements that make up the majority of the material [162]. A more robust mineral identification strategy involves the use of lower energy photons in the mid-infrared (MIR) range that correspond to bond vibration energies. The energies and intensities of these MIR absorbance peaks give spectral "fingerprint" that are unique to different minerals, even when their atomic compositions and crystal structures are very similar [163]. The tradeoffs for this superior mineral identification is that MIR instrumentation is much heavier, bulkier, and more expensive for deployment in remote sensing applications. Even so, there is current interest in compiling and cataloging spectra for carbonates and other minerals across the full IR spectral range [164]. Pilot projects have also explored MIR spectra as an indirect method to detect biogenic carbon residues in Mars-like clay minerals [165].

In this work, we demonstrate that MIR spectra of ground-truthed samples can offer different and valuable information that can augment SWIR spectra obtained by remote sensing. In this way, we show that there is still much to learn from terrestrial-based investigations of serpentinization processes that can help inform future missions in the search for extraterrestrial microbial life.

5.3 Experimental details

5.3.1 Samples

Hand samples were collected from the Bay of Islands Complex (BOIC), including a training site (Winterhouse Canyon (WHC), in the Tablelands within Gros Morne National Park) and the New site (Blow Me Down (BMD) massif, near York Harbour, NL). Hand sampling criteria emphasized colour and texture, as well as context. Further details of the context for these sites is given in our SERP overview paper and in previous work [145]. In all cases, field work was timed in summer to minimize the likelihood of snow cover. In brief, we used satellite images to identify carbonates on ultramafic rocks that were near water features such as streams or steep slopes. We then explored on foot these areas to look for white carbonate precipitates; some of these covered several square meters, but most were much smaller (1 m^2 or less) and were not wholly continuous over that area. Samples were removed with small knives and stored in vials or bags.

To assess calcium carbonate content in hand samples while in the field, we used a acid test with HCl. It is useful to note that calcium carbonate minerals such as calcite and aragonite readily fizz and dissolve in HCl, but Mg-containing carbonates such dolomite or clay-rich carbonates such as marl have much slower dissolution and do not fizz.

We also used two different calcium carbonate mineral polymorphs, calcite and aragonite (both $CaCO_3$), in the laboratory to compare with the field specimens. Calcite was purchased (Sigma-Aldrich, ACS reagent grade). Aragonite was synthesized by adding 25 mL of 60 mM Na_2CO_3 dropwise to 25 mL 60 mM $CaCl_2$ over a 3 minute span, while stirring at 400 rpm and holding solutions at 90 °C [96]. The resulting precipitate was separated by centrifugation (4000 rpm for 10 min) followed by filtration,

and then dried at ambient temperature for 12 hours.

5.3.2 Infrared spectroscopy

IR spectra were collected in an Attenuated Total Reflectance (ATR) geometry (Bruker Alpha with Diamond ATR and OPUS software). Fine particles (a few mg in total) were scraped from the rock samples, ground by hand with a mortar and pestle, and then pressed against the ATR crystal to ensure tight contact. The broad-band IR beam generated in the spectrometer is internally reflected off of this crystal, and the resulting spectra show which energies were absorbed by the sample. Spectra spanned the MIR range (400-4000 cm^{-1}, resolution 2 cm^{-1}), but the figures herein show a smaller range that focuses on the fingerprint region (400-1600 cm^{-1}) for greater clarity.

Spectra were analyzed and plotted with Quasar and Orange Spectroscopy [166], which are open source data analysis packages for Python. All spectra are shown as-collected, with no baseline correction or filtering. Mineral identification was based on comparisons with previous work [110] as well as with a mineral IR database [1]. General strategies for using MIR for mineral identification during field work are well-established and are described in reviews by others [161, 163].

5.4 Results and Discussion

5.4.1 SWIR *vs.* MIR

Mineral identification in the MIR range is much more robust than in the vis-NIR-SWIR range. Figure 5.1a compares NIR-SWIR reflectance spectra for geogenic calcite and serpentine [167], where mineral absorbance appears as downward-pointing peaks. For ease of comparison, the eight WorldView-3 satellite SWIR bands [151] are

denoted with vertical dashed lines. Most of the spectral differences between these two minerals in the SWIR range occur at wavelengths that are not covered by the satellite bands. This means that the procedure involved in analyzing NIR-SWIR spectra to detect calcite is feasible [152], but cumbersome. In contrast, the MIR range (Figure 5.1b) makes differentiating among serpentine, calcite, and aragonite much easier. To make a more explicit connection between the SWIR and MIR ranges, the spectra in Figure 5.1b are displayed as a function of both wavelength (top) and wavenumber (bottom) for the horizontal axis. For the vertical axis, convention dictates that ATR spectra are plotted as absorbance, so mineral absorbance appears as upward-pointing peaks.

Since our field investigations were geared toward detecting carbonate minerals as surface expressions of the serpentinization process, our MIR studies focus on the carbonate minerals aragonite and calcite (both $CaCO_3$). The distinct carbonate vibrational mode signatures are well-studied experimentally and theoretically. Each vibrational mode corresponds to specific atomic motions in the solid that can be easily visualized with simulations [168]. For calcite, there are three carbonate-related peaks: a wagging mode at 712 cm^{-1}, an out-of-plane vibration at 875 cm^{-1}, and an asymmetric stretch at 1480 cm^{-1} [110, 130]. Aragonite has peaks for these three vibrational modes (at 712 cm^{-1}, 858 cm^{-1}, and 1450 cm^{-1}), as well as two additional peaks at 700 cm^{-1} and 1090 cm^{-1} [169].

The data presented in this work will be ATR spectra in the MIR range, like those shown in Figure 5.1b, which give us the clearest option for mineral identification.

5.4.2 Ground-truthed samples at BIOC

As described above, we used satellite images to identify carbonate areas that were near fresh water features such as streams. We then ground-truthed the most promising

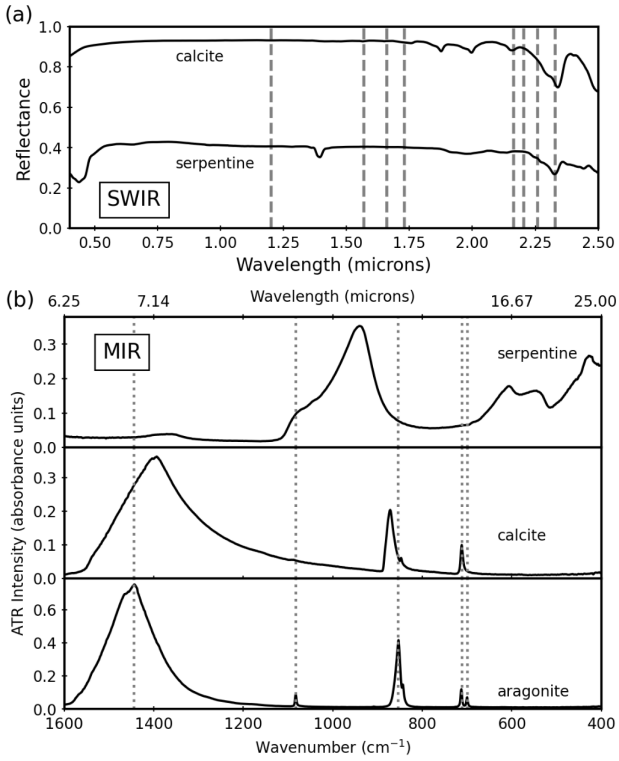

Figure 5.1: (a) Reflectance SWIR spectral standards for calcite and serpentine from the United States Geological Survey database. On the vertical axis, 1.0 denotes complete reflection, so absorption by the mineral appears as downward-pointing peaks. Note that most of the spectral differences between these two minerals occur in ranges that are not covered by the eight WorldView-3 satellite SWIR bands, which are indicated by the vertical dashed lines. (b) Representative fingerprint-range MIR spectra for calcite, aragonite, and serpentine, collected using attenuated total reflectance (ATR). On the vertical axis, 0.0 denotes complete reflection, so absorption by the mineral appears as upward-pointing peaks. The dotted vertical lines show the position of the five dominant aragonite peaks.
Reflectance SWIR data is based on the United States Geological Survey database [167]

regions to look for white precipitates indicative of carbonates; some of these covered several square meters, but most were much smaller (1 m^2 or less) and were not wholly continuous over the area. Once we located carbonate precipitates, we tested the pH of nearby water, which was typically in the form pools of standing water, wet seepage around nearby rocks, or flowing streams. We also inspected and sampled nearby areas as control specimens to assess the extent to which carbonate minerals were present in sediments. In all cases, the control specimen spectra showed serpentine, with very low background carbonate levels.

We summarize our findings in two groupings. First, we focus on carbonates found near high-pH pools, where we have multiple indicators for the serpentinization reaction, including an aqueous environment that could support microbial life. Second, we consider carbonates that were not in the immediate vicinity of high-pH water. In this latter group, there was always evidence of nearby water, but tests indicated near neutral pH. Examples of each type of area are shown in Figure 5.2.

5.4.2.1 Near high-pH pools

The training site (WHC) is notable for one deep pool that is subsurface-fed, have a high pH near the water inlet, and are surrounded near the edges and outside of the pool by thick white laminated crusts [145]. These white precipitate have persisted over a span of decades, but they change their shape and thickness from year to year. Samples of these thick white crusts collected in 2009 and 2019 showed calcite. However, during the 2021 field season some specimens were predominantly aragonite while others were entirely calcite. In contrast, the 2021 new site (BMD) had one shallow, white-crusted pool with high-pH, and spectra from these crusts showed only calcite in most locations.

At the training site during the 2021 field season, thin white fibers aggregated near the edges and at the bottom of the main rocky pool (WHC2, as described in [145]

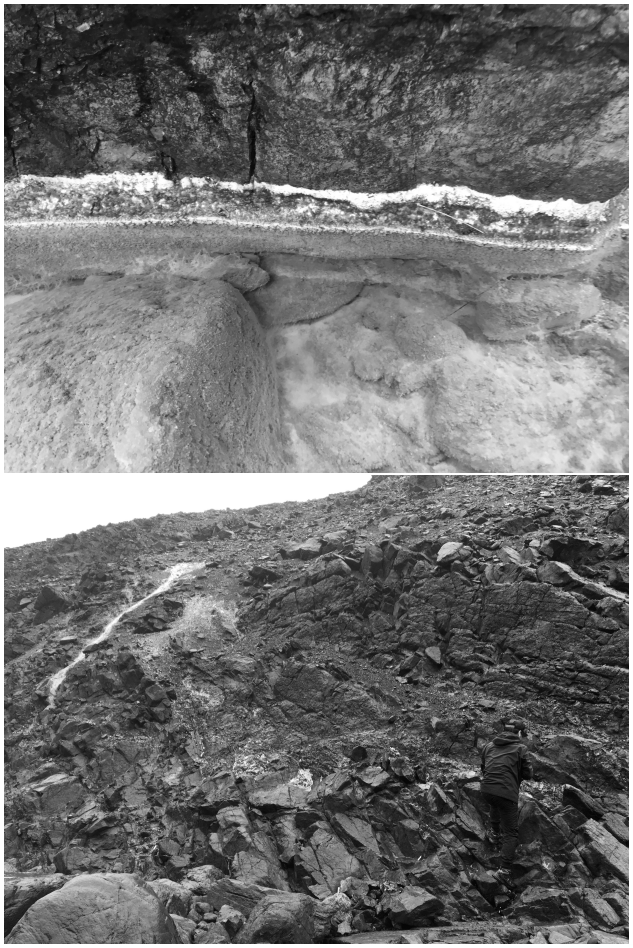

Figure 5.2: Photos of representative high-pH (top) and mid-pH (bottom) locations at BIOC. Top: A high-pH pool from the training site (WHC) with white crusts lining the pool (middle) and white fibers coating the pool bottom. Image width is 30 cm. Bottom: A mid-pH seep from the test site (BMD) has thick white crusts (upper left). A person is shown in the bottom left corner for scale.

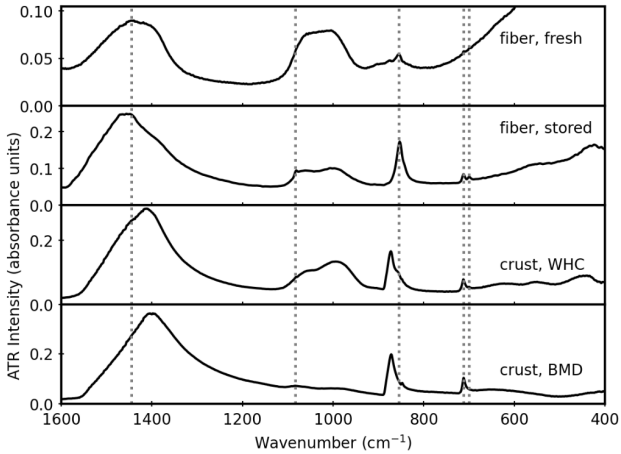

Figure 5.3: Representative MIR spectra of white solids collected in high-pH environments during the 2021 field season. The vertical dotted lines correspond to aragonite peak positions. Aragonite is the predominant carbonate phase in the fibers, while the high-pH crusts can be either mixture of calcite and aragonite (WHC) or entirely calcite (BMD).

and shown in Figure 5.2 top). Sampling these delicate fibers was challenging because they aggregated into a spongy mass, so we collected them in vials with some of their surrounding pool water. As fibers dried at 50 °C over a span of 12 hours, they became crispy and brittle. A portion of the fibers remained stored in their pool water (pH 11).

To better understand the mineral content of the white fibers, we focused on the fingerprint region (400-1600 cm^{-1}) and compared with other control samples, such as serpentine and white laminated crusts that formed around the same pool. Figure 5.3 shows that the fibers have evidence of aragonite, as well as additional peaks that are consistent with peridotite parent minerals (related to Si-O vibrational modes [170]). Fibers were assessed while fresh and after storage in their pool water for eight months. Since there was no detectable change in the peak positions between the dried and stored samples, it suggests that the aragonite formed while in the pool and not during the drying process.

Comparing with the crusts that formed near the pools that contained the white

fibers, Figure 5.3 shows that the crust spectra include similar peridotite-like silica peaks (985 cm^{-1} and 684 cm^{-1}), as well as carbonate peaks. Shifts and shoulders of these carbonate peaks are consistent with a dominant calcite phase, with some aragonite. Overall, we found that the relative proportions of aragonite and calcite in the crust can vary with the sampling location, ranging from almost pure aragonite to pure calcite. We note that the presence of aragonite in the high-pH crusts is correlated with the presence of the fibers in the nearby high-pH pools. For example, when the WHC2 site was sampled in 2009 and 2019, there were no carbonate fibers in the pools and the nearby crusts were entirely calcite. However, during the 2021 WHC2 sampling, there were both carbonate fibers in the pool and aragonite in the nearby crusts.

5.4.2.2 Near mid-pH water

The training site (WHC) and the new site (BMD) each had many locations with white laminated crusts that were not located near high-pH water, but were near wet seepage areas on rocky slopes (Figure 5.2 bottom) or near river banks. These crusts varied greatly in thickness, ranging from cm-thick (TLE, as described in [145]) to mm-thin. White fibrous material was also embedded in some stream banks at WHC.

After initial identification in the field by eye (based on colour), we used HCl to check for fizz that is expected in calcium carbonates. Collected nearby to the white crusts, the control specimens (rocks and sediments) did not fizz in the presence of HCl, suggesting that there is minimal background calcium carbonate.

Back in the laboratory, we used MIR spectra to confirm that the mineralogy of the white crusts is largely calcium carbonate minerals, and that this mineralogy is distinct from the surrounding rocks and sediments (which are predominantly peridotite). Figure 5.4 compares representative spectra for specimens collected from mid-pH areas,

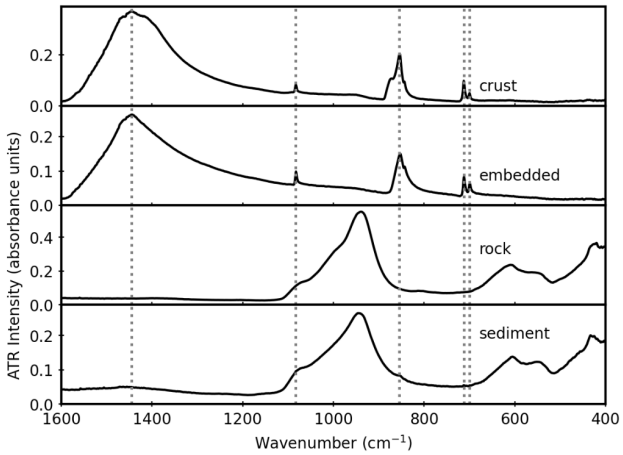

Figure 5.4: Representative MIR spectra of specimens collected near mid-pH environments, including white crusts, embedded white material, dark grey rock, and dark brown sediment. The white crusts ranged from pure aragonite to pure calcite (the spectrum above shows a mixture of both phases), while the embedded white material was entirely aragonite. The control rocks and sediments are predominantly peridotite.

including rocks, sediments, and white crusts. Similar to the high-pH environments (Figure 5.3), we found a much higher prevalence of aragonite in white crusts during the 2021 field season at both the training site (WHC) and the new site (BMD).

5.4.3 Comparison with other sites of serpentinization

The white crusts from BIOC training and new sites show all of the expected MIR spectral features of calcium carbonates, allowing easy differentiation between calcite, aragonite, and other non-carbonate mineral phases. We found extensive aragonite during the 2021 field season, but not in the 2019 field season. Aragonite formed on the top of high-pH pools, in thick white laminated crusts near high-pH pools, in thin white laminated crusts near mid-pH seeps, and embedded in stream banks downstream from high-pH pools. While earlier work at BIOC investigated the aqueous geochemistry in detail [145], ours is the first look into the serpentinization-related carbonate mineral phases at BIOC.

Studies from others demonstrate that site-specific conditions have a complex influence on which carbonate mineral phases form and persist at terrestrial sites of serpentinization [147,171–175]. In general, researchers have determined carbonate phase compositions using powder X-ray diffraction, although some studies used Raman spectroscopy for initial polymorph identification [176,177]. These mineral characterization studies are typically augmented by compositional analyses of nearby water, including ionic content, pH, levels of dissolved inorganic carbon, radiocarbon dating and/or isotopic fractionation assessments.

As an example, The Cedars (California, USA) is a well-studied site with extensive surface carbonates [148]. Recent work [175] provides a detailed investigation of how aragonite and calcite grow in pools at that site. They rely on X-ray diffraction for the phase characterization, corroborating their assignments with crystal habit and elemental content information from scanning electron microscopy with energy dispersive X-ray analyses. Notably, they find that the initial polymorph to crystallize is aragonite, followed by calcite on the underside of the floe as it thickens. The preference of aragonite over calcite in their case is likely controlled by pH and not by high Mg/Ca ratio or high supersaturation.

To assess what can trigger aragonite formation, many studies have correlated the presence (or absence) of aragonite with factors related to the inflow and ionic content of nearby water. At the Ronda peridotites (Spain), the presence of aragonite has been correlated with higher Mg concentrations that are introduced by nearby river water [173]. Similarly, work by [171] at the Samail (Oman) and Ligurian (Italy) ophiolites posit that aragonite precipitation may be favored when high-pH pools come into contact with surface runoff with higher concentrations of Mg ions and/or dissolved inorganic carbon. In more recent work, [172] note that aragonite precipitation at the Samail ophiolites also correlates with less oxygen isotope fractionation.

One consistent observation from many different studies is that, when aragonite does form, it converts to calcite over time. This has been noted at the Samail Ophiolite [172] and The Cedars [175], as well as in hydrothermal carbonate chimneys at depth in the Atlantic Ocean [147]. For example, a detailed investigation at the Samail Ophiolites [172] concludes that aragonite is present at some level in most fresh carbonate deposits, but all older travertine deposits are entirely calcite.

In the case of our BIOC sites, the study of the carbonates is still in its early stages, and we cannot yet explain which factors contribute most to phase selectivity between aragonite and calcite.

5.4.4 Other considerations

When applying IR spectral analyses to sites of serpentinization, critical considerations are (1) the spatial resolution and breadth of area that is sampled, and (2) the spectral resolution and range collected by the instruments. Thus far, we have emphasized the advantages of the MIR spectral range, relative to the SWIR range, for ground-truthed samples. We now discuss how lab-based analyses, including those in the MIR range, offer some additional benefits because of the rugged terrain in our BIOC field site.

For remote sensing, terrestrial satellites such as WorldView-3 have 30-370 cm spatial resolution, depending on the band, and can cover tens of km within one image [151]. The spectral range of the instrument is not continuous, but is instead limited to specific windows in the visible-NIR-SWIR, spanning 15-200 microns in wavelength. The final product is pixelated raster-style data, with each pixel in the image covering an area that is set by the spatial resolution (30-370 cm). Each pixel is associated with an array of numbers that corresponds to the integrated amount of intensity collected in each visible-NIR-SWIR band within that small pixel of area. Since each spectral band spans tens to hundreds of wavelength units, the integrated intensity effectively

WV-3 Satellite	Spatial (m)	Spectral (μm)
Resolution	30-370	0.015-0.200
Range	10,000	0.4-2.5, discrete
Drone	Spatial (m)	Spectral (μm)
Resolution	0.01	0.400
Range	500	0.8-1.1, single band
Laboratory	Spatial (m)	Spectral
Resolution	0.001	1 cm^{-1}
Range	0.001	2.5-25 μm, continuous

Table 5.1: Comparison of WorldView-3 (WV-3) satellite, drone, and laboratory spatial and spectral parameters for infrared data acquisition used in this work.

smears out any spectral features with that range, thereby limiting spectral resolution to the range of the band (15-200 microns of wavelength).

Drone-flown cameras can improve on the spatial resolution (smaller pixel area, typically 1 cm^2) by collecting images closer to ground-level, but they also have a correspondingly smaller spatial range for a single image (typically hundreds of meters). However, IR spectra collected from drones are still limited in the spectral range (integrated intensity bands of 100-1300 microns) due to similar limitations in spectrometer costs and payload weight. In the present work, our drone had an IR camera that covered the NIR range 0.8-1.1 in a single band. Due to the limited spectral range, these data offered limited information and are thus not discussed in this manuscript. A comparison of the IR spatial and spectral parameters for laboratory, drone, WV-3 satellite instruments is provided in Table 5.1.

In the case of our BIOC field site, we used both WorldView-3 and drone images to identify the most likely areas for surface expressions of serpentinization. The steep canyons that host our sites create considerable challenges for analyzing satellite images

due to shadowing effects. Because of the high likelihood for cloud cover in this region of the North Atlantic, as well as the many months of snow cover, it is not often feasible to compare multiple satellite images with the sun location at different angles. Our drone flights were completed during summers when snow cover was not a concern, but the steep grade of the canyon walls still affected where and how low the drone could fly.

For ground-truthed samples, we have the advantages of superior spatial resolution (mm or better), as well as continuous coverage of a large spectral range (SWIR to MIR) with excellent spectral resolution (less than 1 wavenumber). The obvious disadvantage is that we cannot leverage these benefits as easily to survey large areas to screen for serpentine-hosted springs. However, many lab-based IR spectrometers are portable with a small footprint, and thus can be used at basecamps or where there is access to an AC generator. This means that using spectral analyses during a field campaign can help direct and adapt sampling strategies during the field work. All in all, smaller geological features – such as our carbonate crusts – will be easier to characterize with the MIR spectra.

With regard to lab-based analyses, it is also worth emphasizing that MIR spectra are very useful for augmenting other common mineral analyses. The ATR measurements we use here require only a few mg of powdered sample, and other modes of measurements require even less sample. For example, including the transmission geometry for IR (transmission IR technique) uses only tens of micrograms of sample that is diluted with an IR-transparent binder such as potassium bromide. IR spectra are also well-suited to characterizing amorphous and poorly crystalline phases, unlike powder X-ray diffraction. The peak information that IR spectra provide is complementary to Raman spectra, which is a different kind of vibrational spectroscopy. IR is much more sensitive to water than Raman, which can either be helpful or a hindrance,

depending on the situation. However, IR is not susceptible to fluorescence interference which can debilitate Raman spectral analyses that involve even small amounts of fluorescent organic material or Fe-bearing minerals, both of which are challenges for serpentinization-relevant minerals.

5.5 Conclusions

We demonstrate that lab-based MIR spectra of ground-truthed samples can offer different and valuable information that complements SWIR data that are relevant for remote-sensing. Specifically, we show the evidence for differences – and annual changes – in the type of calcium carbonate polymorph that forms as surface expressions of subsurface serpentinization at the Bay of Islands Ophiolite Complex (Newfoundland & Labrador, Canada). Our results highlight value of MIR spectroscopy for understanding more about terrestrial-based serpentinization processes.

5.6 Supporting information

This section is related to Chapter 5, but is not intended to be submitted to a journal.

5.6.1 Serpentinization

Serpentinization is a series of reactions between groundwater and minerals in ultramafic rocks. The ultramafic rock, such as olivine (Fe_2SiO_4, Mg_2SiO_4) reacts with groundwater, producing serpentine ($Mg_3Si_2O_5(OH)_4$) and hydroxide ($Mg(OH)_2$, $Fe(OH)_2$), making a high pH local environment. If the local geological setting contains calcium-rich minerals, such as pyroxene ($CaMgSi_2O_6$), the release of calcium ions also accompanies the formation of serpentine. The following serpentinization

reactions can support microbial life by providing energy (production of H_2) and a carbon source (abiotic organics CH_4). Serpentinization occurs in mid-ocean ridges or ophiolites on Earth, as evidenced by local alkaline water environments (pH 11-12). On Mars, serpentinization is thought to have occurred in the subsurface. Therefore, it is significant to develop methods to locate subsurface serpentinization to explore whether there is extinct/extant life on Mars. Here is the equations of serpentinization reaction mentioned above (Equation 5.1, Equation 5.2, Equation 5.3, Equation 5.4).

$$Fe_2SiO_{4(s)} + 5Mg_2SiO_{4(s)} + 9H_2O_{(l)} \rightarrow 3Mg_3Si_2O_5(OH)_{4(s)} + Mg(OH)_{2(s)} + 2Fe(OH)_{2(s)} \tag{5.1}$$

$$4Mg_2SiO_{4(s)} + CaMgSi_2O_{6(s)} + 7H_2O_{(l)} \rightarrow 3Mg_3Si_2O_5(OH)_{4(s)} + Ca^{2+}_{(aq)} + 2OH^-_{(aq)} \tag{5.2}$$

$$6Fe(OH)_{2(s)} \rightarrow 2Fe_3O_{4(s)} + 2H_{2(g)} + 4H_2O_{(l)} \tag{5.3}$$

$$4H_{2(g)} + CO_{2(g)} \rightarrow 2H_2O_{(l)} + CH_{4(g)} \tag{5.4}$$

The serpentine weathering contains the release of magnesium (Mg) and silicon (Si) during the dissolution [178], lacking the essential plant nutrients such as potassium, nitrogen, and phosphorus element [179]. Therefore, the plants that grew around the serpentine soil are distinctive and have low growth productivity [180]. Moreover, some bio-organism in the vicinity would accelerate the serpentine weathering process, releasing a large amount of Mg, Si, and Ca components [179, 181]. The released Mg and Ca further form carbonate minerals when in contact with atmosphere CO_2.

Therefore, detecting carbonate features is one method to locate serpentinization. The reactions of serpentine weathering and carbonate formation are shown in Equation 5.5, Equation 5.6 and Equation 5.7

$$Mg_3Si_2O_5(OH)_{4(s)} + 6H^+_{(aq)} \rightarrow 3Mg^{2+}_{(aq)} + 2H_4SiO_{4(s)} + H_2O_{(l)} \tag{5.5}$$

$$Mg^{2+}_{(aq)} + H_2O_{(l)} + CO_{2(g)} \rightarrow MgCO_{3(s)} + 2H^+_{(aq)} \tag{5.6}$$

$$Ca^{2+}_{(aq)} + 2OH^-_{(aq)} + CO_{2(g)} \rightarrow CaCO_{3(s)} + H_2O_{(l)} \tag{5.7}$$

5.6.2 More details about field research

Three methods can be considered to locate serpentinization. One is to detect carbonate features. A serpentinization spring (alkaline environment) discharged to the ground surface comes in contact with atmosphere CO_2, forming carbonate precipitate around the serpentine rocks. The second characteristic is the release of hydrogen and methane in the serpentinization reaction. The third method is detecting the temperature of the serpentinization spring since the reaction is exothermic, causing warmer spring water than the surrounding water. Visible to infrared optical spectroscopy is widely used for rapid analyzing mineral composition. In this project, remote sensing (space-based satellite or drone) with either visible or thermal (near-IR) spectral analysis was used to locate the known or potential serpentinization location. My job in this project is to arrive at expected sites and collect samples based on the results from remote sensing, followed by identifying the mineral samples with field-based Mid-IR or Near-IR characterization.

This project contains two parts chronologically. The first field research was con-

ducted in 2019 at the Winterhouse Canyon (WHC) in the Tablelands. Previous research has well investigated the geochemical study of this area. Our job in this field work is to calibrate the remote sensing and lab-based IR analysis to confirm the wavelength region or specific IR features used to identify the mineral. In 2021, the second field trip was located in Blow Me Down Massif, where the serpentine feature was not explored. We chose some promising serpentinization spring sites based on remote sensing data. My job in this field of research was to collect samples in the chosen sites and use IR to check the mineral phase, to confirm the accuracy of remote sensing results.

5.6.3 Additional discussion

Although serpentinization would both release Mg and Ca during the dissolution, It has been demonstrated that serpentine-affected soil obtains a larger amount of Mg than Ca [182]. Therefore, it is reasonable to find some natural inorganic or complex compounds in which Mg is present, such as magnesite ($MgCO_3$) or struvite (($MgNH_4PO_4{\cdot}6H_2O$)) [183]. However, our IR results of carbonated minerals show only the calcium carbonate phase, without any characteristic magnesium carbonate. In addition, the effect of Mg was also considered in carbonate synthesis in my laboratory work (Chapter 2). Even though my experiments did not take into account all Mg:Ca ratios and did not simulate the temperature and pH of the serpentine spring, no magnesite was found even when the Mg:Ca reached 3:1 (Figure 2.6).

It is known that the addition of Mg ions favors aragonite formation during the calcium carbonate formation [184–186], evidenced by both our synthetic and natural samples. Such phenomenon is also seen in marine biological minerals, such as nacre of seashell and sea-urchin skeletons, which are composed mainly of aragonite rather than calcite due to their high Mg content [187]. Serpentine has a local environment

with significant Mg release, resulting in a high Mg:Ca ratio. Therefore, the emergence of aragonite as a carbonate mineral is not surprising.

The local pH is another factor that influences the phases of carbonate minerals. Others [188] demonstrated that high pH conditions could be beneficial for pre-aragonite ACC, followed by crystallization. Therefore, the alkaline environment of the serpentine spring may favor the aragonite formation. As for the calcite phase identified in mineral samples, its formation may originate from the phase transition of the aragonite phase (dissolution-recrystallization). However, the time scale for the phase transition remains unknown.

Overall, the serpentine alters the ionic and pH conditions of its surrounding environment, causing the formation of aragonite or calcite. Factors such as ion content (Mg:Ca ratio), pH, or temperature plays essential roles in salt formation but will not tell the whole story. The natural situation is too complicated to explain the mineral formation thoroughly and beyond the scope of this thesis. However, these special serpentine features, such as carbonate minerals, help us use visible or infrared techniques to locate the serpentine sites accurately.

Chapter 6

Conclusion

6.1 Summary of thesis work

This thesis work studied the calcium carbonate ($CaCO_3$) polymorphism and phase conversion under different conditions. We first described two different dissolution-recrystallization scenarios by considering the phase of initial calcium carbonate particles. As the single-phase aragonite powders are immersed in water, very limited phase conversion is observed, making the aragonite phase persist for much longer. However, if aragonite and calcite are deposited together, whether as a physical mixture of powders or as a mixed-phase annealed sample, any exposure to water could accelerate the rate of aragonite-calcite phase conversion, making the mixed phase eventually become a single-phase suspension of calcite. This suggests that faster and more complete aragonite dissolution should be considered whenever calcite is in contact with both water and aragonite.

Orthophosphate and polyphosphate (SHMP) exhibit different behaviors when interacting with $CaCO_3$ particles in aqueous solution. At the same concentration (mM range), the ATR-FTIR data showed an apparent phosphate secondary phase after

orthophosphate exposure. However, no such secondary phase was formed during polyphosphate treatment, suggesting low phosphate uptake. The solid-state NMR data showed that the phosphate exists as different speciations of SHMP hydrolysis products. I also saw the evidence that PO_4 adsorption is aided by the concomitant $CaCO_3$ dissolution-recrystallization process. It is also confirmed that $CaCO_3$ particles close to P-species are only a tiny fraction of the bulk, minute surface dissolution-recrystallization and phosphate intercalation. More importantly, such dispersed phosphate adsorption stabilizes aragonite against dissolution-recrystallization (phase conversion) even in aragonite-calcite mixed phase suspension. Meanwhile, the adsorbed phosphate entities improve the thermal stability of aragonite, helping against the phase conversion at high temperatures (annealing).

The field research work provided another way to observe and infer the dissolution and recrystallization of $CaCO_3$ from naturally occurring minerals. I used ATR-FTIR to detect the mineral samples collected in serpentine sites and found that there were pure calcite, pure aragonite, and aragonite-calcite mixed phases. The mixture of phases suggests that the local geological setting of serpentinization (Mg^{2+}, high pH) could cause the crystallization of aragonite, similar to what I found in my laboratory syntheses. By comparing with other studies [175], the aragonite seems to point to a fresher carbonate deposit, and the calcite phase may come from the phase conversion from aragonite. Complex natural conditions make the timescale for geological $CaCO_3$ crystallization and phase conversion very different from timescales I observed in laboratory studies. However, geological studies by others have worked to assess the timescales by using radiocarbon dating and stable isotope analyses [172].

6.2 Implication and future work

6.2.1 Relevance for ocean acidification

In this work, I discussed the calcite-aragonite mixture system, studying the time evolution of the "pumping effect" that is based on aragonite dissolution and its recrystallization as calcite. The implications for my findings could be profound. Sulpis *et al.* recently posit that the aragonite dissolution boosts the carbonate ion content in seawater to neutralize the ocean acidification in a way that protects calcite mineral from dissolution [3]. My studies describe earlier stages of the dissolution/recrystallization process. In addition, the mixed-phase system resulted in significant changes in aragonite "sacrifice" rates in solution, which need to be considered more when modeling ocean acidification.

For future work, the study of $CaCO_3$ dissolution-recrystallization in an ocean environment is of great interest. To mimic seawater, the solution composition, pH, salinity, and temperature must be considered. Each factor would have an important effect on $CaCO_3$ phase conversion. Moreover, the distance between aragonite and calcite crystals in mixed-phase suspension may influence the kinetics of phase conversion. In other words, I want to know the distance limit that the aragonite's dissolved ions (Ca^{2+}, CO_3^{2-}) can diffuse to create a supersaturated condition in terms of the calcite. To achieve this goal, I would like to synthesize one large aragonite single crystal and calcite powders. Therefore, it is possible to observe changes in aragonite dissolution rates as I adjust the distance between aragonite single crystals and calcite powders.

6.2.2 Relevance for industry processes

In industrial applications, nano-sized $CaCO_3$ is often used as additives (fillers) in materials such as plastics, cement, and rubber [6, 8, 189]. In addition to calcite, the

synthesis of other phase, such as aragonite, has also received much attention due to their distinctive physical and chemical properties [95]. Therefore, the stability of calcium carbonate phases, especially in humid or aqueous environments, is critical.

Phosphate is an important chemical modifier that can disperse calcium carbonate particles against particle aggregation [20, 119]. Moreover, according to our research results, the introduction of polyphosphate also protects calcium carbonate from phase transformation, which will be more conducive to apply calcium carbonate materials in industry.

Appendix A

Additional field research data

This is an appendix of Chapter 5, showing a field research report in order to give a better sense of what kinds of analyses are required and how many measurements are needed, so as to study the geological setting of serpentine and carbonate minerals.

A.1 All Experimental details

Infrared (IR) spectroscopy is used to identify phases of minerals. Each vibrational motion of atoms in a solid requires a specific amount of energy to excite it. The infrared frequency range of electromagnetic radiation matches the energy required for these vibrations. IR energy absorption occurs when vibrations that change the dipole moment occur.

A.1.1 Attenuated total reflectance-fourier transform infrared spectroscopy (ATR-FTIR)

Attenuated total reflectance-infrared spectroscopy (ATR-IR) is an internal reflection technique in which samples absorbed evanescent waves when the IR incident beam

experience total internal reflection at the interface. ATR-FTIR usually measure solid powders, which means that some powders needs to be collected from rock samples.

Fine powders were scraped from the rock samples and pressed against the ATR crystal to ensure tight contact. Spectra spanned the mid-IR range (400-4000 cm^{-1}), with a resolution 2 cm^{-1}.

A.1.2 External reflection techniques

In addition to ATR, external reflection techniques have also been used to perform IR analysis. External reflection techniques detect the beam reflected from the sample surface and generally produce two reflection conditions: diffuse and specular reflection.

A.1.2.1 Specular reflectance

The specular reflection technique is a method to measure the specular reflection energy of the sample surface, which is based on the principle that the angle of the incident beam is equal to the angle of the reflected beam. Therefore, this technique measures samples with a reflective surface or thin film attached to a reflective substrate.

A.1.2.2 Diffuse reflectance

The technique relies on diffusely scattered light when the spectrometer beam illuminates the sample. The incident IR beam penetrates the solid, causes beam scattering, and returns to the surface as a diffused beam. The deeper beam penetration, the stronger beam scattering produces more diffuse reflection, thus achieving the desired spectral band shape and peak intensity.

A.1.2.3 Contactless FTIR analyzer

For naturally formed rock samples, the appearance of their rock surface is valuable, with a unique texture or color. To better understand the surface chemistry of rocks, it is necessary to perform IR operations without damaging the rock surface. One type of FTIR spectroscopy has a front reflection module, which helps to detect the intact sample in a contactless and non-destructive manner. Two methods were used for this analysis. First, the bulk sample was directly detected by placing the sample surface at the IR window. Another way was to collect some powders from the rock surface and mix them with potassium bromide (KBr) to make a pellet, then place it at the IR window and analyze it.

A.1.3 Near IR spectroscopy

Near-IR spectroscopy measures the overtone and combination bands with higher frequency modes. The Near-IR range is typically between 4000 and 12500 cm $^{-1}$ (0.8 to 2.5 μm). The transition of the higher vibrational state is much less likely and weaker in intensity than the fundamental state, resulting in a broader IR peak. The Near-IR data collection was completed at Memorial using a TerraSpec 2 Near Infrared - Shortwave Infrared (NIR-SWIR) Spectrometer (in the lab of Dr. Stephen Piercey), based on a diffuse reflectance geometry and using suitable a white reflection standard for calibration.

A.2 2019 field trip results

In 2019, we collected samples at Winterhouse Canyon (WHC) in the Tablelands, Newfoundland and Labrador, Canada. The field research team members have studied the serpentine's geological features in this area [145].

A.2.1 ATR-IR results

In Mid-IR (MIR) analysis, the fingerprint region, from 400 to 1500 cm^{-1}, is best for sample identification. Therefore, the IR bands shown in the fingerprint region drew much attention for sample identification.

A.2.1.1 Control samples

Serpentine and control group: Typical serpentine-like rocks were selected for IR analysis, and their surface color varied from light green and dark green to yellow. As shown in the IR spectra (Figure A.1 Left), all these samples indicate serpentine as the dominant phase with a peak at 950 cm^{-1} and double peaks at 610 cm^{-1} and 550 cm^{-1}. The small peak at 1650 cm^{-1} may indicate a water vibration.

We also randomly collected mud or small stones in the field as a control group. From the IR spectrum (Figure A.1 Right), the strong peak at 940 cm^{-1} and the double peak at 610 cm^{-1} and 550 cm^{-1} indicate serpentine. Based on the sites where we collected the sample, these locations were relatively wet. Therefore, the ultramafic minerals may have been serpentinized, with prominent water features shown in the IR (broad peak at 3500 cm^{-1} and a small peak at 1650 cm^{-1} in Figure A.1).

A.2.1.2 Calcium carbonates

Calcite group: The IR spectrum of some samples confirms calcite as the dominant phase, with three absorbance peaks (1500 cm^{-1}, 872 cm^{-1} and 712 cm^{-1}) reflecting the vibration within the carbonate moiety of calcite (Figure A.2 Left). In addition, no matter the texture of the sample surface (rough or shiny), there is no difference in the carbonate phase.

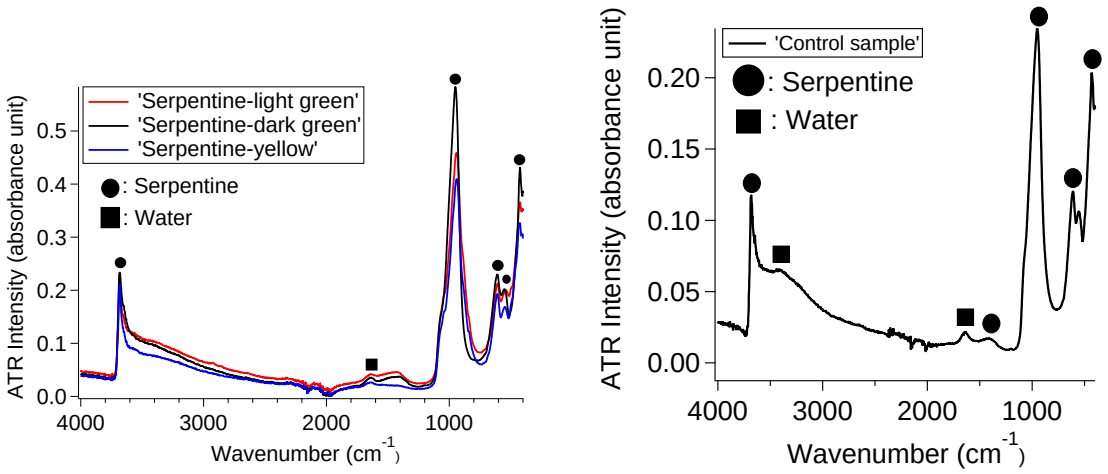

Figure A.1: Representative ATR-FTIR of Left: serpentine mineral. Right: control sample

A.2.1.3 Serpentine with carbonate mixture

Serpentine with calcite mixture group: Many samples were collected from the outcrop of the spring at various locations. The ATR analysis (Figure A.2 Right) shows a calcite and serpentine mixture. The serpentine phase marked in the spectra could also be peridotite, which is reasonable because peridotite is a dominant rock in the upper part of the Earth's mantle. In addition, serpentine minerals can form when peridotite is hydrated at low temperatures.

A.2.2 Near-IR results

The Near-IR (NIR) data for our field samples is valuable because it helps bridge between the lower-energy mid-IR (MIR) data that we can collected during field work with the higher-energy shortwave-IR (SWIR) data that the satellites can provide. The mineral assignments we were able to make from the NIR data were largely consistent with those we had assigned based on the Mid-IR (MIR) data. Overall, both MIR and NIR showed slightly different IR features between rough and shiny parts. Based on our NIR and MIR data, we now attribute the shiny appearance to the presence of

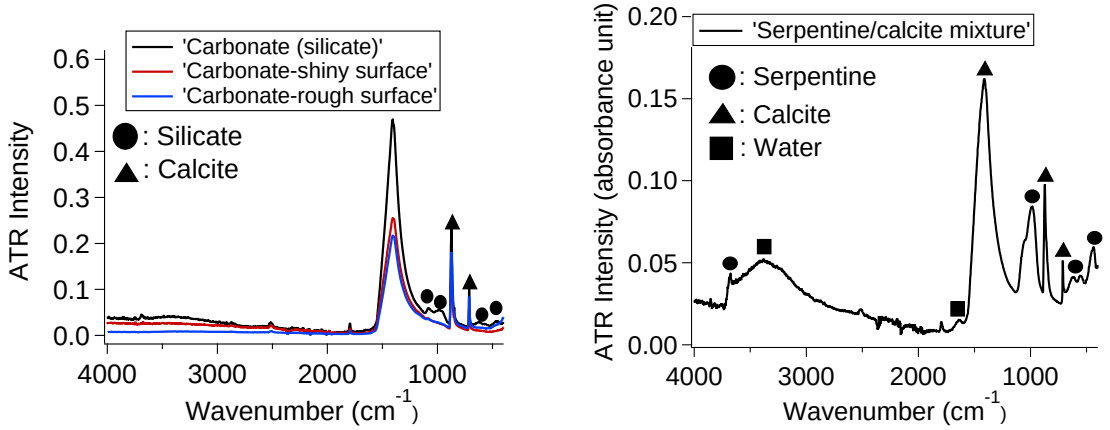

Figure A.2: Representative ATR-FTIR of Left: calcite mineral. Right: mixture of calcite and serpentine

different minority phases.

For serpentine (Figure A.3 Left), there were typical serpentine spectral features, including a doublet peak at 2.10 and 2.13 μm as well as other peaks related to Mg–OH and OH. There are some variations in relative peak intensities that we correlate with the sample surface color and texture. The absorbance peaks at 1.38 μm represent the Mg/Fe–OH stretching overtone, and an asymmetric Mg/Fe–OH combination mode appears near 2.32 μm. The doublet at 2.10 and 2.13 μm, although not very clear, helps to distinguish the serpentine phase. The combination of OH stretching and OH bending at 1.9 μm suggests adsorbed water, which is typical of serpentine. Additional peaks are related to Fe oxidation states in serpentine. The peak at 0.45 μm generally relates to a spin-forbidden electronic transition of Fe^{3+}. A peak at 0.75 μm is related to Fe^{2+}/Fe^{3+} intervalence charge transfer. Small spectral bumps near 0.92 μm likely relate to Fe^{2+} electronic transitions.

For calcite (Figure A.3 Right), NIR peaks were visible at 2.3 and 2.5 μm due to the combination and overtone bands of the CO_3 fundamentals. There are also OH combination bands at 1.4 and 1.75 μm related to stretching and bending. Even though there is no OH in the calcite structure itself, these bands are commonly associated with

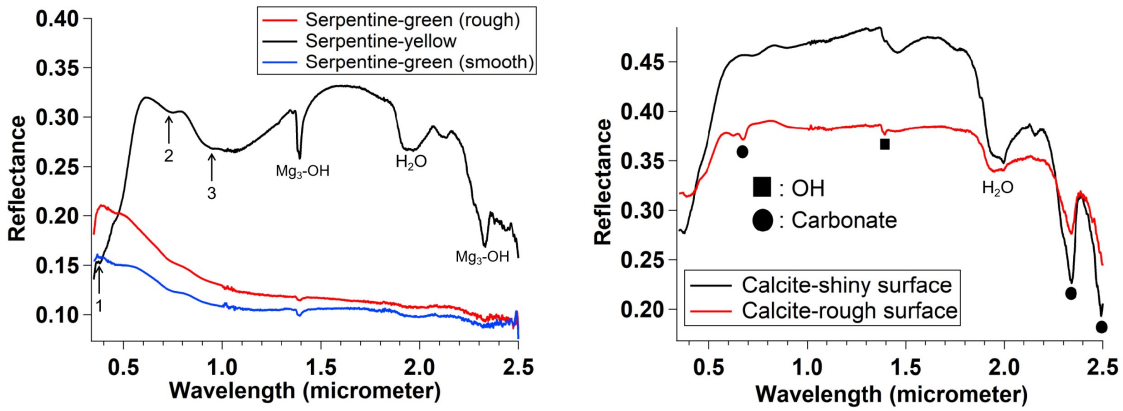

Figure A.3: Near-IR of Left: serpentine, Right: calcite

other associated minerals. We noticed that the shiny part of samples had sharper OH peaks than the rough part, so there might be other minerals that contain structural water in the shiny surface. We also saw additional doublet peaks around 0.7 μm for calcite samples with the rough surface; the origin of this peak is not yet clear and is under further investigation by us.

In summary, we have confirmed NIR regions that are distinct between serpentine and calcite. In the regions of interest of the eight different SWIR bands of WorldView3 satellite, the calcite has less absorbance (more reflection) than the peroditite. These differences will be helpful in prescreening the satellite and drone spectral data.

A.2.3 Contactless FTIR results

As mentioned above, each sample has a different surface appearance for both calcite and serpentine samples. To better understand the surface chemistry of each sample, it is necessary to operate an IR technique without damaging the surface. Therefore, we used a contactless reflectance FTIR analyzer to identify the surface chemistry. We converted the wavenumber unit to the wavelength unit in the IR spectrum (Figure A.4). Overall, unlike near IR, we did not get too many peaks under 2.5 μm, and

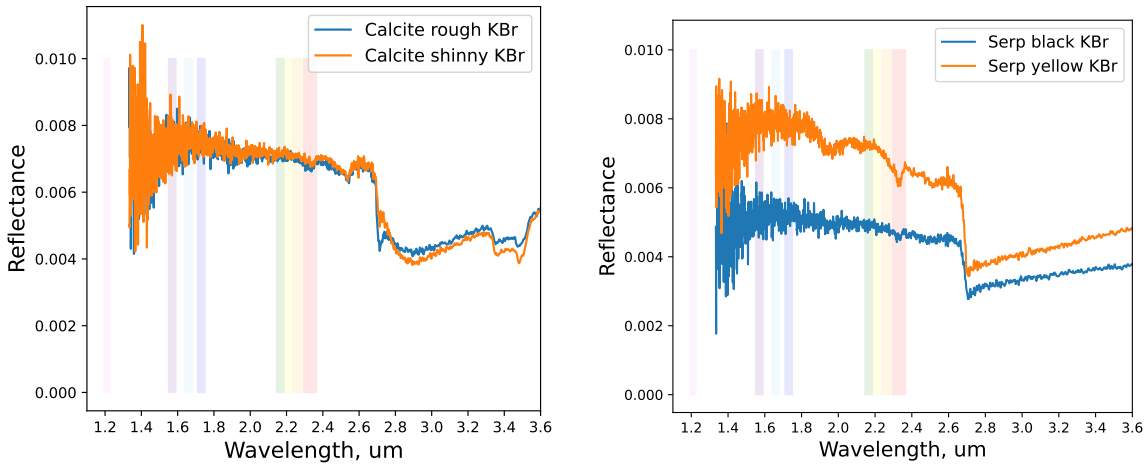

Figure A.4: Contactless IR spectra of Left: calcite sample, Right: Serpentine sample. The colored bands in the spectra indicate the position of eight SWIR bands of the WorldView3 satellite.

an even worse detection limit under 1.8 μm, barely seeing anything but noise in the spectrum.

The contactless IR spectrum of rough and shiny calcite parts was shown in Figure A.4 (Left). Like Near-IR (NIR), the peak at 2.3 μm is due to the combination and overtone bands of the CO_3. The peaks in between 2.4 μm to 2.8 μm (around 4000 cm^{-1} are unknowns, since the fingerprint (400 cm^{-1}-1500 cm^{-1}) is the most recognizable region for phase judgment. For serpentine (Figure A.4 Right), the peak at 2.32 μm stands for asymmetric Mg–OH combination tone, and the peak at 1.9 μm represents the combination of OH stretching and OH bending. Both peaks are also seen in the near IR spectrum. However, such peaks are not found on the black serpentine surface, which probably means different chemical phases.

A.3 2021 field trip results

Based on the satallite and drone images, we found potential sites in Blow Me Down provincial park (Newfoundland and Labrador, Canada.) that might contains serpen-

tinized springs with carbonated minerals exposed on the ground. Our job is to arrive in these sites physically, collecting samples and IR identification, to check the accuracy of satellite and drone results. We describe results from 4 different areas. Each area has an informal name that our research team uses to identify it: the Matt site, the Penny site, the Pie site, and Winterhouse Canyon (WHC).

A.3.1 Matt Site

The Matt site is where a potential serpentinized spring occurred or is occurring down a deep slope; many white precipitants were exposed along the massif. As seen in Figure A.5 (top), the control minerals show a serpentine phase, with one peak at 1370 cm^{-1} suggesting peridotite.

The white precipitates on the serpentine minerals were collected in multiple positions. From the ATR-FTIR (Figure A.5 bottom left), we first confirmed calcium carbonate as the main component in the white precipitates. Some small peaks at 985 cm^{-1} and 684 cm^{-1} may indicate the silicate from serpentine. However, two different calcium carbonate polymorphs, calcite, and aragonite were observed. Some of the white samples suggest a mixture of calcite and aragonite, by identifying the ν_2 IR peak position, with peak at 872 cm^{-1} and 854 cm^{-1} representing calcite and aragonite, respectively (Figure A.5 bottom right).

It is known that aragonite is less stable than calcite thermodynamically. The mineral dissolution and recrystallization cause aragonite to convert to calcite eventually. Based on my lab work, if aragonite and calcite coexist in the aqueous solution, the aragonite would recrystallize to calcite in a short period (one-week). We don't know how long is needed for aragonite to transform to calcite in geological environments, maybe a few days or a few years.

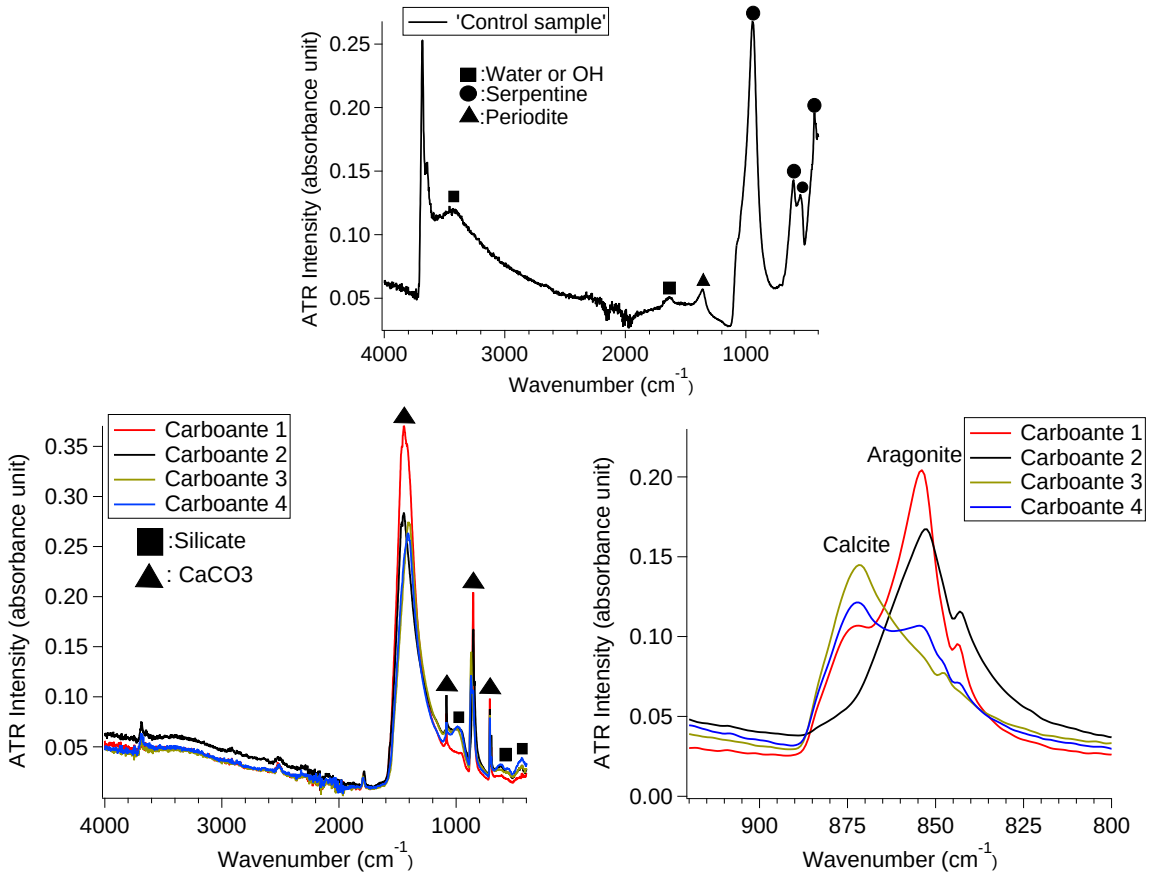

Figure A.5: Top plot: ATR of serpentine mineral in Matt site. Bottom left: ATR of calcium carbonate in Matt site. Bottom right: Emphasizing the ATR ν_2 peak of calcium carbonate.

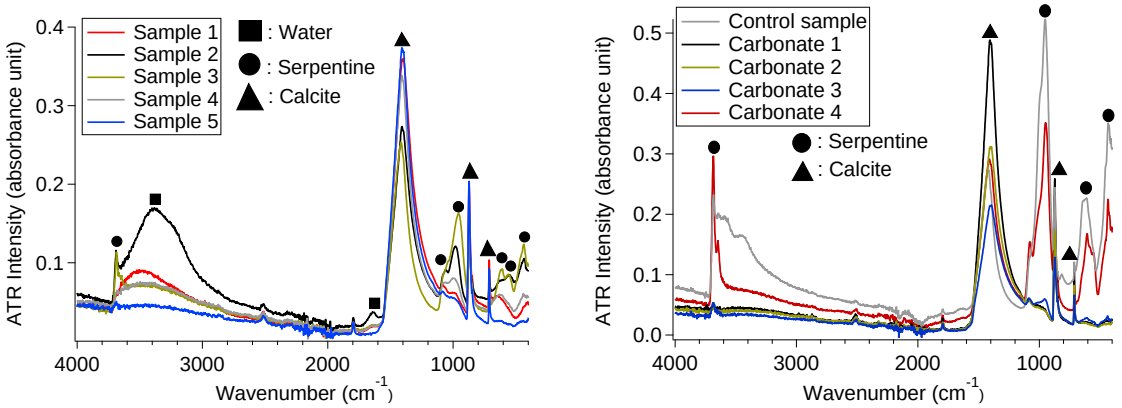

Figure A.6: Left plot: ATR of samples collected at the Penny site. Right Plot: ATR of samples collected in Pie site.

A.3.2 Penny Site

Two active alkaline springs were found at this site, suggesting the serpentinization reaction. The carbonate sediments may form when atmospheric CO_2 reacts with alkaline water. We indeed observed white precipitate exposed on the ground, so IR analysis was conducted. Samples were collected at multiple positions: far away from active spring - near active spring - pool below. From the IR results (Figure A.6 Left), we confirmed calcium carbonate precipitate in all positions, only calcite. Some of the samples also contain serpentine and water.

A.3.3 Pie site

This is the area where active alkaline pools were also found. Some of the samples were collected along the stream. Overall, all the white carbonate samples around the alkaline pools are confirmed as calcite phase (Figure A.6 Right). The control sample collected near alkaline pools has a serpentine phase (Figure A.6 Right).

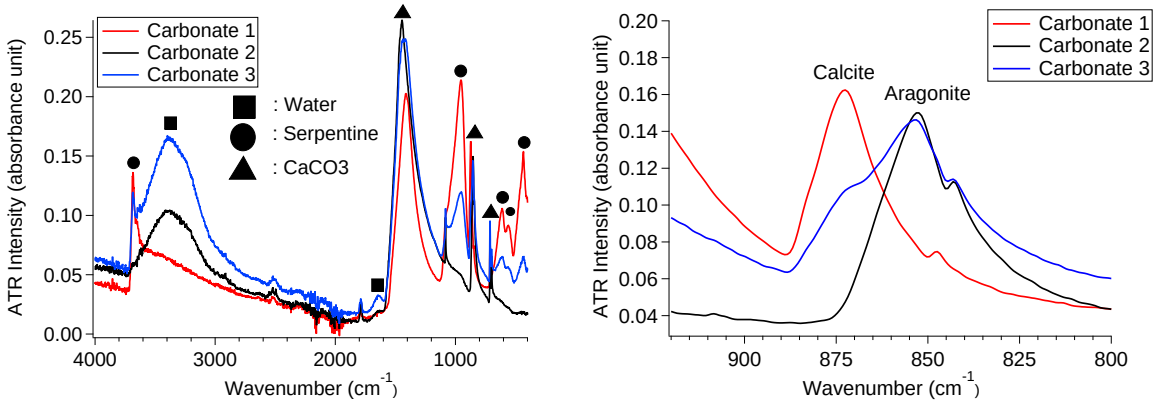

Figure A.7: Left plot: ATR of carbonate mineral at the WHC site. Right plot: Emphasizing the ATR ν_2 peak of carbonate mineral from WHC.

A.3.4 WHC (aragonite)

This is where we found aragonite in 2019 field research. Two years later (from 2019 to 2021), the white precipitate sediment feature in this location was doubled in length. We confirmed the samples collected in this area to include both calcite and aragonite (Figure A.7).

A.3.5 WHC (ACC)

This is where we found crispy fibers sitting in the pool (Figure A.8 Top), and we also collected some white laminated pieces around the pool (Figure A.8 Bottom). The IR of the original and relatively dry fibers are still dominated by the water (black and blue curve in Figure A.8 Top left). As the fiber sample dries, some broad peaks appear in the fingerprint region, whose position matches ACC (yellow and grey curve in Figure A.8). Compared to the ACC standard (red curve in Figure A.8), a doublet peak occurs at ν_2 position of dried fibers (Figure A.8 Top right), probably representing pre-aragonite and pre-calcite ACC. Another piece of evidence for local geological features is the laminated pieces collected around the pool. The infrared spectrum shows the dominant phase of calcite, further confirming the carbonate environment

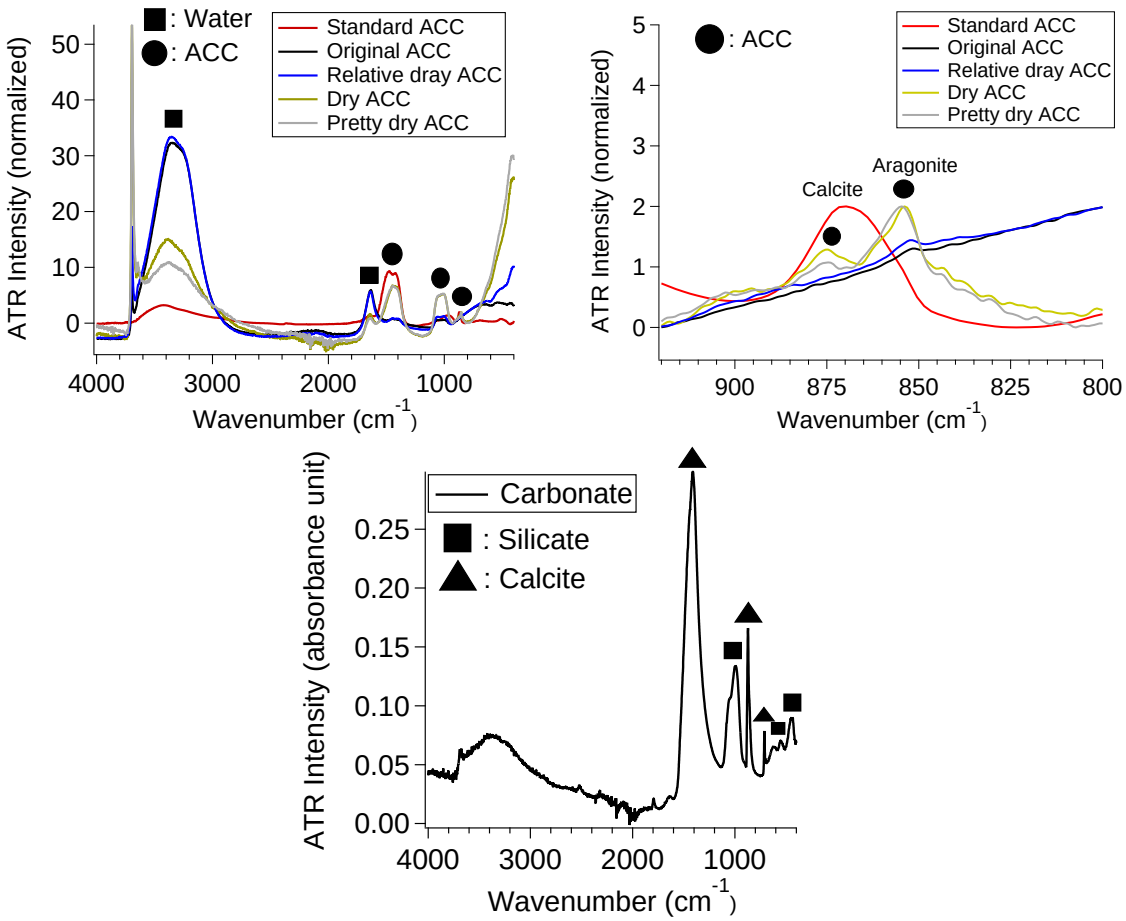

Figure A.8: ATR of samples collected in WHC (ACC) site. Top left: full spectrum. Top right: magnified spectrum (400 cm^{-1}-1600 cm^{-1}). Bottom: full spectrum of white laminated pieces around the pool.

(Figure A.8 bottom).

Bibliography

[1] Kimmel Center for Archaeological Science (Weizmann Institute of Science). Infrared standards library, 2021.

[2] J. Perić, M. Vučak, R. Krstulović, Lj. Brečević, and D. Kralj. Phase transformation of calcium carbonate polymorphs. *Thermochim. Acta*, 277:175–186, 1996.

[3] O. Sulpis, P. Agrawal, M. Wolthers, G. Munhoven, M. Walker, and J. J. Middelburg. Aragonite dissolution protects calcite at the seafloor. *Nat. Commun*, 13:1–8, 2022.

[4] R. Chang, S. Kim, S. Lee, S. Choi, M. Kim, and Y. Park. Calcium carbonate precipitation for CO_2 storage and utilization: A review of the carbonate crystallization and polymorphism. *Front. Energy Res*, 5:1–12, 2017.

[5] C. A. Moras, L. T. Bach, T. Cyronak, R. Joannes-Boyau, and K. G. Schulz. Ocean alkalinity enhancement-avoiding runaway $CaCO_3$ precipitation during quick and hydrated lime dissolution. *Biogeosciences*, 19:3537–3557, 2022.

[6] X. Liu, L. Chen, A. Liu, and X. Wang. Effect of nano-$CaCO_3$ on properties of cement paste. *Energy Procedia*, 16:991–996, 2012.

[7] Z. Hu, X. Zen, J. Gong, and Y. Deng. Water resistance improvement of paper by superhydrophobic modification with microsized $CaCO_3$ and fatty acid coating. *Colloids Surf. A Physicochem. Eng. Asp*, 351(1-3):65–70, 2009.

[8] Y. D. Zhu, G. C. Allen, P. G. Jones, J. M. Adams, D. I. Gittins, P. J. Heard, and D. R. Skuse. Dispersion characterisation of $CaCO_3$ particles in PP/$CaCO_3$ composites. *Compos. Part A Appl. Sci. Manuf*, 60:38–43, 2014.

[9] T. Nypelö, M. Österberg, and J. Laine. Tailoring surface properties of paper using nanosized precipitated calcium carbonate particles. *ACS Appl. Mater. Interfaces*, 3(9):3725–3731, 2011.

[10] A. S. Kamba, M. Ismail, T. A. T. Ibrahim, and Z. A. B. Zakaria. Biocompatibility of bio based calcium carbonate nanocrystals aragonite polymorph on NIH 3T3 fibroblast cell line. *Afr. J. Tradit. Complement. Altern. Med*, 11:31–38, 2014.

[11] S. M. Dizaj, M. Barzegar-Jalali, M. H. Zarrintan, K. Adibkia, and F. Lotfipour. Calcium carbonate nanoparticles as cancer drug delivery system. *Expert Opin. Drug Deliv*, 12:1649–1660, 2015.

[12] M. Iijima, J. Yasumoto, A. Iguchi, K. Koiso, S. Ushigome, N. Nakajima, Y. Kunieda, T. Nakamura, K. Sakai, M. Yasumoto-Hirose, et al. Phosphate bound to calcareous sediments hampers skeletal development of juvenile coral. *R. Soc. Open Sci*, 8(3):1–7, 2021.

[13] M. Alberic, E. N. Caspi, M. Bennet, W. Ajili, N. Nassif, Thierry A., A. Berner, P. Fratzl, E. Zolotoyabko, L. Bertinetti, et al. Interplay between calcite, amorphous calcium carbonate, and intracrystalline organics in sea urchin skeletal elements. *Cryst. Growth Des*, 18(4):2189–2201, 2018.

[14] Y. B. Hu, M. Wolthers, D. A. Wolf-Gladrow, and G. Nehrke. Effect of pH and phosphate on calcium carbonate polymorphs precipitated at near-freezing temperature. *Cryst. Growth Des*, 15:1596–1601, 2015.

[15] S. Tadier, S. Rokidi, C. Rey, C. Combes, and P. G. Koutsoukos. Crystal growth of aragonite in the presence of phosphate. *J. Cryst. Growth*, 458:44–52, 2017.

[16] W. Xia and J. Chang. Well-ordered mesoporous bioactive glasses (MBG): A promising bioactive drug delivery system. *J. Control Release*, 110(3):522–530, 2006.

[17] Y. Lei, S. Narsing, M. Saakes, R. D. Van Der Weijden, and C. J. N. Buisman. Calcium carbonate packed electrochemical precipitation column: new concept of phosphate removal and recovery. *Environ. Sci. Technol*, 53(18):10774–10780, 2019.

[18] R. Kumar and P. Pal. Assessing the feasibility of N and P recovery by struvite precipitation from nutrient-rich wastewater: a review. *Environ. Sci. Pollut. Res*, 22(22):17453–17464, 2015.

[19] T. Nakatsuka, H. Kawasaki, and S. Yamashita. End group effects in polymer modification of calcium carbonate fillers. *Rubber Chem. Technol*, 58(1):107–116, 1985.

[20] C. Xu, C. Walsh, E. Boaretto, and K. M. Poduska. Assessing the feasibility of electrophoretic separation of $CaCO_3$ polymorphs for archaeological applications. *Anal. Methods*, 9(3):427–433, 2017.

[21] P. Q. Yuan, Z. M. Cheng, Z. M. Zhou, W. K. Yuan, and R. Semiat. Zeta potential on the anti-scalant modified sub-micro calcite surface. *Colloids Surf. A Physicochem. Eng. Asp*, 328(1-3):60–66, 2008.

[22] M. Ni and B. D. Ratner. Nacre surface transformation to hydroxyapatite in a phosphate buffer solution. *Biomaterials*, 24(23):4323–4331, 2003.

[23] F. H. Butt, F. Rahman, and U. Baduruthamal. Evaluation of SHMP and advanced scale inhibitors for control of $CaSO_4$, $SrSO_4$, and $CaCO_3$ scales in RO desalination. *Desalination*, 109(3):323–332, 1997.

[24] S. C. de Morais, D. F. de Lima, T. M. Ferreira, J. B. Domingos, M. A. F. de Souza, B. B. Castro, and R. C. Balaban. Effect of pH on the efficiency of sodium hexametaphosphate as calcium carbonate scale inhibitor at high temperature and high pressure. *Desalination*, 491:114548, 2020.

[25] W. Sekkal and A. Zaoui. Nanoscale analysis of the morphology and surface stability of calcium carbonate polymorphs. *Sci. Rep*, 3(1):1–10, 2013.

[26] H. Shindo and M. Kwak. Stabilities of crystal faces of aragonite ($CaCO_3$) compared by atomic force microscopic observation of facet formation processes in aqueous acetic acid. *Phys. Chem. Chem. Phys*, 7:691–696, 2005.

[27] N. H. de Leeuw and S. C. Parker. Surface structure and morphology of calcium carbonate polymorphs calcite, aragonite, and vaterite: an atomistic approach. *J. Phys. Chem. B*, 102(16):2914–2922, 1998.

[28] M. Kwak and H. Shindo. Atomic force microscopic observation of facet formation on various faces of aragonite in aqueous acetic acid. *J. Cryst. Growth*, 275(1-2):e1655–e1659, 2005.

[29] G. V. Chilingar, R. Mourhatch, and G. D. Al-Qahtani. Chapter 6 - scaling. In George V. Chilingar, Ryan Mourhatch, and Ghazi D. Al-Qahtani, editors, *The Fundamentals of Corrosion and Scaling for Petroleum & Environmental Engineers*, pages 117–139. Gulf Publishing Company, 2008.

[30] R. H. Petrucci. *General chemistry: principles and modern applications*. Pearson, 2017.

[31] W. B. Euler, L. J. Kirschenbaum, and B. Ruekberg. Determination of K_{sp}, ΔG_0, ΔH_0, and ΔS_0. *J. Chem. Educ*, 77(8):1039, 2000.

[32] A. Maria M. Kaczmarczyk, A. Spórna-Kucab, and T. Michałowski. Solubility products and solubility concepts. *Descriptive Inorganic Chemistry. Researches of Metal Compounds. Akitsu T.(Ed.) InTech*, pages 93–134, 2017.

[33] J. Kanakis, P. Malkaj, J. Petroheilos, and E. Dalas. The crystallization of calcium carbonate on porcine and human cardiac valves and the antimineralization effect of sodium alginate. *J. Cryst. Growth*, 223(4):557–564, 2001.

[34] J. W. Morse, R. S. Arvidson, and A. Lüttge. Calcium carbonate formation and dissolution. *Chem. Rev*, 107(2):342–381, 2007.

[35] B. Coto, C. Martos, J. L. Peña, R. Rodríguez, and G. Pastor. Effects in the solubility of $CaCO_3$: Experimental study and model description. *Fluid Phase Equilib*, 324:1–7, 2012.

[36] O. S. Pokrovsky, S. V. Golubev, J. Schott, and A. Castillo. Calcite, dolomite and magnesite dissolution kinetics in aqueous solutions at acid to circumneutral pH, 25 to 150 °C and 1 to 55 atm pCO_2: New constraints on CO_2 sequestration in sedimentary basins. *Chem. Geol*, 265(1-2):20–32, 2009.

[37] E. M. Pouget, P. H. H. Bomans, J. A. C. M. Goos, P. M. Frederik, G. de With, and N. A. J. M. Sommerdijk. The initial stages of template-controlled $CaCO_3$ formation revealed by Cryo-TEM. *Science*, 323(5920):1455–1458, 2009.

[38] J. Rieger, T. Frechen, G. Cox, W. Heckmann, C. Schmidt, and J. Thieme. Precursor structures in the crystallization/precipitation processes of $CaCO_3$ and control of particle formation by polyelectrolytes. *Faraday Discuss*, 136:265–277, 2007.

[39] J. W. Mullin and O. Söhnel. Expressions of supersaturation in crystallization studies. *Chem. Eng. Sci*, 32(7):683–686, 1977.

[40] J. J. De Yoreo and P. G. Vekilov. Principles of Crystal Nucleation and Growth. *Rev. Mineral. Geochem*, 54(1):57–93, 2003.

[41] K. Henzler, E. O. Fetisov, M. Galib, M. D. Baer, B. A. Legg, C. Borca, J. M. Xto, S. Pin, J. L. Fulton, G. K. Schenter, et al. Supersaturated calcium carbonate solutions are classical. *Sci. Adv*, 4(1):eaao6283, 2018.

[42] K. B. Krauskopf and D. K. Bird. *Introduction to geochemistry*, volume 721. McGraw-Hill New York, 1967.

[43] M. Perez. Gibbs-Thomson effects in phase transformations. *Scr. Mater*, 52(8):709–712, 2005.

[44] F. F. Abraham. *Homogeneous nucleation theory*, volume 263. Elsevier, 1974.

[45] G. H. Nancollas and M. M. Reddy. The crystallization of calcium carbonate. II. Calcite growth mechanism. *J. Colloid Interface Sci*, 37(4):824–830, 1971.

[46] D. Gebauer and H. Cölfen. Prenucleation clusters and non-classical nucleation. *Nano Today*, 6(6):564–584, 2011.

[47] D. Gebauer, A. Volkel, and H. Cölfen. Stable prenucleation calcium carbonate clusters. *Science*, 322(5909):1819–1822, 2008.

[48] M. Niederberger and H. Cölfen. Oriented attachment and mesocrystals: Non-classical crystallization mechanisms based on nanoparticle assembly. *Phys. Chem. Chem. Phys*, 8:3271–3287, 2006.

[49] Y. Politi, Y. Levi-Kalisman, S. Raz, F. Wilt, L. Addadi, S. Weiner, and I. Sagi. Structural characterization of the transient amorphous calcium carbonate precursor phase in sea urchin embryos. *Adv. Funct. Mater*, 16(10):1289–1298, 2006.

[50] S. Weiner, J. Mahamid, Y. Politi, Y. R. Ma, and L. Addadi. Overview of the amorphous precursor phase strategy in biomineralization. *Front. Mater. Sci. China*, 3(2):104–108, 2009.

[51] D. Gebauer, P. N. Gunawidjaja, J. Y. P. Ko, Z. Bacsik, B. Aziz, L. J. Liu, Y. F. Hu, L. Bergström, C. W. Tai, T. K. Sham, et al. Proto-calcite and proto-vaterite in amorphous calcium carbonates. *Angew. Chem. Int. Ed*, 49(47):8889–8891, 2010.

[52] R. S. K. Lam, J. M. Charnock, A. Lennie, and F. C. Meldrum. Synthesis-dependant structural variations in amorphous calcium carbonate. *CrystEngComm*, 9(12):1226–1236, 2007.

[53] D. Hasson and A. Cornel. Effect of residence time on the degree of $CaCO_3$ precipitation in the presence of an anti-scalant. *Desalination*, 401:64–67, 2017.

[54] K. Sawada. The mechanisms of crystallization and transformation of calcium carbonates. *Pure Appl. Chem*, 69(5):921–928, 1997.

[55] K. K. Mallick and J. Winnett. 3D bioceramic foams for bone tissue engineering. In *Bone Substitute Biomaterials*, pages 118–141. Elsevier, 2014.

[56] H. U. Sø, D. Postma, R. Jakobsen, and F. Larsen. Sorption of phosphate onto calcite; results from batch experiments and surface complexation modeling. *Geochim. Cosmochim. Acta*, 75(10):2911–2923, 2011.

[57] N. Xu, H. Yin, Z. Chen, S. Liu, M. Chen, and J. Zhang. Mechanisms of phosphate retention by calcite: Effects of magnesium and pH. *J. Soils Sediments*, 14(3):495–503, 2014.

[58] Y. P. Guo, Y. Zhou, D. C. Jia, and H. X. Tang. Fabrication and characterization of hydroxycarbonate apatite with mesoporous structure. *Microporous Mesoporous Mater*, 118(1-3):480–488, 2009.

[59] Y. Wang, Y. X. Moo, C. Chen, P. Gunawan, and R. Xu. Fast precipitation of uniform $CaCO_3$ nanospheres and their transformation to hollow hydroxyapatite nanospheres. *J. Colloid Interface Sci*, 352(2):393–400, 2010.

[60] X. Cao and W. Harris. Carbonate and magnesium interactive effect on calcium phosphate precipitation. *Environ. Sci. Technol*, 42(2):436–442, 2008.

[61] N. Xu, M. Chen, K. Zhou, Y. Wang, H. Yin, and Z. Chen. Retention of phosphorus on calcite and dolomite: Speciation and modeling. *RSC Adv*, 4(66):35205–35214, 2014.

[62] J. D. Schuttlefield and V. H. Grassian. ATR-FTIR spectroscopy in the undergraduate chemistry laboratory. Part I: fundamentals and examples. *J. Chem. Educ*, 85(2):279, 2008.

[63] M. Milosevic. On the nature of the evanescent wave. *Appl. Spectrosc*, 67(2):126–131, 2013.

[64] I. A. Mudunkotuwa, A. A. Minshid, and V. H. Grassian. ATR-FTIR spectroscopy as a tool to probe surface adsorption on nanoparticles at the liquid-solid interface in environmentally and biologically relevant media. *Analyst*, 139:870–881, 2014.

[65] M. Milosevic. Internal reflection and ATR spectroscopy. *Appl. Spectrosc. Rev*, 39(3):365–384, 2004.

[66] M. K. Singh and A. Singh. *Characterization of polymers and fibres*. Elsevier, 2021.

[67] A. D. Bain. Exact calculation, using angular momentum, of combined Zeeman and quadrupolar interactions in NMR. *Mol. Phys*, 101(21):3163–3175, 2003.

[68] R. John Abraham, J. Fisher, and P. Loftus. *Introduction to NMR spectroscopy*, volume 2. Wiley New York, 1998.

[69] C. J. Jameson. Understanding NMR chemical shifts. *Annu. Rev. Phys. Chem*, 47(1):135–169, 1996.

[70] R. Tycko and G. Dabbagh. Measurement of nuclear magnetic dipole-dipole couplings in magic angle spinning NMR. *Chem. Phys. Lett*, 173(5):461–465, 1990.

[71] D. D. Laws, H. L. Bitter, and A. Jerschow. Solid-state NMR spectroscopic methods in chemistry. *Angew. Chem. Int. Ed*, 41(17):3096–3129, 2002.

[72] C. Dybowski and S. Bai. Solid-state NMR spectroscopy. *Anal. Chem*, 80(12):4295–4300, 2008.

[73] E. R. Andrew. Magic angle spinning. *Int. Rev. Phys. Chem*, 1(2):195–224, 1981.

[74] A. Akiva-Tal, S. Kababya, Y. S. Balazs, L. Glazer, A. Berman, A. Sagi, and A. Schmidt. In situ molecular NMR picture of bioavailable calcium stabilized as amorphous $CaCO_3$ biomineral in crayfish gastroliths. *Proc. Natl. Acad. Sci*, 108(36):14763–14768, 2011.

[75] W. Kolodziejski and J. Klinowski. Kinetics of cross-polarization in solid-state NMR: a guide for chemists. *Chem. Rev*, 102(3):613–628, 2002.

[76] R. L. Johnson and K. Schmidt-Rohr. Quantitative solid-state ^{13}C NMR with signal enhancement by multiple cross polarization. *J. Magn. Reson*, 239:44–49, 2014.

[77] T. Gullion. Introduction to rotational-echo, double-resonance NMR. *Concepts Magn. Reson. Part A Bridg. Educ. Res*, 10(5):277–289, 1998.

[78] T. Gullion. Rotational-echo, double-resonance NMR. In *Modern Magnetic Resonance*, pages 713–718. Springer, 2008.

[79] R. Gertman, I. B. Shir, S. Kababya, and A. Schmidt. In situ observation of the internal structure and composition of biomineralized *emiliania huxleyi* calcite by solid-state NMR spectroscopy. *J. Am. Chem. Soc*, 130:13425–13432, 2008.

[80] J. Aizenberg, L. Addadi, S. Weiner, and G. Lambert. Stabilization of amorphous calcium carbonate by specialized macromolecules in biological and synthetic precipitates. *Adv. Mater*, 8(3):222–226, 1996.

[81] I. Ben Shir, S. Kababya, I. Katz, B. Pokroy, and A. Schmidt. Exposed and buried biomineral interfaces in the aragonitic shell of *perna canaliculus* revealed by solid-state NMR. *Chem. Mater*, 25(22):4595–4602, 2013.

[82] H. Nebel, M. Neumann, C. Mayer, and M. Epple. On the structure of amorphous calcium carbonate - a detailed study by solid-state NMR spectroscopy. *Inorg. Chem*, 47(17):7874–7879, 2008.

[83] S. Kababya, A. Gal, K. Kahil, S. Weiner, L. Addadi, and A. Schmidt. Phosphate-water interplay tunes amorphous calcium carbonate metastability: Spontaneous phase separation and crystallization vs stabilization viewed by solid state NMR. *J. Am. Chem. Soc*, 137(2):990–998, 2015.

[84] B. Gao and K. M. Poduska. Tracking amorphous calcium carbonate crystallization products with Far-infrared spectroscopy. *Minerals*, submitted 06 December 2022.

[85] B. Gao and K. M. Poduska. Comparing polyphosphate and orthophosphate treatments of solution-precipitated aragonite powders. *Solids*, accepted 18 November 2022.

[86] Y. Boyjoo, V. K. Pareek, and J. Liu. Synthesis of micro and nano-sized calcium carbonate particles and their applications. *J. Mater. Chem. A*, 2:14270–14288, 2014.

[87] O. A. Jimoh, K. S. Ariffin, H. B. Hussin, and A. E. Temitope. Synthesis of precipitated calcium carbonate: a review. *Carbonates Evaporites*, 33:331–346, 2018.

[88] C. Ramakrishna, T. Thenepalli, C. Han, and J. W. Ahn. Synthesis of aragonite-precipitated calcium carbonate from oyster shell waste via a carbonation process and its applications. *Korean J. Chem. Eng*, 34:225–230, 2017.

[89] R. M. Santos, P. Ceulemans, and T. V. Gerven. Synthesis of pure aragonite by sonochemical mineral carbonation. *Chem. Eng. Res. Des*, 90:715–725, 2012.

[90] C. Wang, J. Zhao, X. Zhao, H. Bala, and Z. Wang. Synthesis of nanosized calcium carbonate (aragonite) via a polyacrylamide inducing process. *Powder Technol*, 163:134–138, 2006.

[91] D. Konopacka-Łyskawa, N. Czaplicka, M. Łapiński, B. Kościelska, and R. Bray. Precipitation and transformation of vaterite calcium carbonate in the presence of some organic solvents. *Materials*, 13(12), 2020.

[92] P. U. P. A. Gilbert, K. D. Bergmann, N. Boekelheide, S. Tambutté, T. Mass, F. Marin, J. F. Adkins, J. Erez, B. Gilbert, V. Knutson, M. Cantine, J. O. Hernández, and A. H. Knoll. Biomineralization: Integrating mechanism and evolutionary history. *Sci. Adv*, 8(10):eabl9653, 2022.

[93] A. Yang, Z. Huang, Y. Zhu, Y. Han, and Z. Tong. Preparation of nano-sized calcium carbonate in solution mixing process. *J. Cryst. Growth*, 571, 2021.

[94] T. Zheng, X. Zhang, and H. Yi. Spherical vaterite microspheres of calcium carbonate synthesized with poly (acrylic acid) and sodium dodecyl benzene sulfonate. *J. Cryst. Growth*, 528:125275, 2019.

[95] C. Ramakrishna, T. Thenepalli, and J. W. Ahn. A brief review of aragonite precipitated calcium carbonate (PCC) synthesis methods and its applications. *Korean Chem. Eng. Res*, 55:443–455, 2017.

[96] M. Ma, Y. Wang, X. Cao, W. Lu, and Y. Guo. Temperature and supersaturation as key parameters controlling the spontaneous precipitation of calcium carbonate with distinct physicochemical properties from pure aqueous solutions. *Cryst. Growth Des*, 19:6972–6988, 2019.

[97] J. L. Wray and F. Daniels. Precipitation of calcite and aragonite. *J. Am. Chem. Soc*, 79(9):2031–2034, 1957.

[98] M. Chang and C. Y. Tai. Effect of the magnetic field on the growth rate of aragonite and the precipitation of $CaCO_3$. *J. Chem. Eng*, 164(1):1–9, 2010.

[99] C. Y. Tai, M. Chang, and S. W. Yeh. Synergetic effects of temperature and magnetic field on the aragonite and calcite growth. *Chem. Eng. Sci*, 66(6):1246–1253, 2011.

[100] J. W. Ahn, W. K. Park, K. S. You, H. C. Cho, S. J. Ko, and C. Han. Roles of additives on crystal growth rate of precipitated calcium carbonate. *Solid State Phenom*, 124-126(PART 1):707–710, 2007.

[101] Z. Hu, M. Shao, Q. Cai, S. Ding, C. Zhong, X. Wei, and Y. Deng. Synthesis of needle-like aragonite from limestone in the presence of magnesium chloride. *J. Mater. Process. Technol*, 209(3):1607–1611, 2009.

[102] W. Sun, S. Jayaraman, W. Chen, K. A. Persson, and G. Ceder. Nucleation of metastable aragonite $CaCO_3$ in seawater. *Proc. Natl. Acad. Sci. U.S.A*, 112(11):3199–3204, 2015.

[103] W. K. Park, S. J. Ko, S. W. Lee, K. H. Cho, J. W. Ahn, and C. Han. Effects of magnesium chloride and organic additives on the synthesis of aragonite precipitated calcium carbonate. *J. Cryst. Growth*, 310(10):2593–2601, 2008.

[104] X. Yang and G. Xu. The influence of xanthan on the crystallization of calcium carbonate. *J. Cryst. Growth*, 314(1):231–238, 2011.

[105] L. Zhang, L. Yue, F. Wang, and Q. Wang. Divisive effect of alcohol−water mixed solvents on growth morphology of calcium carbonate crystals. *J. Phys. Chem. B*, 112(34):10668–10674, 2008.

[106] L. Chuzeville, F. Boury, D. Duday, R. Anand, E. Moretto, and J. Thomann. Eco-friendly processes for the synthesis of amorphous calcium carbonate nanoparticles in ethanol and their stabilisation in aqueous media. *Green Chem*, 24(3):1270–1284, 2022.

[107] K. Seo, C. Han, J. Wee, J. Park, and J. Ahn. Synthesis of calcium carbonate in a pure ethanol and aqueous ethanol solution as the solvent. *J. Cryst. Growth*, 276(3):680–687, 2005.

[108] E. M. Sánchez, M. G. Willinger, C. M. Pina, and A. G. Checa. Transformation of ACC into aragonite and the origin of the nanogranular structure of nacre. *Sci. Rep*, 7, 2017.

[109] E. Tolba, W. E. G. Müller, B. M. Abd El-Hady, M. Neufurth, F. Wurm, S. Wang, H. C. Schröder, and X. Wang. High biocompatibility and improved osteogenic potential of amorphous calcium carbonate/vaterite. *J. Mater. Chem. B*, 4:376–386, 2016.

[110] B. Xu, A. Hirsch, L. Kronik, and K. M. Poduska. Vibrational properties of isotopically enriched materials: the case of calcite. *RSC Adv*, 8(59):33985–33992, 2018.

[111] B. Xu and K. M. Poduska. Linking crystal structure with temperature-sensitive vibrational modes in calcium carbonate minerals. *Phys. Chem. Chem. Phys*, 16(33):17634–17639, 2014.

[112] C. Günther, A. Becker, G. Wolf, and M. Epple. In vitro synthesis and structural characterization of amorphous calcium carbonate. *Z. Anorg. Allg. Chem*, 631:2830–2835, 2005.

[113] P. K. Ajikumar, G. W. Ling, G. Subramanyam, R. Lakshminarayanan, and S. Valiyaveettil. Synthesis and characterization of monodispersed spheres of amorphous calcium carbonate and calcite spherules. *Cryst. Growth Des*, 5:1129–1134, 2005.

[114] S. Feng Chen, H. Cölfen, M. Antonietti, and S. H. Yu. Ethanol assisted synthesis of pure and stable amorphous calcium carbonate nanoparticles. *Chem. Comm*, 49:9564–9566, 2013.

[115] K. B. Krauskopf and D. K. Bird. Solution-mineral equilibria part 1: carbonates. *Introduction of Geochemistry*, pages 61–83, 1995.

[116] A. M. Bano, P. M. Rodger, and D. Quigley. New insight into the stability of $CaCO_3$ surfaces and nanoparticles via molecular simulation. *Langmuir*, 30(25):7513–7521, 2014.

[117] A. G. Stack. Next generation models of carbonate mineral growth and dissolution. *Greenhouse Gas Sci. Technol*, pages 278–288, 2014.

[118] D. E. Abd-El-Khalek and B. A. Abd-El-Nabey. Evaluation of sodium hexametaphosphate as scale and corrosion inhibitor in cooling water using electrochemical techniques. *Desalination*, 311:227–233, 2013.

[119] T. Nakatsuka, H. Kawasaki, K. Itadani, and S. Yamashita. Phosphate coupling agents for calcium carbonate filler. *J. Appl. Polym. Sci*, 27(1):259–269, 1982.

[120] T. H. Chong and R. Sheikholeslami. Thermodynamics and kinetics for mixed calcium carbonate and calcium sulfate precipitation. *Chem. Eng. Sci*, 56(18):5391–5400, 2001.

[121] S. Muryanto, A. P. Bayuseno, H. Ma'mun, M. Usamah, and Jotho. Calcium carbonate scale formation in pipes: effect of flow rates, temperature, and malic acid as additives on the mass and morphology of the scale. *Procedia. Chem*, 9:69–76, 2014.

[122] M. B. Toffolo, L. Regev, E. Mintz, K. M. Poduska, R. Shahack-Gross, C. Berthold, C. E. Miller, and E. Boaretto. Accurate radiocarbon dating of archaeological ash using pyrogenic aragonite. *Radiocarbon*, pages 231–249, 2017.

[123] A. Li, H. Zhang, Q. Liu, and H. Zeng. Effects of chemical inhibitors on the scaling behaviors of calcite and the associated surface interaction mechanisms. *J. Colloid Interface Sci*, 618:507–517, 2022.

[124] H. Liu, H. Huang, X. Wu, K. Wu, J. Hu, J. Wei, and Q. Yu. Interactions between organic chelation agents and ions in seawater for accelerating self-healing of cracks in cement paste. *J. Mater. Civ. Eng*, 33(4):04021036, 2021.

[125] C. Combes, B. Miao, R. Bareille, and C. Rey. Preparation, physical–chemical characterisation and cytocompatibility of calcium carbonate cements. *Biomaterials*, 27(9):1945–1954, 2006.

[126] C. Combes, S. Tadier, H. Galliard, S. Girod-Fullana, C. Charvillat, C. Rey, R. Auzély-Velty, and N. El Kissi. Rheological properties of calcium carbonate self-setting injectable paste. *Acta Biomater*, 6(3):920–927, 2010.

[127] N. Xu, Y. Wang, X. Xu, C. Liu, J. Qian, and G. Feng. Mechanisms and applications of the synthesized fusiform aragonite for the removal of high concentration of phosphate. *Water Air Soil Pollut*, 227, 2016.

[128] N. Pismenskaya, E. Laktionov, V. Nikonenko, A. El Attar, B. Auclair, and G. Pourcelly. Dependence of composition of anion-exchange membranes and

their electrical conductivity on concentration of sodium salts of carbonic and phosphoric acids. *J. Membr. Sci*, 181(2):185–197, 2001.

[129] W. B. White. The Carbonate Minerals. In *The Infrared Spectra of Minerals*. Mineralogical Society of Great Britain and Ireland, 1974.

[130] L. Valenzano, Y. Noel, R. Orlando, C. M. Zicovich-Wilson, M. Ferrero, and R. Dovesi. Ab initio vibrational spectra and dielectric properties of carbonates: magnesite, calcite and dolomite. *Theor. Chem. Acc*, 117(5-6):991–1000, 2007.

[131] Maryam H. Derkani, Ashleigh J. Fletcherand Maxim Fedorov, Wael Abdallah, Bastian Sauerer, James Anderson, and Zhenyu J. Zhang. Mechanisms of surface charge modification of carbonates in aqueous electrolyte solutions. *Colloids Interfaces*, pages 62:1–19, 2019.

[132] J. Perić, R. Krstulović, T. Ferić, and M. Vučak. The examination of the phase transformation of aragonite into calcite by means of DSC analysis. *Thermochim. Acta*, 207:245–254, 1992.

[133] N. Koga, D. Kasahara, and T. Kimura. Aragonite crystal growth and solid-state aragonite–calcite transformation: a physico–geometrical relationship via thermal dehydration of included water. *Cryst. Growth Des*, 13(5):2238–2246, 2013.

[134] Yuki Kezuka, Kosuke Kawai, Kenichiro Eguchi, and Masahiko Tajika. Fabrication of single-crystalline calcite needle-like particles using the aragonite–calcite phase transition. *Minerals*, 7(8), 2017.

[135] T. Hanein, M. Simoni, C. L. Woo, J. L. Provis, and H. Kinoshita. Decarbonisation of calcium carbonate at atmospheric temperatures and pressures, with

simultaneous CO_2 capture, through production of sodium carbonate. *Energy Environ. Sci*, 14:6595–6604, 2021.

[136] H. N. Po and N. M. Senozan. The Henderson-Hasselbalch equation: its history and limitations. *J. Chem. Educ*, 78(11):1499, 2001.

[137] M. Gashti, M. P.and Bourquin, M. Stir, and J. Hulliger. Glutamic acid inducing kidney stone biomimicry by a brushite/gelatin composite. *J. Mater. Chem. B*, 1:1501–1508, 2013.

[138] C. Liao, F. Lin, K. Chen, and J. Sun. Thermal decomposition and reconstitution of hydroxyapatite in air atmosphere. *Biomaterials*, 20(19):1807–1813, 1999.

[139] A. Dosen and R. F. Giese. Thermal decomposition of brushite $CaHPO_4 \cdot 2H_2O$, to monetite $CaHPO_4$ and the formation of an amorphous phase. *Am. Mineral*, 96(2-3):368–373, 2011.

[140] R. S. Arvidson and J. W. Morse. Formation and diagenesis of carbonate sediments. In H. D. Holland and K. K. Turekian, editors, *Treatise on Geochemistry (Second Edition)*, pages 61–101. Elsevier, Oxford, second edition edition, 2014.

[141] M. Schulte, D. Blake, T. Hoehler, and T. Mccollom. Serpentinization and its implications for life on the early Earth and Mars. *Astrobiology*, 6:364–376, 2006.

[142] P. B. Kelemen, J. Matter, E. E. Streit, J. F. Rudge, W. B. Curry, and J. Blusztajn. Rates and mechanisms of mineral carbonation in peridotite: Natural processes and recipes for enhanced, in situ CO_2 capture and storage. *Annu. Rev. Earth Planet Sci*, 39:545–576, 2011.

[143] N. H. Sleep, D. K. Bird, and E. C. Pope. Serpentinite and the dawn of life. *Philos. Trans. R. Soc. Lond., B, Biol. Sci*, 366:2857–2869, 2011.

[144] D. Cardace and T. M. Hoehler. Serpentinizing fluids craft microbial habitat. *Northeast Nat*, 16:272–284, 2009.

[145] M. C. Cook, J. G. Blank, A. Rietze1, S. Suzuki, K. H. Nealson, and P. L. Morrill. A geochemical comparison of three terrestrial sites of serpentinization: The Tablelands, the Cedars, and Aqua de Ney. *J. Geophys. Res. Biogeosci*, 126:1–20, 2021.

[146] B. R. Frost and J. S. Beard. On silica activity and serpentinization. *J. Petrol*, 48:1351–1368, 2007.

[147] K. A. Ludwig, D. S. Kelley, D. A. Butterfield, B. K. Nelson, and G. Früh-Green. Formation and evolution of carbonate chimneys at the Lost City Hydrothermal Field. *Geochim. Cosmochim. Acta*, 70:3625–3645, 2006.

[148] P. L. Morrill, J. G. Kuenen, O. J. Johnson, S. Suzuki, A. Rietze, A. L. Sessions, M. L. Fogel, and K. H. Nealson. Geochemistry and geobiology of a present-day serpentinization site in California: The Cedars. *Geochim. Cosmochim. Acta*, 109:222–240, 2013.

[149] O. Müntener. Serpentine and serpentinization: A link between planet formation and life. *Geology*, 38(10):959–960, 2010.

[150] N. G. Holm, C. Oze, O. Mousis, J. H. Waite, and A. Guilbert-Lepoutre. Serpentinization and the formation of H_2 and CH_4 on celestial bodies (Planets, Moons, Comets). *Astrobiology*, 15:587–600, 2015.

[151] Satellite Imaging Corporation. Worldview-3 satellite sensor specifications, 2013.

[152] B. L. Ehlmann, J. F. Mustard, S. L. Murchie, F. Poulet, J. L. Bishop, A. J. Brown, W. M. Calvin, R. N. Clark, D. J. Des Marais, R. E. Milliken, L. H.

Roach, T. L. Roush, G. A. Swayze, and J. J. Wray. Orbital identification of carbonate-bearing rocks on Mars. *Science*, 322:1828–1832, 2008.

[153] R. V. Morris, S. W. Ruff, R. Gellert, D. W. Ming, R. E. Arvidson, B. C. Clark, D. C. Golden, K. Siebach, G. Klingelhöfer, C. Schröder, I. Fleischer, A. S. Yen, and S. W. Squyres. Identification of carbonate-rich outcrops on Mars by the Spirit Rover. *Science*, 329:421–424, 2010.

[154] J. R. Johnson, C. Achilles, J. F. Bell III, S. Bender, E. Cloutis, B. Ehlmann, A. Fraeman, O. Gasnault, V. E. Hamilton, S. Le Mouélic, S. Maurice, P. Pinet, L. Thompson, D. Wellington, and R. C. Wiens. Visible/near-infrared spectral diversity from in situ observations of the Bagnold Dune Field sands in Gale Crater, Mars. *J. Geophys. Res. Planets*, 122:2655–2684, 2017.

[155] M. G. A. Lapotre, B. L. Ehlmann, S. E. Minson, R. E. Arvidson, F. Ayoub, A. A. Fraeman, R. C. Ewing, and N. T. Bridges. Compositional variations in sands of the Bagnold Dunes, Gale crater, Mars, from visible-shortwave infrared spectroscopy and comparison with ground truth from the Curiosity rover. *J. Geophys. Res. Planets*, 122:2489–2509, 2016.

[156] R. N. Greenberger, J. F. Mustard, E. A. Cloutis, P. Mann, J. H. Wilson, R. L. Flemming, K. M. Robertson, M. R. Salvatore, and C. S. Edwards. Hydrothermal alteration and diagenesis of terrestrial lacustrine pillow basalts: Coordination of hyperspectral imaging with laboratory measurements. *Geochim. Cosmochim. Acta*, 171:174–200, 2015.

[157] B. Bultel, J. C. Viennet, F. Poulet, J. Carter, and S. C. Werner. Detection of carbonates in Martian weathering profiles. *J. Geophys. Res. Planets*, 124:989–1007, 2019.

[158] E. K. Leask, B. L. Ehlmann, R. N. Greenberger, P. Pinet, Y. Daydou, G. Ceuleneer, and P. Kelemen. Tracing carbonate formation, serpentinization, and biological materials with micro-/meso-scale infrared imaging spectroscopy in a Mars analog system, Samail Ophiolite, Oman. *Earth Space Sci*, 8:1–30, 2021.

[159] R. N. Greenberger, J. F. Mustard, B. L. Ehlmann, D. L. Blaney, E. A. Cloutis, J. H. Wilson, R. O. Green, and A. A. Fraeman. Imaging spectroscopy of geological samples and outcrops: Novel insights from microns to meters. *GSA Today*, 25:4–10, 2016.

[160] C. Pilorget, J. Fernando, B. L. Ehlmann, F. Schmidt, and T. Hiroi. Wavelength dependence of scattering properties in the VIS–NIR and links with grain-scale physical and compositional properties. *Icarus*, 267:296–314, 2016.

[161] C. M. Simonescu. Application of FTIR spectroscopy in environmental studies. In Muhammad Akhyar Farrukh, editor, *Advanced Aspects of Spectroscopy*, chapter 2. IntechOpen, Rijeka, 2012.

[162] S. J. Gaffey. Spectral reflectance of carbonate minerals in the visible and near infrared (0.35-2.55 microns): calcite, aragonite, and dolomite. *Am. Mineral*, 71:151–162, 1986.

[163] S. Weiner. *Microarchaeology: Beyond the visible archaeological record*. Cambridge University Press, 2010.

[164] J. L. Bishop, S. J. King, D. Lane, A. J. Brown, B. Lafuente, T. Hiroi, R. Roberts, G. A. Swayze, J.-F. Lin, and M. Sánchez Rom/'an. Spectral properties of anhydrous carbonates and nitrates. *Earth Space Sci*, 8:e2021EA001844 (1–43), 2021.

[165] J. C. Viennet, S. Bernard, C. Le Guillou, P. Jacquemot, E. Balan, L. Delbes, B. Rigaud, T. Georgelin, and M. Jaber. Experimental clues for detecting biosignatures on Mars. *geochem. perspect. Lett*, 12:28–33, 2019.

[166] J. Demšar, T. Curk, A. Erjavec, Črt Gorup, T. Hočevar, M. Milutinovič, M. Možina, M. Polajnar, M. Toplak, A. Starič, M. Štajdohar, L. Umek, L. Žagar, J. Žbontar, M. Žitnik, and B. Zupan. Orange: Data mining toolbox in python. *J Mach Learn Res*, 14:2349–2353, 2013.

[167] R.F. Kokaly, Swayze Clark, R.N., Livo G.A., T.M. K.E., Hoefen, N.C. Pearson, R.A. Wise, W.M. Benzel, H.A Lowers, R.L. Driscoll, and A.J. Klein. Original measurements made using lab, field and imaging spectrometers. page USGS Spectral Library Version 7: U.S. Geological Survey Data Series 1035, 2017.

[168] CRYSTAL - Theoretical Chemistry Group (Torino, Italy). Animating the crystal vibration frequencies, 2021.

[169] C. Carteret, M. De La Pierre, M. Dossot, F. Pascale, A. Erba, and R. Dovesi. The vibrational spectrum of $CaCO_3$ aragonite: A combined experimental and quantum-mechanical investigation. *J. Chem. Phys*, 138(1):014201, 2013.

[170] E. Fritsch, E. Balan, S. Petit, and F. Juillot. Vibrational spectroscopic study of three Mg-Ni mineral series in white and greenish clay infillings of the New Caledonian Ni-silicate ores. *Eur. J. Mineral*, 33:743–763, 2021.

[171] V. Chavagnac, G. Ceuleneer, C. Monnin, B. Lansac, G. Hoareau, and C. Boulart. Mineralogical assemblages forming at hyperalkaline warm springs hosted on ultramafic rocks: A case study of Oman and Ligurian ophiolites. *Geochem. Geophys. Geosyst*, 14:2474–2495, 2013.

[172] E.S. Falk, W. Guo, A.N. Paukert, J.M. Matter, E.M. Mervine, and P.B. Kelemen. Controls on the stable isotope compositions of travertine from hyperalkaline springs in Oman: Insights from clumped isotope measurements. *Geochim. Cosmochim. Acta*, 192:1–28, 2016.

[173] M. Giampouras, C. J. Garrido, J. Zwicker, I. Vadillo, D. Smrzka, W. Bach, J. Peckmann, P. Jiménez, J. Benavente, and J. M. García-Ruiz. Geochemistry and mineralogy of serpentinization-driven hyperalkaline springs in the Ronda peridotites. *Lithos*, 350-351:105215, 2019.

[174] C. Boschi, F. Bedini, I. Baneschi, A. Rielli, L. Baumgartner, N. Perchiazzi, A. Ulyanov, G. Zanchetta, and A. Dini. Spontaneous serpentine carbonation controlled by underground dynamic microclimate at the Montecastelli Copper Mine, Italy. *Minerals*, 10, 2019.

[175] J. N. Christensen, J. M. Watkins, L. S. Devriendt, D. J. DePaolo, M. E. Conrad, M. Voltolini, W. Yang, and W. Dong. Isotopic fractionation accompanying CO_2 hydroxylation and carbonate precipitation from high pH waters at The Cedars, California, USA. *Geochim. Cosmochim. Acta*, 301:91–115, 2021.

[176] A. N. Paukert, J. M. Matter, P. B. Kelemen, E. L. Shock, and J. R. Havig. Reaction path modeling of enhanced in situ CO_2 mineralization for carbon sequestration in the peridotite of the Samail Ophiolite, Sultanate of Oman. *Chem. Geol*, 330-331:86–100, 2012.

[177] E. M. Mervine, S. E. Humphris, K. W. W. Sims, P. B. Kelemen, and W. J. Jenkins. Carbonation rates of peridotite in the Samail Ophiolite, Sultanate of Oman, constrained through ^{14}C dating and stable isotopes. *Geochim. Cosmochim. Acta*, 126:371–397, 2014.

[178] K. U. Brady, A. R. Kruckeberg, and H. D. Bradshaw. Evolutionary ecology of plant adaptation to serpentine soils. *Annu. Rev. Ecol. Evol. Syst*, 36(1858):243–266, 2005.

[179] G. T. Prance. Serpentine and its vegetation. a multidisciplinary approach. *Brittonia*, 40(3):268, 1988.

[180] J. Proctor and S. R. J. Woodell. The ecology of serpentine soils. *Adv. Ecol. Res*, 9:255–366, 1975.

[181] M. Yao, B. Lian, H. H. Teng, Y. Tian, and X. Yang. Serpentine dissolution in the presence of bacteria bacillus mucilaginosus. *Geomicrobiol. J*, 30(1):72–80, 2013.

[182] E. Kazakou, P. G. Dimitrakopoulos, A. J. M. Baker, R. D. Reeves, and A. Y. Troumbis. Hypotheses, mechanisms and trade-offs of tolerance and adaptation to serpentine soils: from species to ecosystem level. *Biol. Rev*, 83(4):495–508, 2008.

[183] S. M. Y. Baugé, L. M. Lavkulich, and H. E. Schreier. Serpentine affected soils and the formation of magnesium phosphates (struvite). *Can. J. Soil Sci*, 93(2):161–172, 2013.

[184] M. Boon, W. D. A. Rickard, A. L. Rohl, and F. Jones. Stabilization of aragonite: role of Mg^{2+} and other impurity ions. *Cryst. Growth Des*, page 5006–5017, 2020.

[185] S. Fermani, B. Njegić Džakula, M. Reggi, G. Falini, and D. Kralj. Effects of magnesium and temperature control on aragonite crystal aggregation and morphology. *CrystEngComm*, 19(18):2451–2455, 2017.

[186] E. Loste, R. M. Wilson, R. Seshadri, and F. C. Meldrum. The role of magnesium in stabilising amorphous calcium carbonate and controlling calcite morphologies. *J. Cryst. Growth*, 254(1-2):206–218, 2003.

[187] Y. Xu and N. A. J. M. Sommerdijk. Aragonite formation in confinements: A step toward understanding polymorph control. *Proc. Natl. Acad. Sci. U.S.A*, 115(34):8469–8471, 2018.

[188] D. Gebauer, A. Völkel, and H. Cölfen. Stable prenucleation calcium carbonate clusters. *Science*, 322(5909):1819–1822, 2008.

[189] H. Cai, S. Li, G. Tian, H. Wang, and J. Wang. Reinforcement of natural rubber latex film by ultrafine calcium carbonate. *J. Appl. Polym. Sci*, 87(6):982–985, 2003.